Technical Report

TR-99-43

Inspection of copper canisters for spent nuclear fuel by means of Ultrasonic Array System

Electron beam evaluation, modelling and materials characterization

Ping Wu, Fredrik Lingvall, Tadeusz Stepinski
Uppsala University, Signals and Systems
Department of Material Science

December 1999

Svensk Kärnbränslehantering AB
Swedish Nuclear Fuel
and Waste Management Co
Box 5864
SE-102 40 Stockholm Sweden
Tel 08-459 84 00
+46 8 459 84 00
Fax 08-661 57 19
+46 8 661 57 19

Inspection of copper canisters for spent nuclear fuel by means of Ultrasonic Array System

Electron beam evaluation, modeling and materials characterization

Ping Wu, Fredrik Lingvall, Tadeusz Stepinski
Uppsala University, Signals and Systems
Department of Material Science

December 1999

Summary

Research conducted in the fifth phase of the SKB's study aimed at developing ultrasonic techniques for assessing EB welds copper canisters is reported here. This report covers three main tasks: evaluation of electron beam (EB) welds, modeling of ultrasonic fields and characterization of copper material.

A systematic analysis of ultrasonic interaction and imaging of an EB weld has been performed. From the analysis of histograms of the weld ultrasonic image, it appeared that the porosity tended to be concentrated towards the upper side of a HV weld, and a guideline on how to select the gates for creating C-scans has been proposed.

The spatial diversity method (SDM) has shown a limited ability to suppress grain noise both in the parent material (copper) and in the weld so that the ultrasonic image of the weld could be improved. The suppression was achieved at the price of reduced spatial resolution.

The ability of wavelet filters to enhance flaw responses has been studied. An FIR (finite impulse response) filter, based on Sombrero mother wavelet, has yield encouraging results concerning clutter suppression. However, the physical explanation for the results is still missing and needs further research.

For modeling of ultrasonic fields of the ALLIN array, an approach to computing the SIR (spatial impulse response) of a cylindrically curved, rectangular aperture has been developed. The aperture is split into very narrow strips in the cylindrically curved direction and SIR of the whole aperture by superposing the individual impulse responses of those strips. Using this approach, the SIR of the ALLIN array with a cylindrically curved surfaces has been calculated. The pulse excitation of normal velocity on the surface of the array, that is required for simulating actual ultrasonic fields, has been determined by measurement in combination with a deconvolution technique. Using the SIR and the pulse excitation obtained, the pulsed-echo fields from the array have been simulated. Measurements of the pulse-echo fields, performed using a small point reflector has yielded results very similar to the simulated ones. This has basically validated the developed approach.

Elastic fields in an immersed copper canister radiated by two apertures (consisting of 16- and 32-elements) have been calculated using the estimated pulse excitation of the ALLIN array in eight cases. These results have shown a very good correlation (e.g., the variations of beam widths or lateral resolutions with depth) with the measured pulse-echo fields from side-drilled-holes in copper block that were presented in our previous report.

For material characterization, two issues have been addressed, the quantitative estimation of attenuation of a solid in the immersion case, and the estimation of grain noise.

To quantitatively estimate attenuation of a solid in the immersion case, a method for correcting the diffraction effect has been developed for the log-spectral difference method (LSDM). The correcting method has been established based on the extended angular spectrum approach used for calculating the echoes from the front and back surfaces of the immersed solid. The correcting method has been theoretically tested for the case of attenuation estimation of copper plate submerged in water and inspected by a linear array with a cylindrically curved surface. The obtained results have demonstrated that the method is capable of effective diffraction correction and thus enables quantitative estimation of attenuation.

For the estimation of grain noise, the ISM and the K-distribution method have been used and the results have been compared. The results have revealed that the higher attenuation and the larger FOM correspond to the larger grains. The results from the K-distribution method have demonstrated the possibility of using the K-parameter as a parameter related to the grain size and the number density of grains. However, the quantitative relation of the K-parameter with the grain properties has not been determined, and it needs further research.

Sammanfattning

Denna rapport innehåller den femte delen av en undersökning ämnad åt att undersöka ultraljudstekniker för att inspektera kopparkanistrar och dess svetsar. Innehållet kan delas upp i tre huvudområden: utvärdering av elektronstråle (EB) svetsar, modellering av ultraljudsfält samt materialkarakterisering.

En systematisk analys av interaktionen mellan ultraljud och svetsar har utförts. Speciellt har materialbrusets egenskaper och spridning i svetsen beaktats. Baserat på analys av histogram från ultraljudsdata har det visat sig att porositet tenderar att koncentrera sig till de övre delarna av en HV svets. Utifrån detta har en metod att välja lämpliga trösklar för att skapa C-scan utvecklats.

SDM (spatial diversity method) visade sig delvis kunna undertrycka materialbruset. Detta sker dock på bekostnad av reducerad spatiell upplösning.

En metod för undertryckning av matrialbrus och förbättra defektdetektion, baserad på en wavelet-transform, har implementerats. Forskningen är dock fortfarande i ett tidigt skede. I framtiden kommer andra metoder för att hitta egenskaper hos EB svetsarena att undersökas. Exempelvis kommer konstruktion av lämpliga filter, modellbaserade metoder samt fokuserade sökare med lägre centerfrekvens att studeras.

För modellering av ultraljudsfält för ALLIN systemet har en metod för att beräkna det rumsliga impulssvaret (SIR) av en cylindrisk formad rektangulär apertur utvecklats. Metoden beräknar SIR som en superposition av ett stort antal tunna element. Ultraljudsfältet har sedan bestämts baserat på en superposition av individuella SIRs. De simulerade resultaten har sedan jämförts med mätningar där en liten spridare har använts och det har visat sig att simuleringarna och mätningarna överstämmer väl.

Med hjälp av metoden ovan har sedan fältet beräknats som referens för immersions-mätnigar på koppar för åtta olika fall. Fältet har beräknats med en apertur bestående av 16 och 32 element för olika djup. De beräknade fälten överstämmer väl med uppmätta fält på ett block med sidoborrade hål (vilka har presenterats i en tidigare rapport).

De två materialegenskaper som har studerats är dämpning samt materialbrus. För att kvantifiera skattning av dämpning vid immersionmätning av koppar har en metod för att korrigera diffraktions-effekten för LSDM-metoden (log-spectral difference method) utvecklats. Denna korrektionsmetod, som bygger på vinkelspektral metoden (ASA), har använts för att beräkna ekon från ytorna på kopparblocket. De teoretiska resultaten visar att den skattade dämpningen stämmer mycket väl överens med den sanna. De mätningar som har utförts ger också rimliga värden på dämpning. Sammantaget är alltså metoden kapabel att kompensera för diffraktions-effekter vilket möjliggör kvantitativa mätningar av dämpningen i koppar.

För att skatta materialbruset har ISM metoden och K-fördelningsmetoderna använts. De båda metoderna har jämförts och det har visat sig att högre dämpningen och högre FOM (figure of merit) härrör från större korn.

Med hjälp av K-fördelningsmetoden visade det sig att det var möjligt att relatera storleken hos kornen och tätheten till K-parametrar, men någon kvantitativ relation mellan K-parametrarna och kornsstorlek/täthet har ännu inte bestämts. För detta krävs ytterligare forskning.

CONTENTS

1 Evaluation of Electron Beam Welds

1.1 Introduction

SKB and TWI have developed an electron beam (EB) welding technology for sealing copper canisters designed for spent nuclear fuel [1]. In the past four years, Uppsala University has carried out a series of research concerned with ultrasonic inspection of EB welds in copper canisters by means of ultrasonic array system [2-4]. We have investigated the feasibility of ultrasonic array technique [2], demonstrating its fitness for the purpose [3]. We have also investigated EB welds' grain noise and the method of its suppression for enhancing defect detection [4]. The present works are mainly to carry on the previous ones related to EB welds, and have been conducted in the following aspects:

(i) ultrasonic interaction and imaging of an EB weld,

(ii) feature analysis and extraction,

(iii) grain noise analysis and suppression, and flaw-detection enhancement.

The purpose of all these works is to evaluate the quality of EB welds.

In the previous work [2-4], analysis of ultrasonic inspected EB welds was made mainly based on C-scans showing the general longitudinal (top) view of EB welds, and secondarily on the B-scans that were, according to the C-scans, usually selected at the positions where the strong indications of defects may be located, and were used to show the depths of the indications. The attention has been focused only on the observation of defects in the welds. Since all the C-scans of welds show grain-noise-like patterns, distinguishing the small defects from such 'grain noise' become difficult, and thus we have put some effort on estimating and then suppressing the grain noise in welds [4]. We recognized two different types of grain noise. The first one comes from the non-welded zone and the second from the welded zone in a copper canister, but did not give any detailed analysis. For the grain noise estimation, we had a try at the K-distribution model in the case of C-scans when a weld inspected was insonified by normal incident beams (refer to Fig. 1.1). The model is not suitable for the case of B-scans because the B-scans contain the weld layer and thus are not homogeneous. For the grain noise suppression we had before applied two frequency-diversity methods, i.e., the noncoherent detector (NCD) and the split spectrum processing (SSP), and a spatial diversity method, which used only 5 different steered beams (due to the time delay limits of the ALLIN system) to make spatial compounding of C-scans. The NCD and SSP seemed to be unable to suppress the 'grain noise' in the weld. The method of spatial diversity may have some potential for the grain noise suppression. In principle, the frequency and spatial diversity methods should be able to suppress grain noise although impossible to completely eliminate it. This has led us to answer the question: why do the NCD and

SSP methods not work? And this has motivated us to gain a deeper insight into the micro- and macrostructure of EB welds, to analyze the ultrasonic interaction of weld microstructure and to describe the picture of a weld macrostructure based on ultrasonic data. Therefore, some ultrasonic properties of a weld have been found out. Since ultrasonic images and data are always deteriorated by the grain noise, the suppression of grain noise remains to be of our big interest and it has been realized in different methods for different purposes.

Detection of flaws in welds is of the utmost importance for this on-going project. Therefore, enhancement of flaw detection has been conducted. In general, there are two ways that are possibly employed to make the enhancement. One is the suppression of grain noise, but it is still very limited. The other is to use the ultrasonic features that are different between flaws and welds. The work dealing with feature analysis and extraction is just for this purpose.

All these works are arranged in the following scheme. First, EB welding process and EB weld micro- and macrostructure are briefly addressed in relation to ultrasonic propagation and scattering. Then the measured ultrasonic signals are presented, ultrasonic interaction of EB welds analyzed, and ultrasonic imaging of the welds is interpreted from the point of view of physical acoustics. These two aspects that are the foundation for the EB weld evaluation are presented in Sects. 1.2 and 1.3. Based on these, the feature analysis and extraction of the signals from EB welds are conducted, and the grain noise in the signals is analyzed and estimated in Sects. 1.4. Finally in Sect. 1.5, grain noise analysis and suppression are carried out, and enhancement of flaw detection is implemented.

1.2 Electron beam welds and their structures [1]

1.2.1 EB welds in copper canisters and their structures

Electron beam (EB) welding is a fusion welding process in which heating results from the impingement of a beam of high-speed electrons on the metal to be welded [5-6]. In general, a single-run fusion weld consists of a fusion zone (FZ) and a heat-affected zone (HAZ) (see Fig. 1.1). Because of the high power and heat concentration of an EB, the fused zone of an EB weld is narrow and the heat-affected zone is very small, and thus both metallurgical damage and distortion are low [1] [7, p. 85]. The microstructure variations in the fusion and heat-affected zones are different because of the different heat influences.

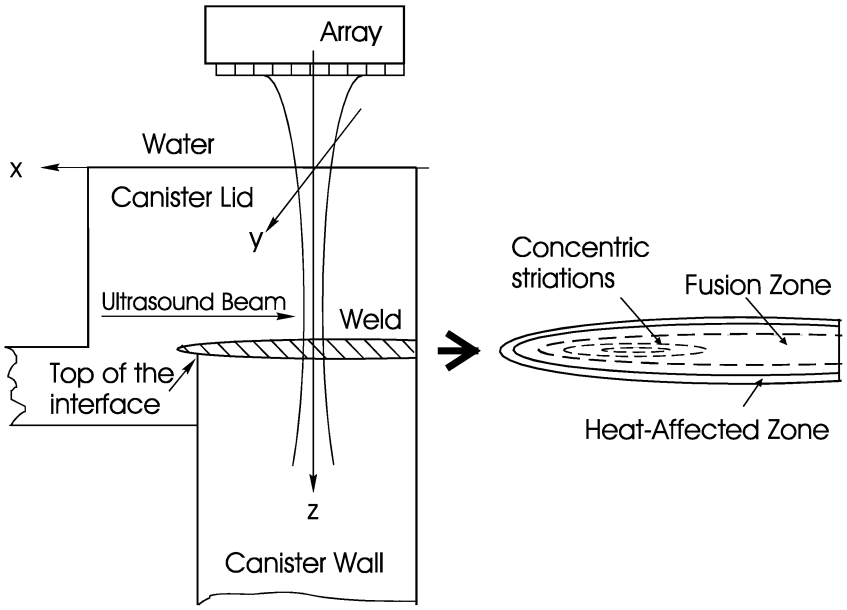

Fig. 1.1. Schematic of EB weld structure and of ultrasonic inspection of the EB weld.

In our case, the EB welding is used for sealing copper canisters. The copper grades used for making copper canisters are deoxidized low phosphorus (DLP) and oxygen-free high conductivity (OFHC) copper [1]. Copper is a face-centered cubic metal [6]. In terms of solidification and grain structures, there is little difference between DLP and OFHC grades. The copper canister lids are welded mainly in horizontal-vertical position. The grain size in copper was estimated as 5-10 micron [1], whereas in the EB welds in copper canisters, grains are much coarser [1] and can be larger than 1000 microns [8].

In both the DLP and OFHC grades, 'solidification fronts' were found, as the welding capillary is constantly fluctuating during the welding process. Thus, the rate of solidification or grain growth at the solidification front is constantly changing. This is typical for copper and other materials that have a narrow freezing range. Instead of merely slowing down, the solidification process may actually reverse altogether temporarily as a particular superheated mass of molten copper washes past the solidification front. This could be seen particularly clearly near the fusion zone tip in many cases, where the solidification fronts overlap, later ones obliterating earlier ones in places. However, this uneven solidification did not give rise to cold shuts or other root defects in the majority of cases. In all cases the fusion zone contained concentric striations indicating the progression of the freezing front which in most cases appeared to be terminated in the lower half of the fusion zone. The irregular solidification fronts may result in uneven boundaries of weld layers in the copper canisters.

Most of the welds have elongated grains along the weld centerline. This elongation along the weld centerline results in orientations of grains in some preferred direction, and thus leads to anisotropy in the weld. The anisotropy has very significant effect on ultrasound incident on the tip area.

1.2.2 Flaws

In principle, the fused and heat-affected zones of EB welds are narrow and this minimizes both metallurgical damage and distortion [7, p. 85]. However, the joint fit-up prior to welding must be accurate, and the motion of the electron beam gun relative to the joint must be equally accurate. Even so, deep-penetration welds may be subject to defects such as cold shuts or lack of fusion, porosity and hot cracking if the correct procedures are not followed.

From the report by Sanderson *et al* [1], with the exception of some 'cold shut' type defects near the top bean of some flat position welds, no cracks or other cold shuts or root defects were found. The only defects discovered of any kind were occasional micro-porosity defects, There were typically 0.1-0.3 mm diameter, tiny spherical pores, which were regarded as insignificant.

The detailed examination of the root region shows that tiny porosity defects can form near the unfused region of the joint, but that other root defects are absent [1]. Typically porosity tended to be concentrated towards the upper side of HV welds, presumably as bubbles formed and floated upwards in the melt.

More detailed knowledge on EB welds, their structures and properties can be found in Refs. 1, 5-7. From the above-presented analysis, it can conclude that a fusion weld can be though of as a multi-layered medium consisting of a fusion zone and a heat-affected zone that surrounds the fusion zone. Each zone contains grains different from the others in size and orientation. In the EB weld case, the grains are coarse in the fusion zone, much smaller in the heat-affected zone, and fine and smallest in the weld parent material.

1.3 Ultrasonic interactions and images of EB welds

Inspections of EB welds have been made using the ALLIN ultrasonic array system in our previous work [2-4]. The schematic of inspection setup is illustrated in Fig. 1.1. The ultrasound beam is normally incident on copper canister immersed in water and insonifies the EB weld. The beam was scanned electronically in the x direction and mechanically in the y direction. The data acquired in this way is 3 D, and thus can be displayed in different scan modes, usually, in A-, B- and C- scans. In the present case, the data at each point along the y direction is shown in a B-scan which is produced by electronic scanning and is a 2-D image extending in the x and z directions. When the data in a certain depth interval (or time interval) along the z direction is selected by a depth (time) gate and at each point (x, y) the peak value in the interval is picked out, it is shown in a C-scan that extends in the x and y directions.

In the previous work, we analyzed ultrasonic inspected EB welds mainly based on C-scans showing the general longitudinal (top) view of EB welds, and secondarily on the B-scans. The B-scans were, according to the C-scans, selected usually at the positions where the strong indications of defects may be located, and were used to show the depths of the indications. The attention has been focused only on the observation of defects in the welds. In this section we turn our attention to other aspects of ultrasonic inspection of welds, i.e., ultrasonic interaction of weld microstructure and imaging of weld macrostructure.

To this end, a detailed analysis of the measurements was made on one of the copper canister samples, i.e., Block 3 of Weld W123, that was inspected in 1997 using the ALLIN system with 16-aperture [3]. Presently this block was re-inspected for a different purpose, i.e., to investigate EB weld structure. In the present measurements, we used a 32-element aperture with the focusing law, Foc80e32 that was presented in our last report [4]. The focusing law was assumed to locate the geometrical focal zone in the canister at z=80 mm through a 28-mm water layer, and actually yielded a narrow beam that was rather uniform over a distance range around z=60 mm where the weld centerline is positioned (refer to Fig. 2.3 and Table 2.2. in [4]). Since the ALLIN array has 64 elements with 0.9-mm width and 1-mm separation, 33 A-scans are available, using this 32-element aperture, for each B-scan that was made electronically in the x direction. In the y direction, the beam moved over 240-mm distance with 1-mm step, and thus 240 B-scans were obtained. This makes 33x240 (i.e., 7920) A-scans. The sampling frequency used was 50 MHz, and the gain used was 12 dB. The region of interest was around the EB weld in the copper canister, that is, from 31 to 81 mm beneath the canister surface (see Fig. 1.1). It should be noted that the coordinates used in the following figures (Figs. 1.2-1.4) are defined in Fig. 1.1. The weld was examined from longitudinal view (C-scan), and from transverse view (B-scan) in combination. Generation of a C-scan needs a gate that selects a data region in the z direction. This gate can be wide or narrow according to the region of interest. In the limit case, the gate is narrow that it corresponds to only one sampling point. A C-scan obtained using such a gate that reflects information at a local depth will be named here 'local C-scan', in order to distinguish from a conventional C-scan that is created using an extended gate. A C-scan, meaning a conventional C-scan, provides the information on the distribution of maximum backscattering from a weld. A local C-scan provides the more localized information on the backscattering from a weld at a certain depth. The local C-scan only applies to the envelope of the ultrasonic signal, or simply the enveloped data. From a B-scan, it is easier to see the grain noise pattern both in the weld and in the parent material, and to measure the depths of flaws. An A-scan shows more detailed information in a narrower range. Each of the scan modes complements with others, showing the 3-D ultrasonic data in different ways.

1.3.1 General longitudinal view of the EB weld - C-scan

The C-scan was obtained by depth (time) gating the signals around the weld (between z=50 and 75 mm) and picking up the peak amplitude of the signals. The C-scan obtained and the histogram in the weld zone calculated are shown in Figs. 1.2 (a) and (b), respectively. The C-scan gives a general longitudinal view of the EB weld. The histogram demonstrates the distribution of the maximal backscatter from the EB weld against amplitude level. The C-scan having 7920 points covers an area of 33 mmx240 mm. The amplitude level of the C-scan ranges from 0 to 128. Three strong indications of defects that are seen in the region between y=200-240 mm are saturated (i.e., their tops are cut off). They are easy to distinguish from the backscatter from the normal part of the weld so that they are not of our present interest. The amplitude level range of the histogram in Fig. 1.2(b) is only taken from 0-80 just for easier observation and also because of the very low occurrence of amplitude levels higher than 80. From Fig. 1.2(b), we can see that the occurrence of the amplitudes increase over the amplitude range of 0-18, reach the maximum at the amplitude level of 18, and decrease for the amplitude level larger than 18. The low amplitude part, e.g., increasing from amplitude level 1 to 10, is mainly attributed to the scattering from the transit region from the non-welded zone to the weld zone, which contains the weld tips. The medium-sized amplitude part, e.g., over the amplitude range of 10 to 40, is mainly attributed to the grains in the weld, and the large amplitude part, e.g., larger than 50, may be largely due to scattering from the micro-pores or some other flaws in the weld.

A C-scan does provide a general longitudinal view of an EB weld, and from the C-scan, it is convenient to choose the B-scans of interest, showing the location of strong flaw indications. However, in a C-scan of this type many indications of flaws or some other reflectors that are strong at that depth but weaker in the gated depth interval are submerged in this grain-noise-like pattern, see, e.g., Fig. 1.5 in the following section, Sect. 1.3.3.

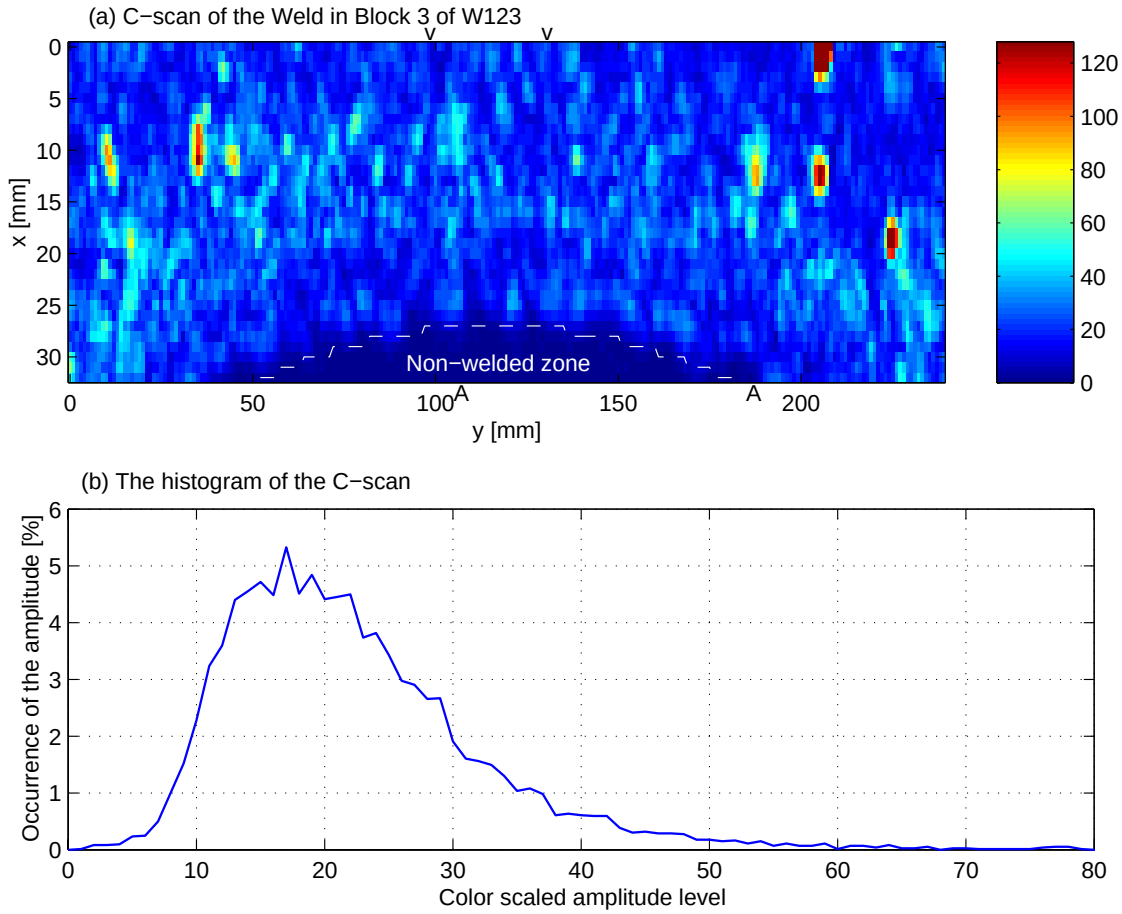

Fig. 1.2. The measurements made on the EB weld in Block 3 of Weld W123. (a) The C-scan of the weld and (b) the histogram of the C-scan with the non-welded zone excluded.

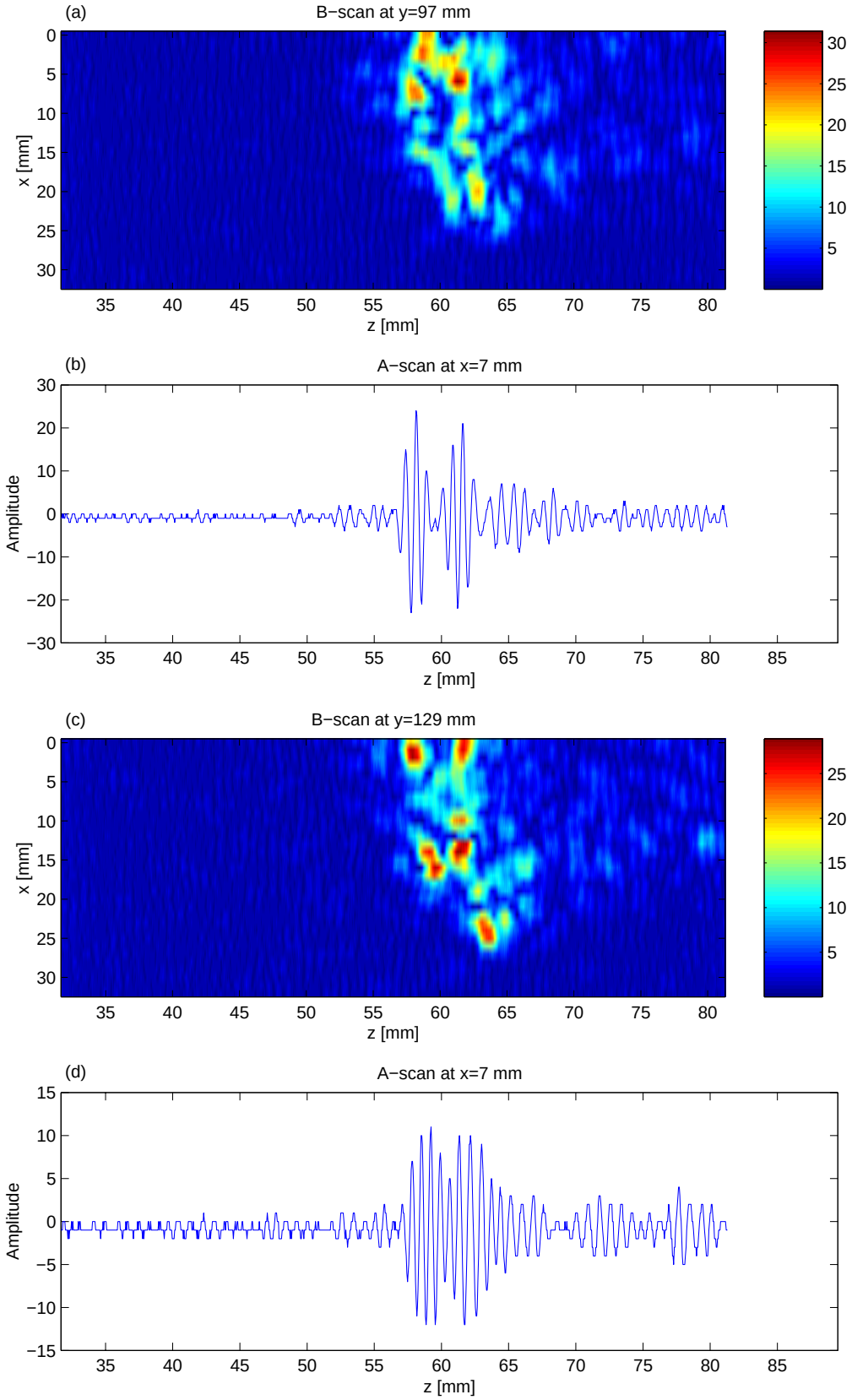

Fig. 1.3. The measurements made on the EB weld in Block 3 of Weld W123. (a) B-scan at *y*=97 mm in the C-scan in Fig. 1.2, and (b) an A-scan at *x*=7 mm in (a); (c) B-scan at *y*=129 mm in the C-scan in Fig. 1.2, and (d) an A-scan at *x*=7 mm in (c). The two positions are marked with letter 'v' in Fig. 1.2.

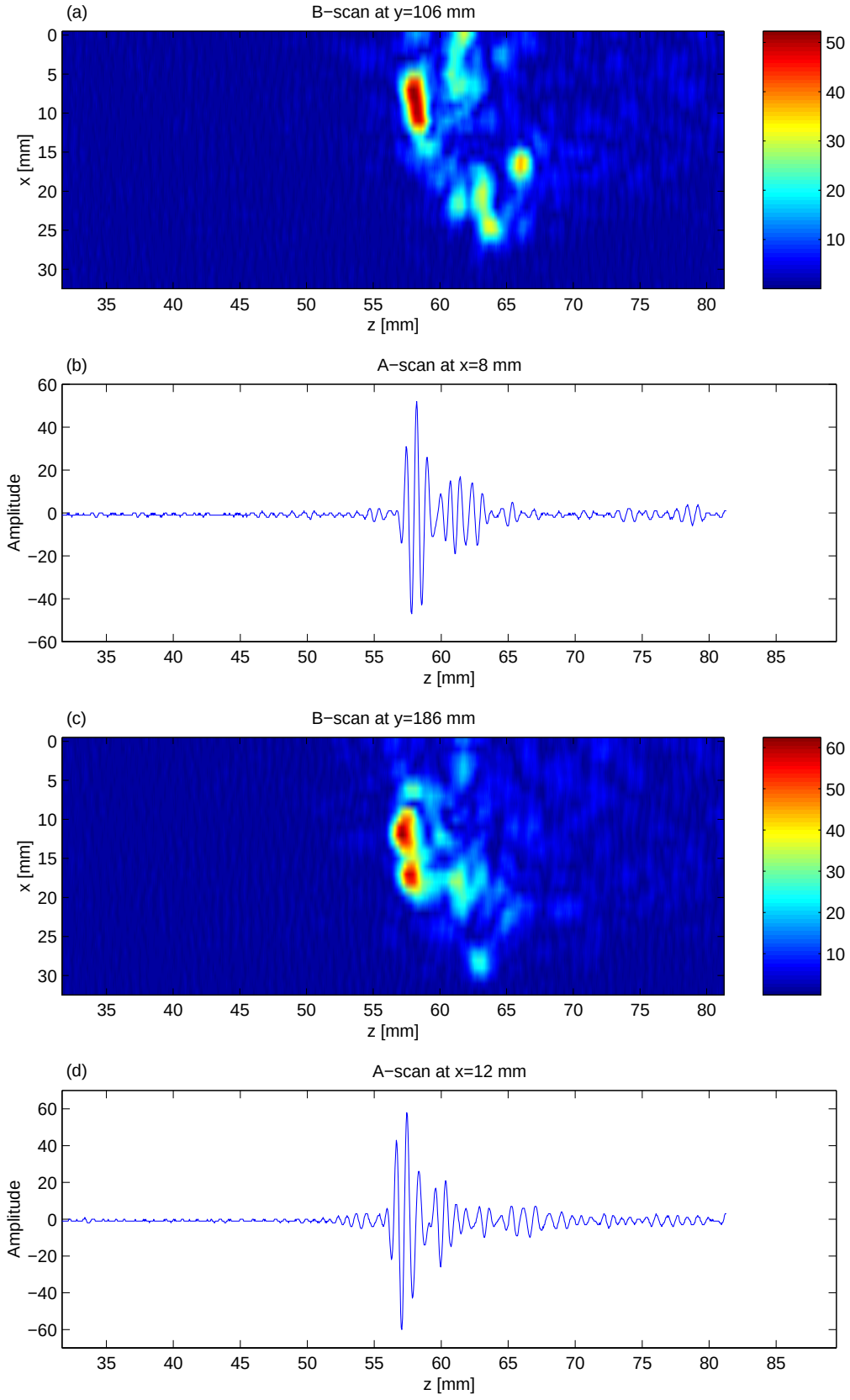

Fig. 1.4. The measurements made on the EB weld in Block 3 of Weld W123. (a) The B-scan at *y*=106 mm in the C-scan in Fig. 1.2, (b) an A-scan at *x*=8 mm in (a), (c) the B-scan at *y*=186 mm in the C-scan in Fig. 1.2, and (d) an A-scan at *x*=12 mm in (c). The two positions are marked with letter 'A' in Fig. 1.2.

1.3.2 Transverse view of the EB weld - B- and A-scans

To examine transverse view of the EB weld, four B-scans were selected based on the C-scan in Fig. 1.2. The two B-scans at y=97 and 129 mm (marked with letter 'v' in Fig. 1.2) contain relatively weak scattering, and are shown in Figs. 1.3 (a) and (c) where the maximum amplitude levels are 29 and 27, respectively. The other two at y=106 and 186 mm (marked with letter 'A' in Fig. 1.2) contain stronger scattering, and are shown in Figs. 1.4 (a) and (c) where the maximum amplitude levels are 52 and 58, respectively. To facilitate analyzing grain noise pattern, all the B-scans in this subsection are displayed in signal envelope and from each selected B-scan an A-scan is chosen and displayed just below. Obviously the lower parts of the four B-scans (x>25 mm) cover the tip end of the weld. From the B-scan in Fig. 1.3(a), it seems to be possible to roughly figure out a pattern of the weld cross-sectional structure because the shape formed by the strong echoes resembles a cross-section of a tube. Apparently, there is a low echo area in the middle of the 'tube', and 'its walls' look not to be continuous and smooth. At the lower ends of the 'walls' (the weld tip) we can see that they are bent to the deeper direction (to the right in the figure). The reasons for this are most probably the effects of refraction and weld anisotropy. The refraction effect arises from the difference of ultrasonic speeds between the weld parent material and its heat-affected and fusion zones and the o*blique* incidence of the ultrasonic beams on the weld tip at which the two zones become round. The anisotropy causes the angle-dependent speed. The weld bending toward the deeper direction may suggest the ultrasonic speed in the weld should be lower than in the parent material, which needs further verifying. Now looking at the B-scan in Fig. 1.3(c) and based on the above observation, we can see some similarity. To investigate the ultrasonic interaction of an EB weld, we divide the B-scans into five different regions in terms of the contents of backscattered signals.

(i) In the first region, z = 31~ 52.5 mm, we can see the fine grain noise that results from the fine grains in the parent material.

(ii) In the second region, z = 52.5~ 56.5 mm, a little stronger echo area is weakly visible and is overlapped with fine grain noise. The echoes in the area come from the heat-affected zone (HAZ) that contains a little coarser grains.

(iii) In the third region, z = 56.5 ~ 63.5 mm, we can see two columns of strong echoes and a weaker scattering, strip-like area between the columns that extend over the range of x = 0 ~ 24 mm in Fig. 1.3, and x = 0 ~ 26 mm in Fig. 1.4. These strong echoes may be caused by the big variations of microstructure from the HAZ to the fusion zone. The traces of the variations may form the boundaries of the fusion zone (x = 0 ~ 24 mm in Fig. 1.3, and x = 0 ~ 26 mm in Fig. 1.4). According to the inspection configuration in Fig. 1.1, the boundary on the left is called front (or upper) boundary, and the one on the right called back (or lower) boundary, which correspond to

the upper and the lower side of a horizontal-vertical weld. Apparently, the boundaries do not look continuous and well-defined. The reasons are probably due to irregular fronts of weld solidification. Below the strong echoes, we can see some weaker echo areas that correspond to the HAZ around the weld tip (x = 24 ~ 28 mm in Fig. 1.3, and x = 27 ~ 30 mm in Fig. 1.4). Further below, there is a weak scattering (fine grain noise) area (x = 28 ~ 32 mm in Fig. 1.3, and x = 30 ~ 32 mm in Fig. 1.4) that is the parent material. In this third region there are the echoes from the fusion zone, and the multiple scattering from the HAZ and the parent material although the multiple scatters are so weak to be difficult to see.

(iv) In the fourth region, z = 64 ~ 67 mm, there is an echo area that is much weaker than in the third region but a little stronger than in the second region, and the echoes in this area result from the scattering from the HAZ and the multiple scattering from the fusion zone.

(v) In the fifth region, we can see a combination of fine and coarse grain noise. The fine one comes from the parent material and the coarse one arises from the multiple scattering among the coarse grains in the weld zone.

Now let us move to the two B-scans in Fig. 1.4 that contain quite much stronger echoes from the EB weld. The B-scan in Fig. 1.4 (a) contains one strong echo spot around point, x=9 mm and y=57 mm, on the front boundary of the weld, and the B-scan in (c) contains two strong echo spots at points, x=12 mm and y=56.4 mm, and x=17 mm and y=56.8 mm, both on the front boundary of the weld. At the first glance, it seems to be impossible for us to figure out the weld structure from each of the B-scans because the strong echoes scale down the area containing echoes from the boundaries of the weld. Also the fine grain noise in the parent material area, apparently, is weaker compared to the one in Fig. 1.3. However, if using a smaller scale, e.g., the scale used in Fig. 1.3, we can see the weld images quite similar to those in Fig. 1.3. The three strong echo spots in Fig. 1.4 probably come from the three pores with diameter larger than the coarse grains in the weld.

From the above analysis and taking into account the effects of refraction and anisotropy, the weld structure seen from its ultrasonic image seems to be in accordance with its metallographs reported by Sanderson *et al* [1].

1.3.3 Local longitudinal view of the EB weld - local C-scans

As mentioned in the beginning of this section (Sect. 1.3), local C-scans can be used to show the longitudinal views of the EB weld at different depths. Here, six local C-scans (see Fig. 1.5(a)-(f)) are chosen at different depths in different regions that may contain the weld or not. They are located from shallow to deep positions, respectively, at (a) z=55.22 mm in the front HAZ, (b) z=58.21 mm at the front boundary of the fusion zone, (c) z=60.660 mm in the fusion zone, (d) z=62.20 mm at the back boundary of the fusion zone, (e) z=64.65 mm in the back HAZ, and (f) z=66.25 mm at the top end of

canister inner wall. In each of the subfigures, we plot a line that roughly defines the boundary between the weld and the non-welded zone. Looking at the C-scans from Fig. 1.5(a) to (f), it can be seen that the boundary moves downwards and becomes smaller, and then from Fig. 1.5(e) to (f) the boundary moves upwards and becomes larger. Combining the C-scans together with the B-scans in Sect. 1.3.2, we may be able to imagine a rough, 3-D image of the weld layer. The image seems to be in agreement with the EB weld structure reported in [1]. It should be specially mentioned that the C-scan in Fig. 1.5(f) is quite interesting, showing the circumferencial top of the interface between the inner surface of the canister's wall and the lid, and this is the first time that we find it out and show it up. The interface top looks not continuous and smooth, probably because the oscillation of the electron beam during the welding process resulted in the irregular solidification fronts along the circumferential top of the interface. From Fig. 1.5(a) and (b), we also get to know that the three strong indications of defects in the region of y=200-240 mm in Fig. 1.2 are located at different depths, the two at y=205 mm being located deeper than the one at y= 224 mm.

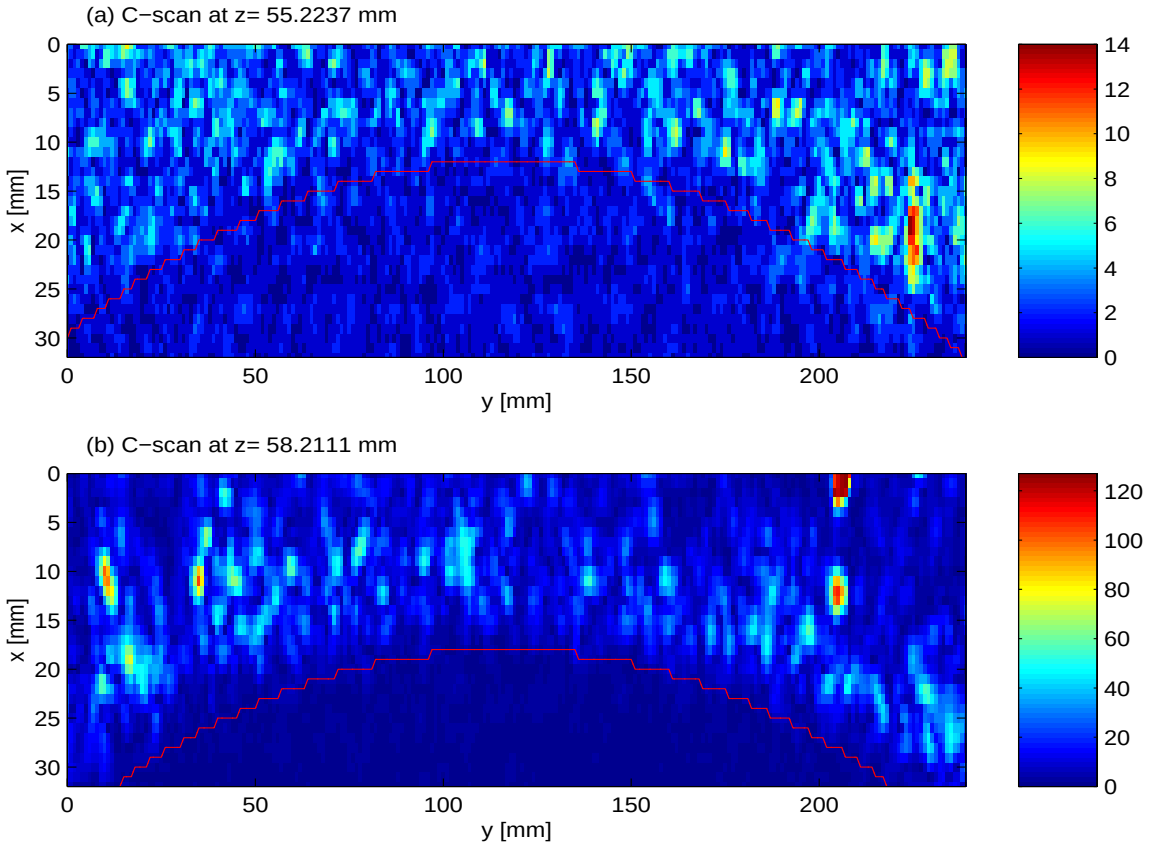

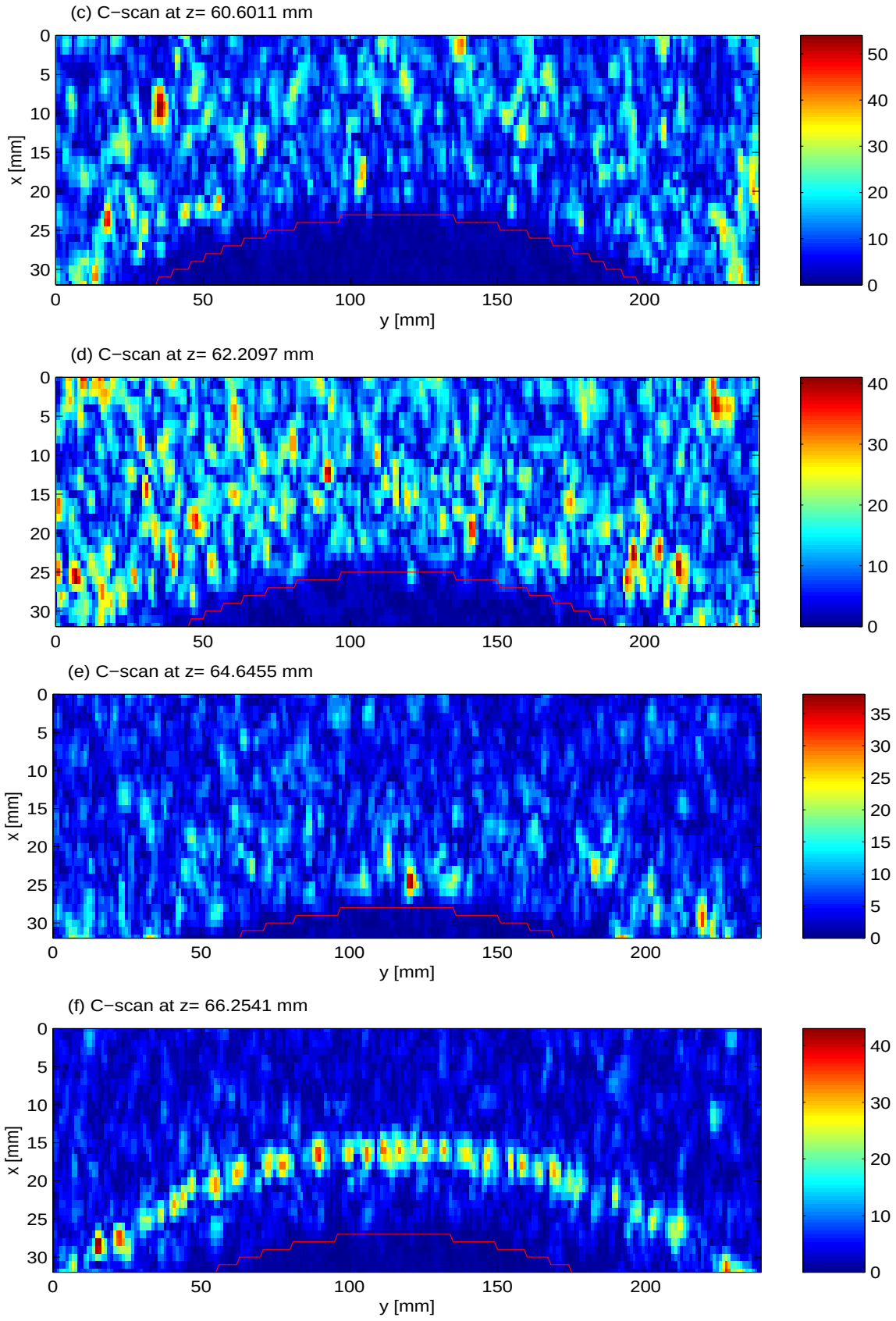

Fig. 1.5. Local C-scans at different depths (a) *z*=55.22 mm in the front HAZ, (b) *z*=58.21 mm at the front boundary of the fusion zone, (c) *z*=60.660 mm in the fusion zone, (d) *z*=62.20 mm at the back boundary of the fusion zone, (e) *z*=64.65 mm in the back HAZ, and (f) *z*=66.25 mm at the top end of canister inner wall.

1.3.5 Summary

The above analysis reveals that an EB weld can be seen to such a multi-layered medium that has a fusion zone layer surrounded by a HAZ layer. The grains in the fusion zone are very coarse and those in the HAZ are finer, but coarser than in the weld parent material. The parent material that surrounds such a layered medium is fine-grained. When inspected using the configuration in Fig. 1.1, a copper canister containing a weld can be roughly treated as a five-layered medium. Each of the five layers, i.e., the five regions above mentioned, contains ultrasonic scatters of different types that have different properties and features. This will be further discussed in the following section.

The structure of an EB weld deduced from its B-scans (transverse view) and local C-scans (longitudinal view) is basically in accordance with that reported by Sanderson *et al* [1] (schematically shown in Fig. 1.1). The boundaries between the parent material and the HAZ and between the HAZ and the fusion zone do not look continuously- and well-defined in the ultrasonic images. Refraction at the boundaries and weld anisotropy may have significant effect on ultrasound at the weld tip, and thus may cause imaging distortion, e.g., the weld bending at the weld tip and the others.

1.4 Feature analysis and extraction

To suppress grain noise and to enhance detection of flaws in EB welds, usually we need to rely on some properties and features extracted from the responses of the welds and flaws. In this section we present two general ways for feature analysis and extraction based on physical acoustic and signal processing methods.

1.4.1 Grain noise and its properties

It is well known that the grains in a metal under ultrasonic inspection act as unresolvable scatterers that result in multiple scattering among them and produce the coherent interference. The coherent interference on a phase-sensitive receiver (the majority of ultrasonic transducers and arrays used in both NDT and medical imaging are phase-sensitive) results in grain noise in ultrasonic echo signals (e.g., A-scan and B-scan signals). The multiple scattering is a random process that can usually be described geometrically by a random walk model [3]. The ultrasonic grain noise due to the coherent interference of the multiple scattering is spatially random, but temporally stable. The grain noise is dependent on the transducer frequency used and spatially diverse, the spatial and frequency diversity methods can be used to suppress the random multiple scatter, that is, grain noise.

We concluded in the former section that a copper canister with an EB weld is an inhomogeneous medium in which the weld is embedded as a multi-layered medium that contains different grains from its parent medium. Now let us examine the ultrasonic interaction of such a copper canister under ultrasonic inspection. When the canister is insonified by a pulse ultrasound beam with the inspection configuration shown in Fig. 1.1, both the weld parent material and the weld layer scatter the ultrasound, and the scattering is of different orders, e.g., the first-, the second-, and the high-order. The first-order scatter of the parent medium occurs at the front surface of the canister, and it is just the reflection. After the first-order scatter, the ultrasound goes into the canister, and it is multiple scattered and attenuated. When the ultrasound goes further, it impinges on the weld layer, and scattered by the layered medium. At each boundary in the weld, either between the weld parent material and the heat-affected zone, or between the heat-affected and the fusion zones, and so forth, the first-order scattering occurs. Then, in every layer the multiple scattering happens, and the scattered ultrasound reverberates. When the multiple scattering either in the parent material or in the weld layer is received by a phase-sensitive receiver, grain noise turns out in the received signal. The multiple scattering in the weld layer is much stronger than in the parent material. Though attenuated fast as it reverberates on, the multiple scattered ultrasound remains so strong that in the B-scan image it is still visible after the weld zone.

The multiple scattering (the high-order scattering) is a random process because the grains, the scatterers, in a polycrystalline metal are randomly positioned and oriented, and thus results in grain noise in a coherent received ultrasonic signal. Unlike the multiple scattering, the first-order scattering does not have a process of scattering from the random scatterers, and thus it is not a random process. It is usually explored for ultrasonic imaging the weld structure. Grain noise usually causes ultrasonic imaging distortion.

Due to the different physical features of grain noise and the first-order scattering, therefore, the spatial diversity method can suppress the grain noise which is random, but not the first-order scattering which is not so random as the grain noise. This will be shown in Sect. 1.5.1 dealing with grain noise suppression.

1.4.2 Statistical analysis of ultrasonic backscattering from EB welds

In the preceding section, Sect. 1.3, we have presented a few ultrasonic signals, that is, the B-scans in Figs. 1.3 and 1.4 and the local C-scans in Fig. 1.5, and made a detailed analysis of ultrasonic interaction and imaging of an EB weld. From these scans, we can see that the amplitudes of ultrasonic (backscattered) signals vary with depths; e.g., in the heat-affected zone the signals are weak, at the boundaries they are strong, and so on. Although this observation is correct, it can not supply a complete picture of how the signal amplitudes vary with depths. Here we make use of a statistical

approach to draw a more complete picture. The approach is based on the analysis of histograms of local C-scans at different depths. A histogram can depict the distribution of amplitude levels of ultrasonic signals. Fig. 1.6 shows the histograms of local C-scans at depths from 50 to 81 mm in the copper canister. The figure is log compressed in order to make visible the low occurrence part in the range of large amplitude level. The vertical axis represents the amplitude level, and the horizontal axis represents the depth. The image in the figure looks like an upside-down mountain with three peaks that are in the depth range of about 55-70 mm over which the EB weld extends. This range is of our special attention. The three downward peaks lie in the intervals of 55-60 mm, 60-65 mm, and 65-70 mm, respectively. The first two correspond to the strong scattered signals from the front and the back boundaries of the weld, and in between there is a small valley, which means the low scattering from inside the fusion zone. The third peak results from the strong scattering by the top of the interface between the canister wall and the lid (see Fig. 1.1).

Among the histograms, we pick out the six histograms corresponding to the six local C-scans in Fig. 1.5, and show them in Fig. 1.7 together with their K-distribution fittings. Concerning the K-distribution, the reader is referred to our previous report [3]. Because the backscattering from the weld structure, not the flaws, is of the main interest presently, the K-distribution fits are made according to the criterion of the minimum error of the histograms calculated from the measured local C-scans and predicted by the K-distribution model. Thus, the K parameter α_1 is used for the fits, and obtained using the low order (first order) central moment of amplitude (refer to Ref. [3]) and the amplitude level range that discards the high amplitude levels with very low occurrences; e.g., in the present case, the amplitude level ranges used for the six fittings are 12, 52, 45, 45, 25, and 20, respectively; and consequently, α_1 obtained are 2.27, 0.95, 2.86, 4.73, 1.91, and 0.92, respectively. Apparently, the K-distribution, on the whole, gives good fit to the histograms of the local C-scans in Fig. 1.7(a), (c)-(e), but does not fit so well for those of the C-scans in Fig. 1.7(b) and (f) that contain several or quite a few individual strong scatterers.

From the above analysis, we can gain some useful information and find out a guideline for selecting gates for C-scans. The fact that the first peak is the largest may indicate that the flaws (usually porosity) most probably exist at the front boundary of the EB weld. This coincides with the investigated results reported by Sanderson *et al* (see Sect. 1.2.2), that the porosity tended to be concentrated towards the upper side of a HV weld, presumably as bubbles formed and floated upwards in the melt. Creating three C-scans using the three gates that cover the three peaks, respectively, we can extract more information on an EB weld. This is shown by Fig. 1.8, in which three C-scans were obtained using such three windows that covered the depth ranges (a) from z=50 mm to 60 mm, (b) from z=60 mm to 65 mm, and (c) from z=65 mm to 70 mm, respectively. From Fig. 1.8(a), it can be seen that most of the strong indications of flaws are in the front boundary region,

from Fig. 1.8(b), one indication is visible in the bask boundary region, and from Fig. 1.8(c), the tip end of the canister inner wall can be seen and also one indication of possible tip flaw at x=26 mm and y=120 mm. Whereas in Fig. 1.2, lots of useful information (e.g., the C-scan in Fig. 1.8(c)) was lost.

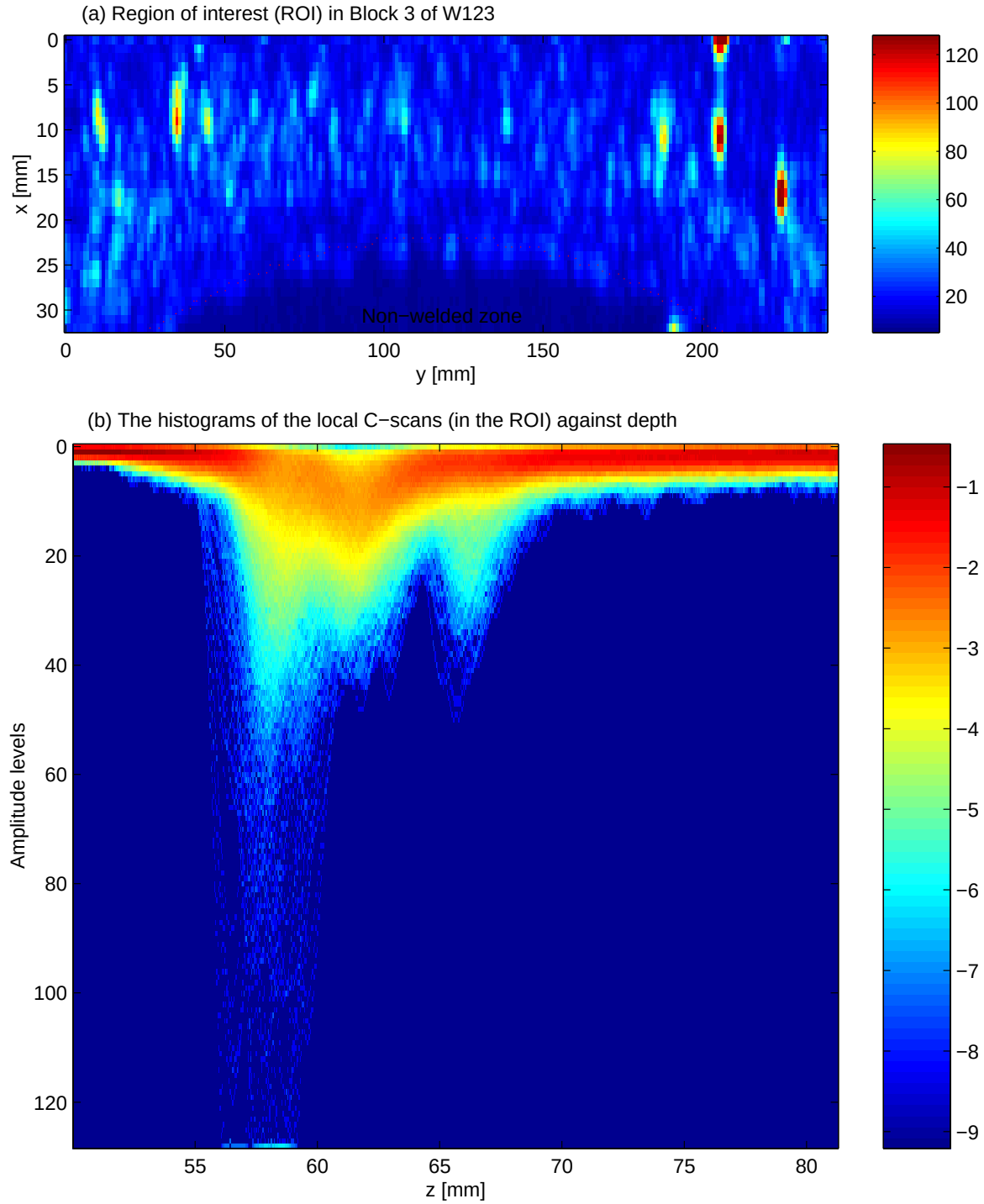

Fig. 1.6. In the region of interest (a), the histograms of the local C-scans in the region of interest are plotted against depth (b). Note that figure (b) is log compressed.

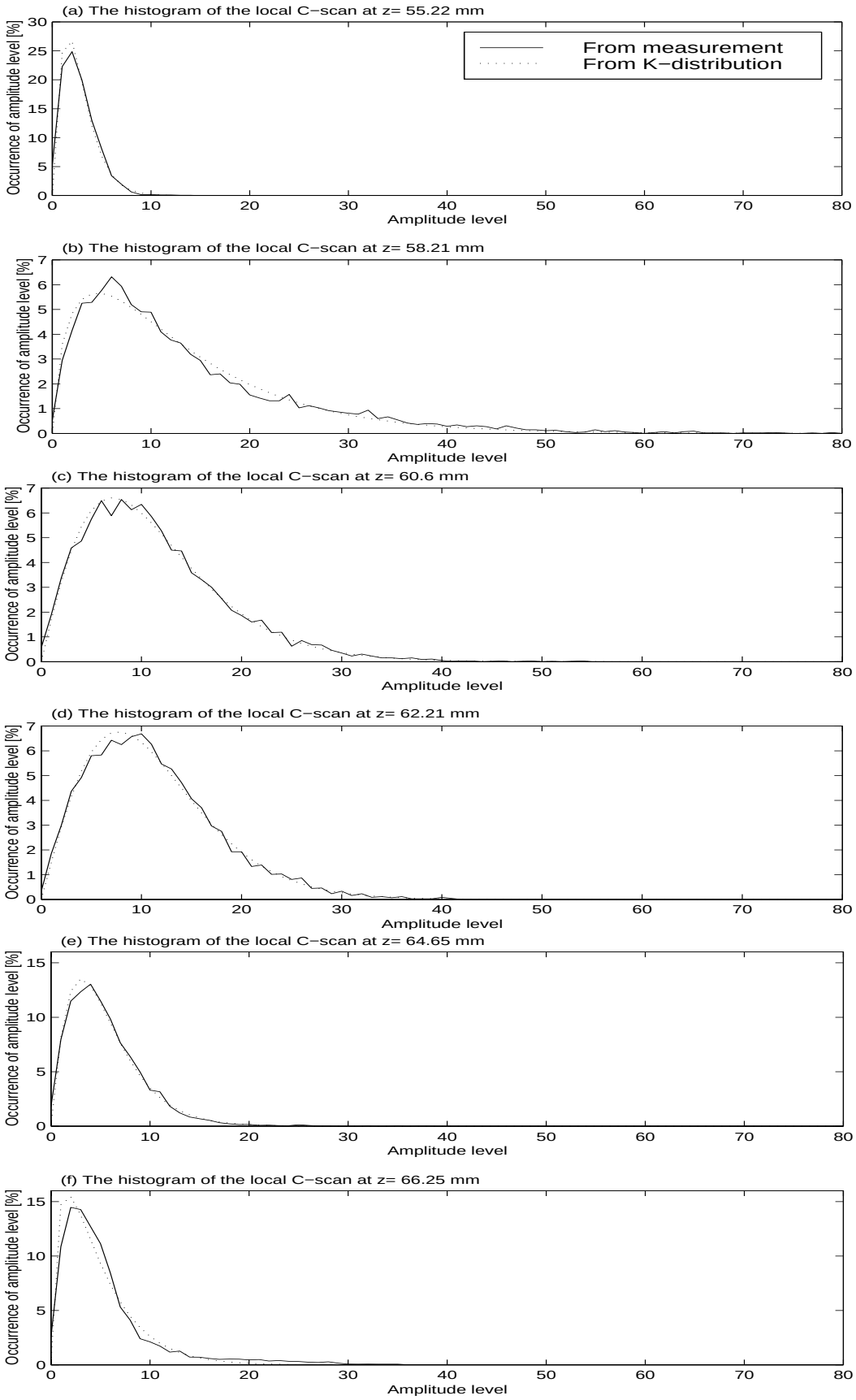

Fig. 1.7. The histograms of the local C-scans in Fig. 1.5, from measurements (solid) and the K-distribution fitting (dotted).

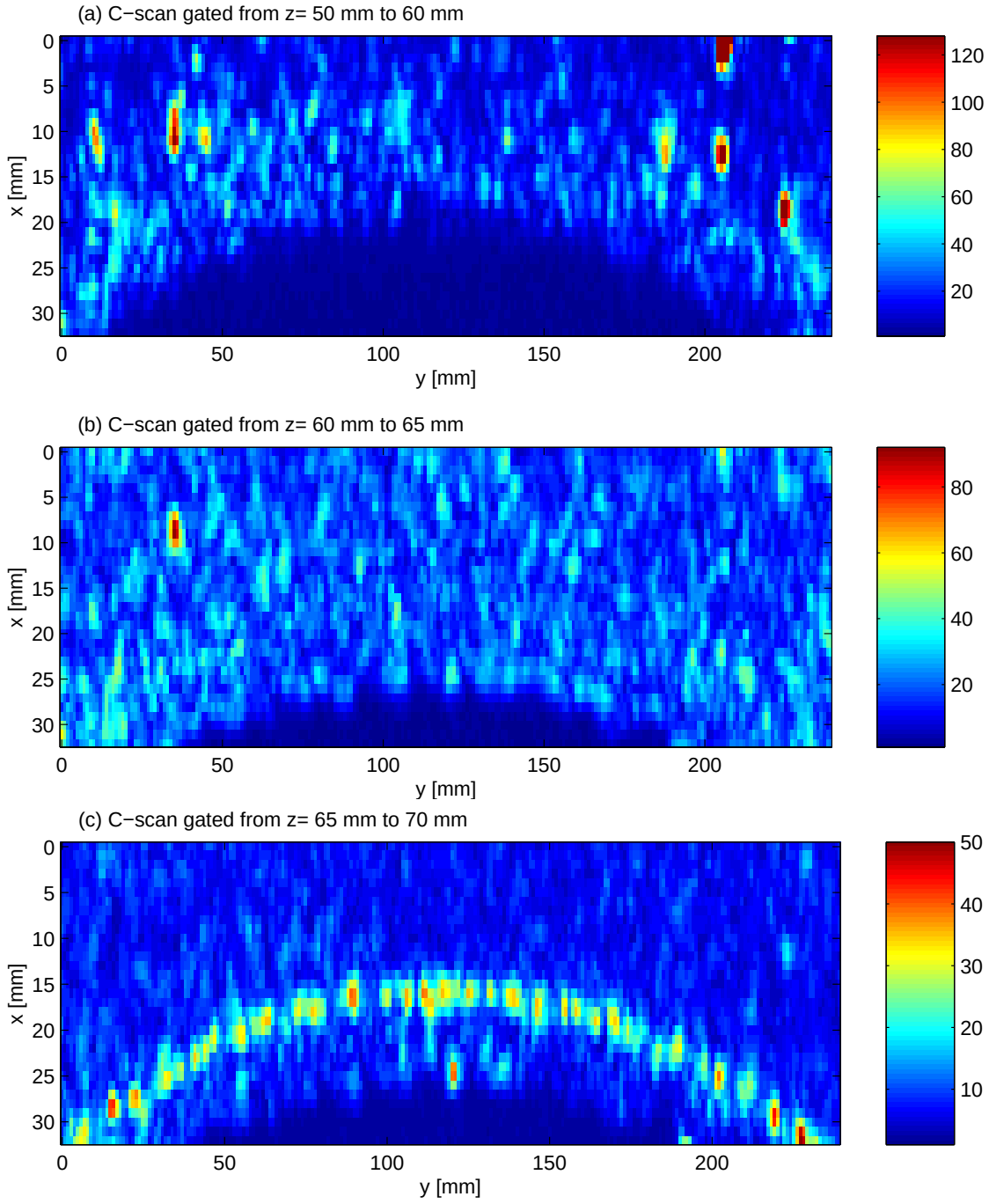

Fig. 1.8. The three C-scans gated by the three windows that cover the depth ranges (a) from z=50 mm to 60 mm, (b) from z=60 mm to 65 mm, and (c) from z=65 mm to 70 mm, respectively.

1.5 Grain noise suppression and flaw-detection enhancement

In this section we present the methods resulting in increasing the sensitivity to week scattering flaws. First, we show the method of suppressing grain noise using spatial diversity method (SDM). Second, we show the way of enhancing the relevant echoes by wavlet filtering.

1.5.1 Grain noise suppression

Due to the random character of grain noise (see Sect. 1.4.1), the spatial diversity method can be used to suppress the grain noise. This is exhibited and under detail investigation in this section.

The spatial diversity method (SDM) has been applied to medical ultrasonic imaging to reduce speckle in ultrasonic images for almost two decades [9-22]. But it has been seldom used in ultrasonic nondestructive testing (NDT). The method is also often called phase-insensitive processing method [9-14], or spatial compounding method [15-22]. These names are taken either after the property of speckle patterns, or after the way that an ultrasonic signal is formed. The spatial diversity method comes from the property of speckle patterns that are spatial diverse. The phase-insensitive processing method is named according to the way that a receiving transducer, usually a transducer array, forms an ultrasonic signal. The spatial compounding name comes from the way that an ultrasonic signal (usually a B-scan) is formed by compounding a set of ultrasonic signals (usually envelope-detected) which are obtained at different position. Below we will refer to as the spatial diversity method (SDM). The SDM can be implemented in different ways, e.g., using different ultrasonic arrays, such as a linear array [9,10,13,14], a phased array [15,16,19,22], a maltese cross array [20], a segmented annuli array [21], or using different synthetic apertures [11,12, 17,18]. The method has been studied extensively, and has shown that the method is quite effective to reduce speckle.

Here, we apply the SDM to the suppression of grain noise from copper canisters. The SDM is implemented based on a linear array and the ALLIN system. More specific, the method is applied to the case corresponding to that presented in Figs. 1.3-1.5 in Sect. 1.3 where the images were obtained using the conventional way of imaging, i.e., phase-sensitive summation of the signals from all the array elements. Since the ALLIN ultrasonic array system does not have the capability of directly obtaining and summing the enveloped-detected signals from the array elements, we have developed an indirect, off-line way to realize the SDM. Similarly to the case in Sect. 1.3, we used 32 elements in the 64-element linear array as aperture transmitting a focused pulse field. But the 32 elements were fixed to elements 3-34, so that the aperture was unable to be electronically scanned in the *x* direction (see Fig. 1.1). Instead, the aperture was mechanically scanned in the *x* direction. At each scanning

position, the aperture was sending the pulse field 32 times, and for each pulse, only one element was used to receive the backscattered ultrasound. In this way, the ultrasonic signals from 32 elements were obtained and acquired by the ALLIN system. Since only one array element was used as receiver, the receiving sensitivity was much lower than that of a 32-element receiver, and thus the gain used in the measurements was 35 dB, which was much larger than in the phase-sensitive case presented in Sect. 1.3 where the gain used was 12 dB. The acquired data were RF signals and could be used to create A- B- and C-scans either in a phase-sensitive way, or in a phase-insensitive way (or equivalently speaking, by means of spatial compounding). In the phase-sensitive way, we can create almost exactly the same C-, B-, and A-scans as those presented in Figs. 1.2-1.5. In the phase-insensitive way, we obtain the so-called spatial compounded data by summing up the envelope-detected signals from the 32 elements. The envelope-detected signals were obtained by means of Hilbert transform and divided by 32, the number of elements used. The B- and A-scans corresponding to those in Figs. 1.3 and 1.4 are shown in Figs. 1.9 and 1.10, respectively. Compared to Figs. 1.3 and 1.4, the B-scans in Figs. 1.9 and Fig. 1.10 look much smoother because the grain noise has been largely reduced. Comparing the B-scans in Fig. 1.9 with those in Fig. 1.3, the boundaries of the EB weld look smoother as well as more continuous. All this indicates that the grain noise both in the weld parent material and in the weld has been largely suppressed, so that the images of a weld structure have been significantly improved.

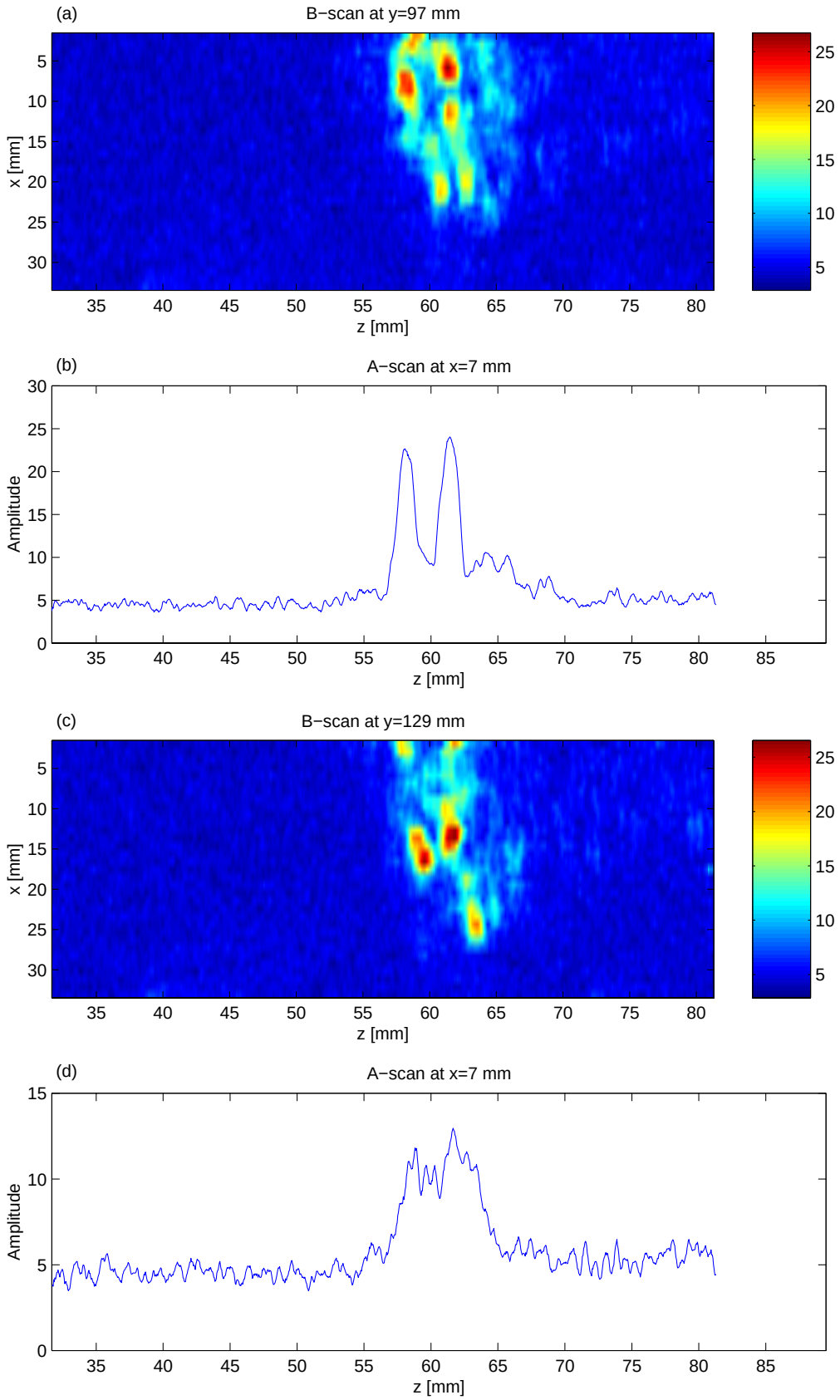

Fig. 1.9. The spatially compounded B- and A-scans that correspond to those in Fig. 1.3.

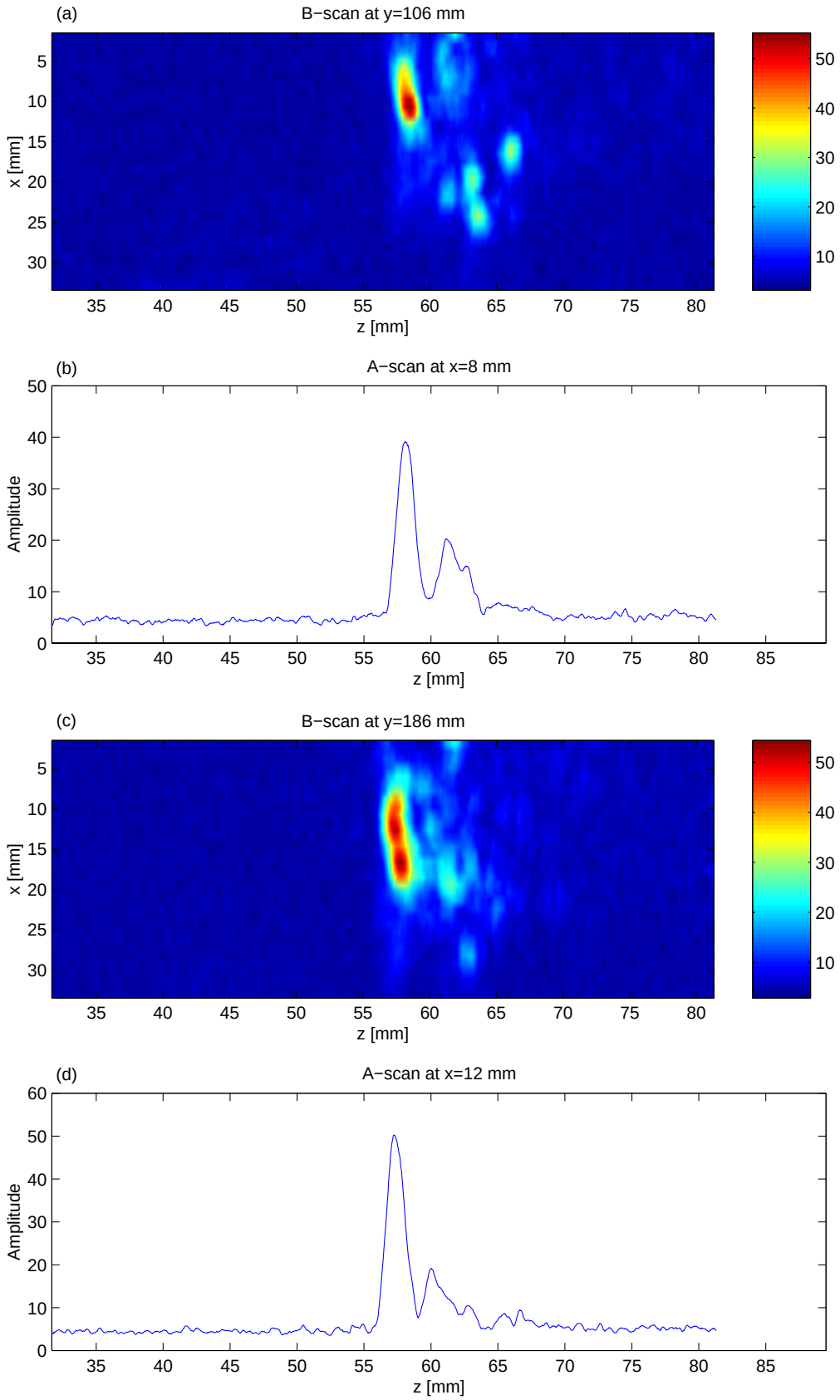

Fig. 1.10. The spatially compounded B- and A-scans that correspond to those in Fig. 1.4.

Now let us get into a more detailed investigation of the SDM. In Fig. 1.11, we show four images of the ultrasonic signals coming out of the 32 elements before forming the A-scans at four positions, namely, (a) $(x, y) = (7, 98)$ mm, (b) $(x, y) = (7, 129)$ mm, (c) $(x, y) = (8, 106)$ mm, (a) $(x, y) = (12, 186)$ mm. Making the phase-sensitive summation of the signals, we obtain the four A-scans that correspond to those in Figs. 1.3(b), 1.3(d), 1.4(b), and 1.4(d), respectively, and making the phase-insensitive summation, we have the A-scans corresponding to those Figs. 1.9(b), 1.9(d), 1.10(b), and 1.10(d), respectively. In Fig. 1.11, we can see that the backscattered ultrasound echoes received by the 32 elements form two vertical strips that look almost straight and should correspond to the scattering from the front and the back boundaries of the weld, respectively. Note that the color scaled levels are different in the images displayed. However, each strip, whether it is from the front or the back boundary, does not look uniform. For example, in Fig. 1.11(a), the echoes in the middle part of the front strip look stronger than those in the upper and lower parts, and the echoes along the back strip are becoming stronger from its upper end to its lower end; in Fig. 1.11(b), the two strips look not so obvious as in Fig. 1.11(a), (c) and (d). The reasons for these phenomena may arise from the irregular orientations of the boundaries at the places where they were insonified, the non-uniform solidification fronts, and the others.

Let us look at six spatial compounded local C-scans that correspond to those in Fig. 1.5 and shown Fig. 1.12(a)-(f), respectively. Fig. 1.12 also shows that the grain noise in the C-scans is largely suppressed and thus the images of the weld structure have been improved.

In comparison of the B- and C-scans before spatial compounded (Figs. 1.3-1.5) with those after spatial compounded (Fig. 1.9, 1.10 and 1.12), we see that the spatial resolution has become worse to different extents for ultrasonic imaging at different depths. This reveals that the grain noise suppression is gained at the price of the spatial resolution, i.e., the increased beam width. But this price is not so significant in the focal zone, e.g., the zone around z=60 mm in the present case, because the backscattered signals from the 32 elements in the focal zone are quite in phase and thus the phase cancellation is not so severe.

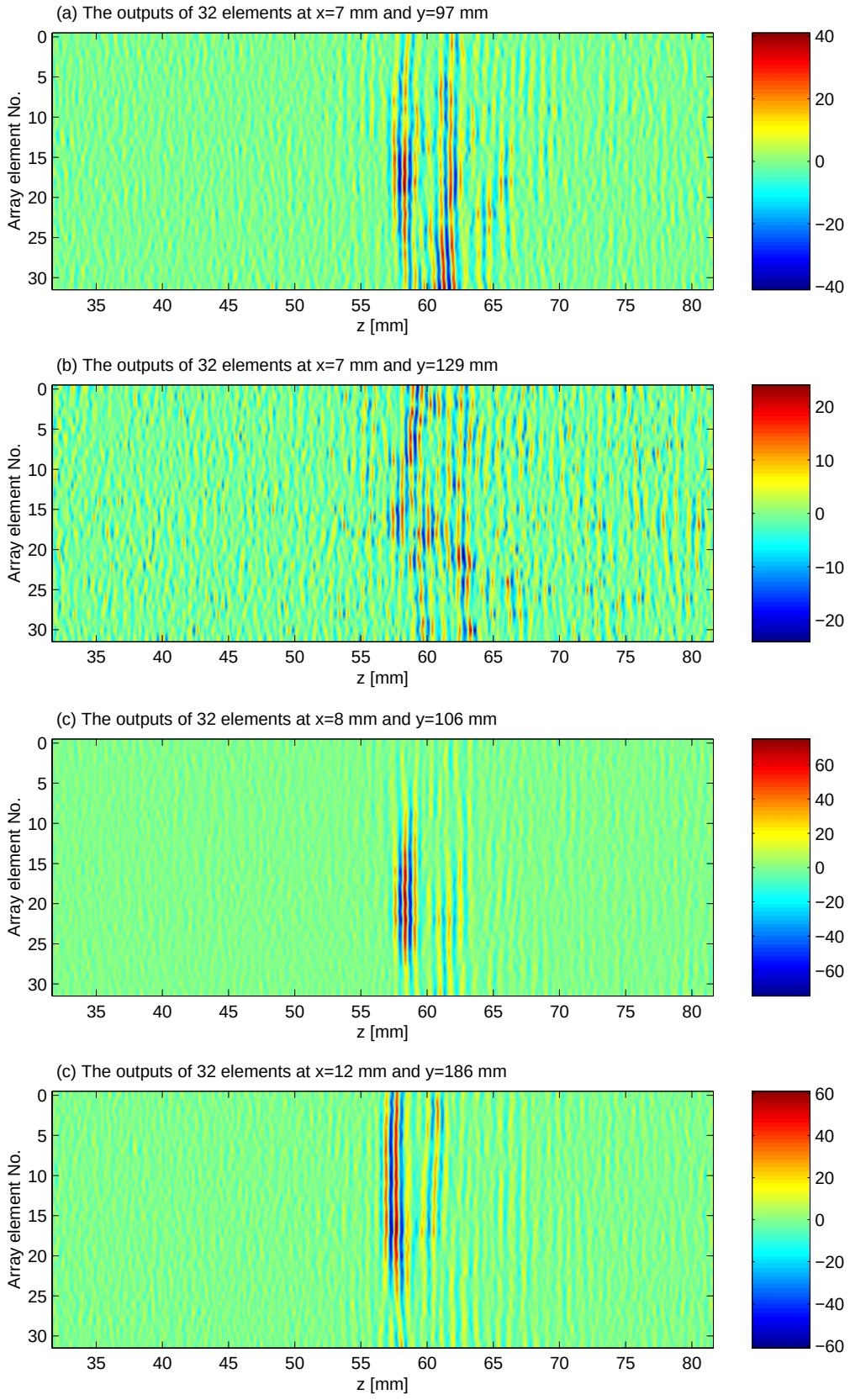

Fig. 1.11. The outputs of 32 elements before beam-forming the A-scans at four positions, (a) (*x*, *y*) = (7, 98) mm, (b) (*x*, *y*) = (7, 129) mm, (c) (*x*, *y*) = (8, 106) mm, (a) (*x*, *y*) = (12, 186) mm, which correspond to the positions in Figs. 1.3(b), 1.3(d), 1.4(b), and 1.4(d), or to the positions in Figs. 1.9(b), 1.9(d), 1.10(b), and 1.10(d), respectively.

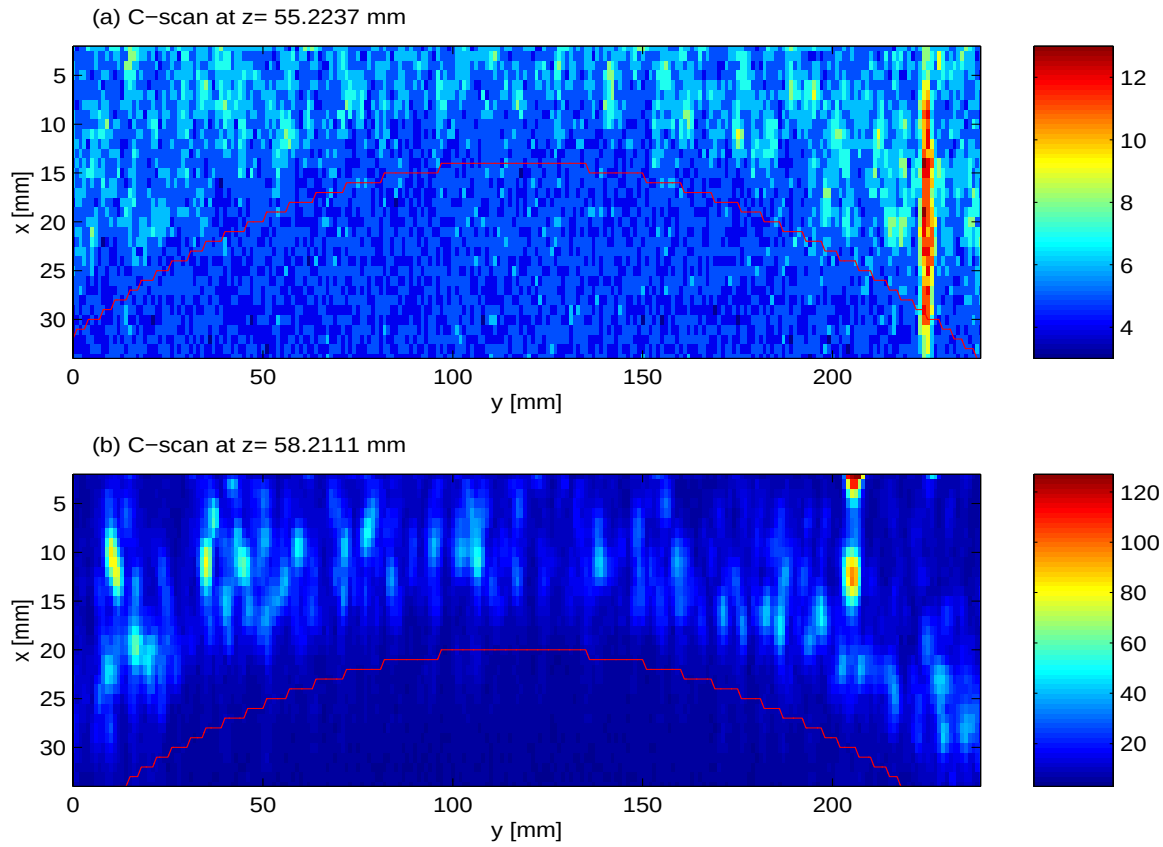
(a) C−scan at z= 55.2237 mm
x [mm]
y [mm]
5
10
15
20
25
30
0
50
100
150
200
12
10
8
6
4
(b) C−scan at z= 58.2111 mm
x [mm]
y [mm]
5
10
15
20
25
30
0
50
100
150
200
120
100
80
60
40
20

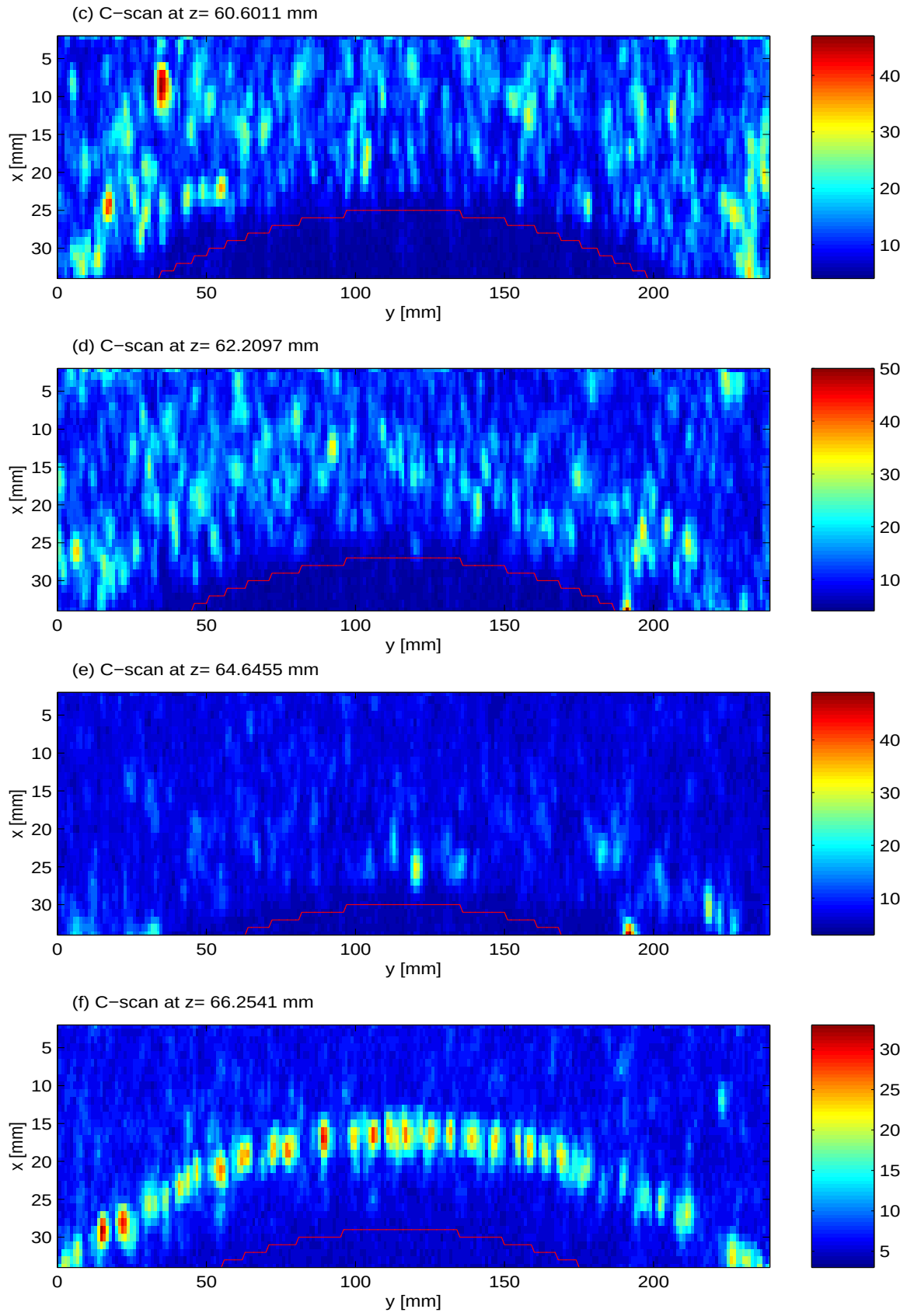

Fig. 1.12. Local C-scans after spatially compounding, which correspond to those in Fig. 1.5.

1.5.2 Clutter Suppression Filtering—Filter Bank Approach

The SDM method aims at suppressing the weld grain noise by means of spatial averaging. The cost paid for that approach, as discussed in the previous section, is a lower spatial resolution—which may not be critical if we only want to detect voids. Another approach is to design a filter for suppressing the clutter in the time domain (A-scans) instead of the spatial domain, without offering the spatial resolution. By comparing the spectra from a flat bottom hole (FBH) (which is Hole No. 13 in the non-welded zone and has a 1.5-mm diameter) and the weld in the CAN1 block, one can see that they look very similar (see Fig. 1.13). This looks discouraging—it seems difficult to filter out the weld clutter essentially located in the same frequency band as the FBH response. However, looking in the time domain (see Fig. 1.14), we can see that the FBH seems to have a slightly shorter response than the weld grains.

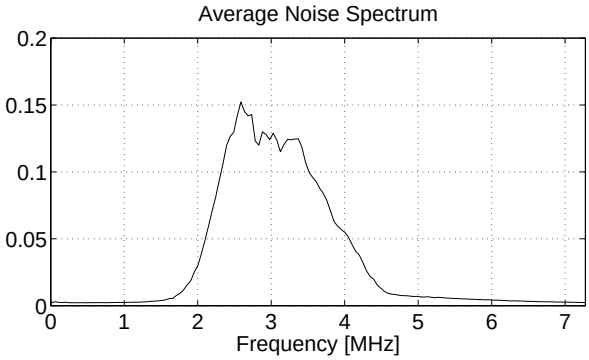

(a) Average weld clutter spectra from 15 B-scans in the CAN1 block.

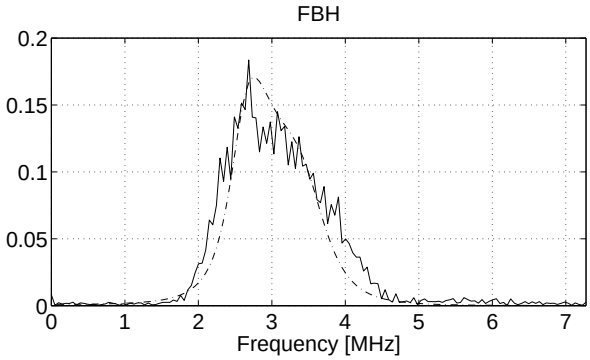

(b) Spectra from a single A-scan of an FBH in the CAN1 block (dash-dotted, Capon spectral method).

Fig. 1.13. Comparison of amplitude spectra from weld clutter and a flat bottom hole with a 1.5-mm diameter in the non-welded zone.

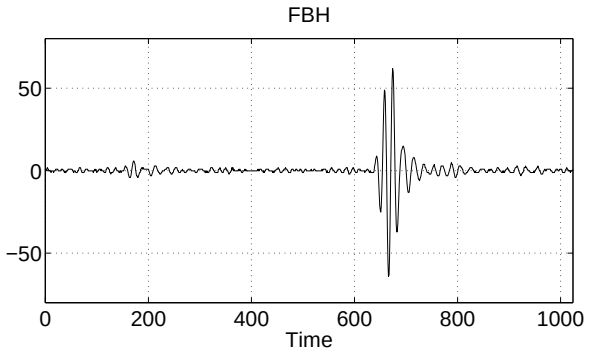

(a) Flat bottom hole

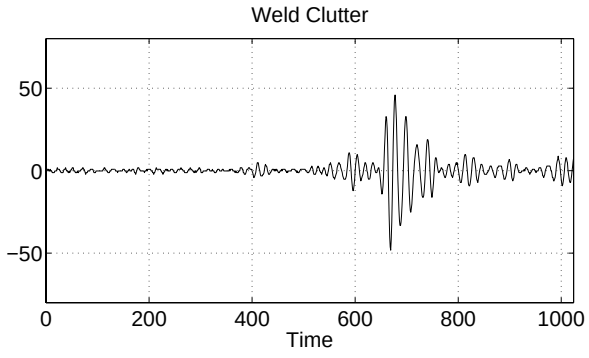

(b) Weld clutter

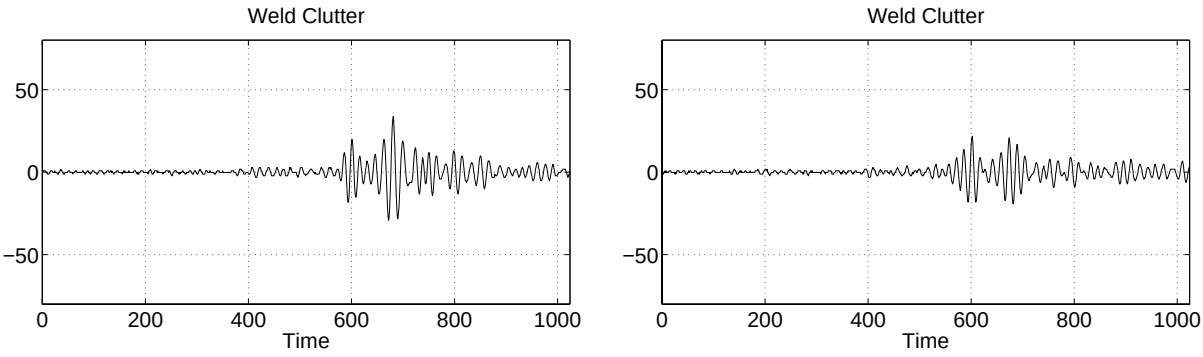

(c) Weld clutter (d) Weld clutter

Fig. 1.14. A-scans of a FBH and weld grains from the CAN1 block.

This might be explained by the fact that voids—especially FBHs—``shadow" deeper lying reflectors. This feature can by exploited to find a ``matched" filter which will emphasize the FBH (or void) response and suppress the grain noise. The question is how to find such a filter. One method is to use a bank of band-pass filters and select such a particular filter that gives the ``best" response in terms of S/N ratio. Other approaches based on statistics of the weld clutter and the response of voids would of course be desirable. However, this requires a rather large number of representative examples from both types of reflectors. Presently we have very few examples of voids, which makes this approach intractable. It is also difficult to verify what kind of reflectors that are present in a weld without destructive examination or radiographic methods. At the moment the only available well-defined reflectors are artificial defects, like drilled holes[1]. We, therefore, have to resort to the more heuristic filter bank approach consisting in the evaluation of the result by looking at filtered A-, B- or C-scans.

Filter banks have a close connection to time-frequency analysis and wavelet theory [23]. The wavelet transform is basically a bank of band-pass filters—, which are orthogonal for the discrete wavelet transform (DWT). In this application we have used the *continuous wavelet transform* (CWT) as a tool to find a FIR filter with the desired properties described above. Wavelet filters are based on a single prototype filter, called ``mother wavelet", which are scaled and shifted to construct a bank of filters simultaneously filtering the signal. Applying the CWT to a signal (column vector) x gives a two-dimensional result (matrix) X, where one dimension is time (shifts) and the other is scale, that is the size (length) of the wavelet filter. Fig. 1.15 shows three examples of wavelet filters.

Fig. 1.16 shows the CWT of an A-scan containing the response from an FBH and the CWT of an A-scan containing clutter, filtered with the Sombrero filter in Fig. 1.15 (b).

[1]It is also a difficult task to detect voids in our test blocks with radiography.

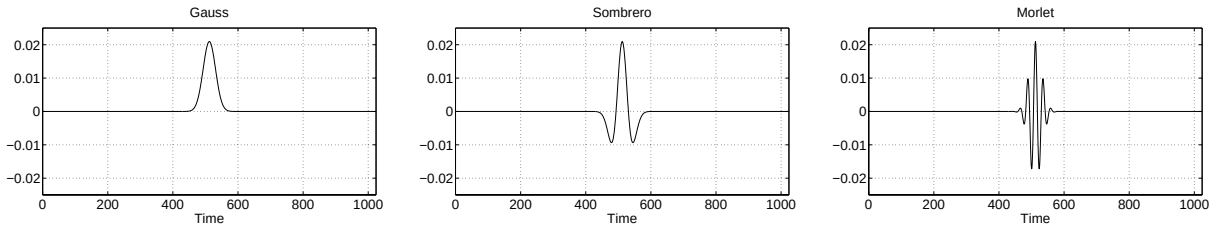

(a) The Gauss filter. (b) The Sombrero filter. (c) The Morlet filter.

Fig. 1.15. Three examples of mother wavelets for the continuos wavelet transform.

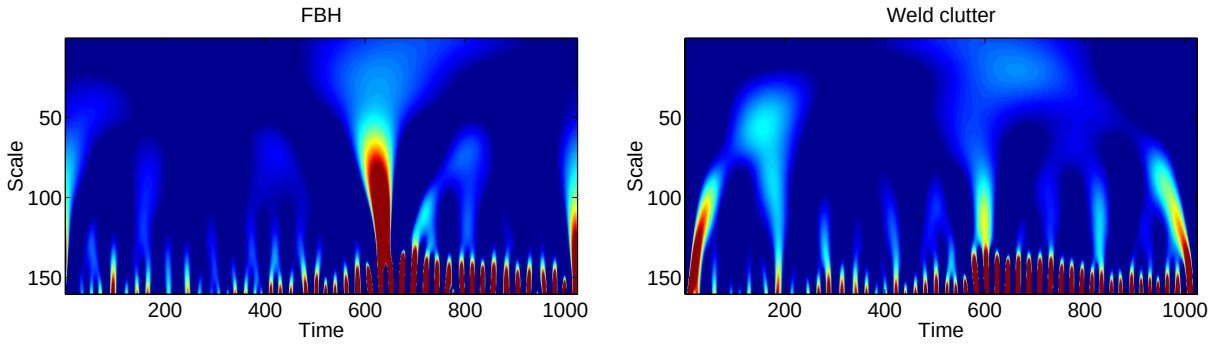

(a) Flat bottom hole. (b) Weld grains.

Fig. 1.16. The CWT of A-scans from a FBH and weld grains from the CAN1 block.

Images like those in Fig. 1.16 give a quick view of where, and at which ``scale", a signal has significant energy. Since the CWT is a convolution of the wavelet filter with the analyzed signal, the response is dependent on the similarities (i.e. the correlation) of the wavelet filter and the signal. These features make wavelets a very useful tool for analyzing transient signals encountered in, for example, US testing. In this application we are basically interested in distinguishing between two types of transients—void transients (defect reflections) and ``other" transients. In this first attempt, the filter (mother wavelet) has not been chosen based on any physical reasoning, only the pre-defined filters shown in Fig. 1.15 have been studied. However, despite this ad hoc procedure the amplitude of the CWT of the FBH signal is significantly larger for scales around 80–130 compared to the corresponding one for the weld clutter signal (Fig. 1.16). The A-scans are shown in Fig. 1.17 both before and after filtering with the Sombrero filter corresponding to scale 120. The frequency response of the Sombrero filter is shown in Fig. 1.18. Note that the filter is much lower frequent than the spectra for the received signals shown in Fig. 1.13. In order to further examine this property a low-pass FIR filter with approximately the same cut-off frequency as the wavelet filter shown in Fig. 1.19 was constructed. The impulse response is quite similar to the wavelet filter and the filtering results are very similar as well.

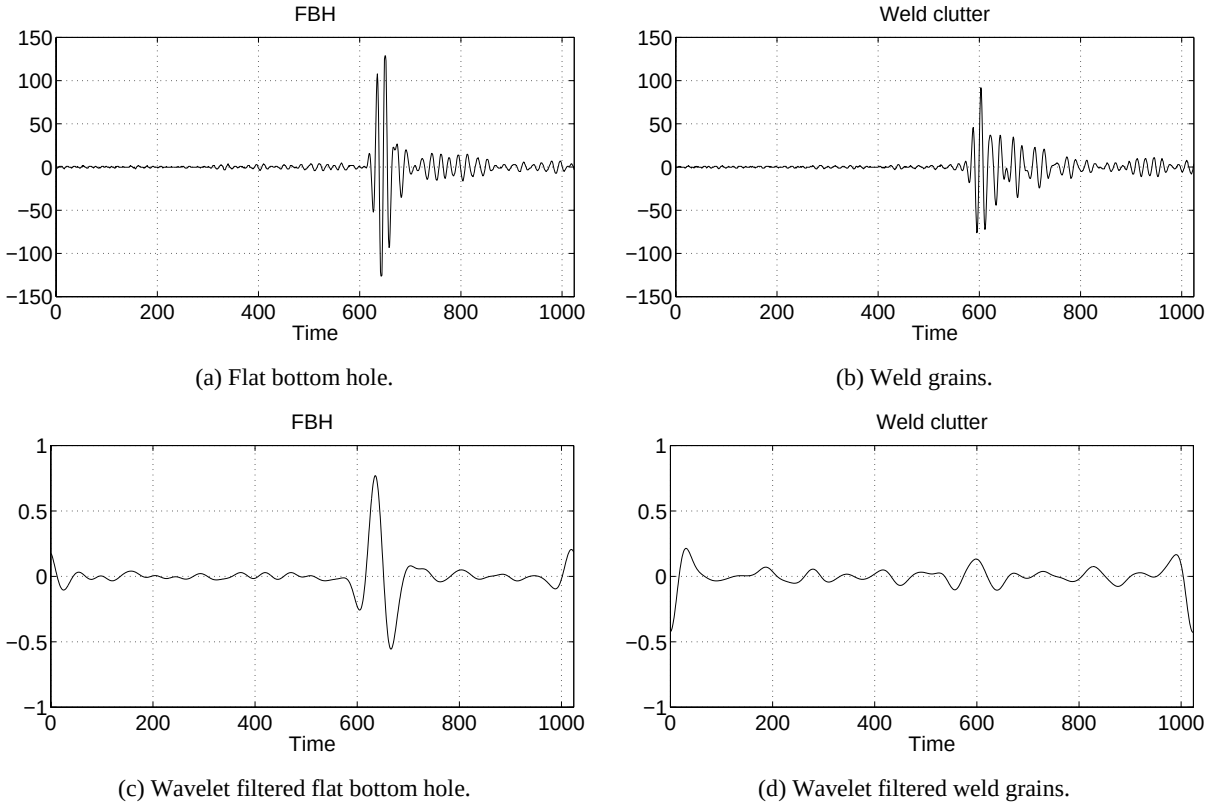

(a) Flat bottom hole.

(b) Weld grains.

(c) Wavelet filtered flat bottom hole.

(d) Wavelet filtered weld grains.

Fig. 1.17. A-scans from a FBH and weld grains from the CAN1 block unfiltered and filtered with the Sombrero filter at the scale corresponding to 120 in Fig. 1.16.

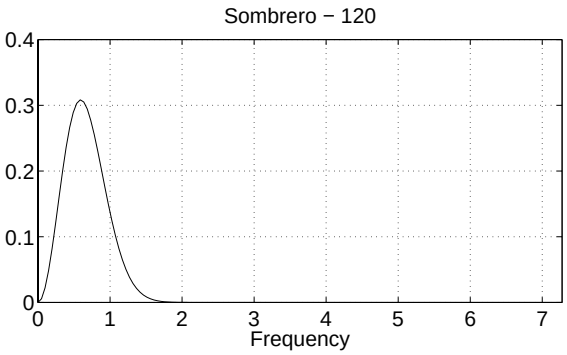

Fig. 1.18. Amplitude spectrum for the Sombrero filter.

One example C-scan from Block 3 of canister Weld123 is shown in Figs. 1.20 and 1.21. One can see that the clutter has been substantially suppressed. However, since this is an example taken from a real weld – no artificial defects – it is not clear whether all suppressed echoes are clutter or actual defects. As this research is at the early stage, no fine tuning—except manual tuning—has been performed. Although the results are very encouraging it should be stressed that the wavelet filter has been applied to a very limited number of examples and further evaluation of the performance is needed.

Further research will include searching for a physical explanation of the results and, if possible, better tuning the filters. We are also planning to inspect the copper weld specimens with a lower center frequency focused transducer with a similar center frequency as the wavelet filter.

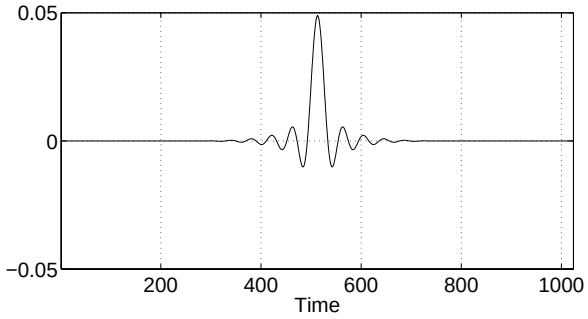

(a) Impulse response.

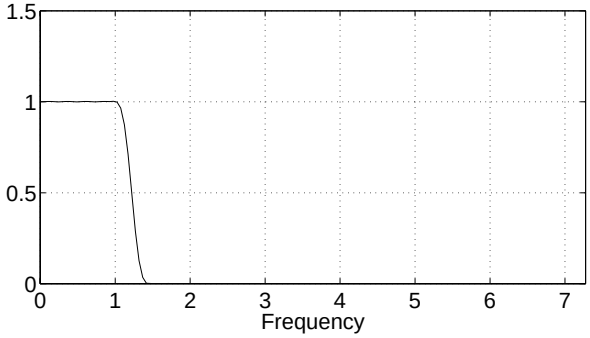

(b) Frequency response.

Fig. 1.19. A linear phase FIR low-pass filter with approximately the same cut-off frequency as the wavelet filter.

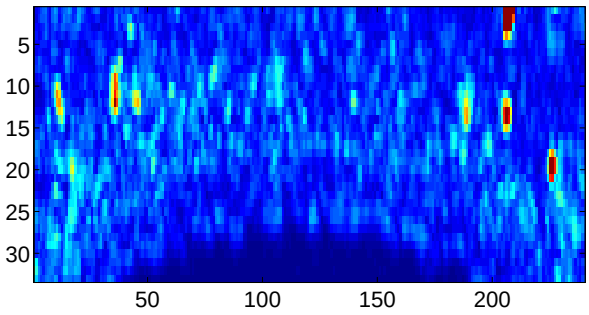

(a)

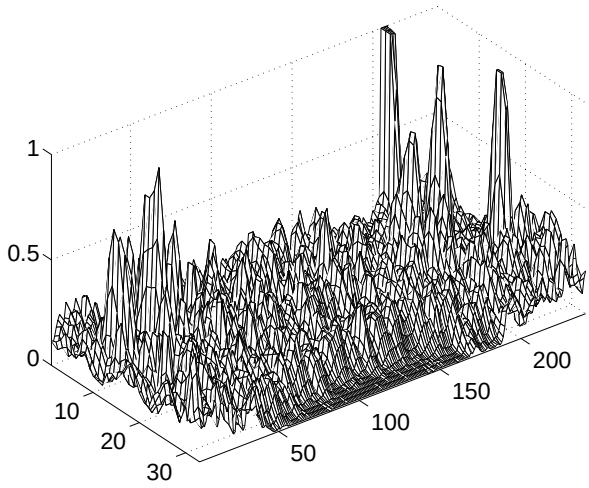

(b)

Fig. 1.20. Original C-scan from the Weld123-3 block using 32 elements.

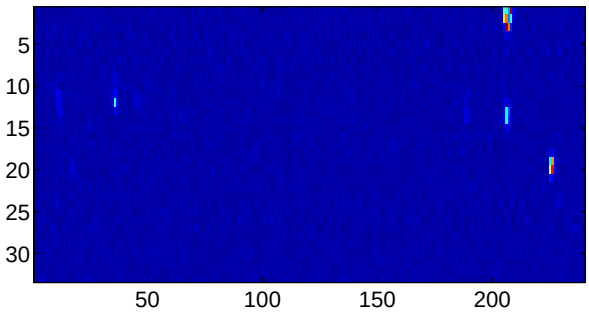

(a)

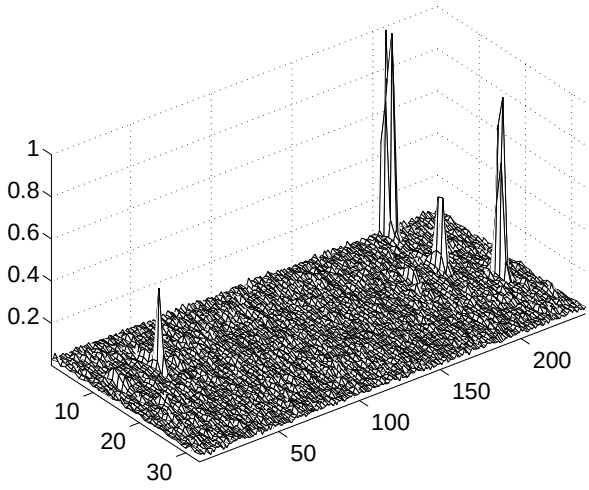

(b)

Fig. 1.21. Filtered C-scan from Weld123-3 block using 32 elements.

1.6 Conclusions and future work

To evaluate EB welds, we started from a brief introduction of EB welds and their structure, then we have made a systematic analysis of ultrasonic interaction and imaging of an EB weld, conducted analysis and extraction of features on grain noise and backscattering from EB welds, then implemented grain noise suppression based on the feature of grain noise, and finally realized flaw-detection enhancement by means of wavelet transform.

Having gained a deep insight into ultrasonic interaction of an EB weld, an EB weld is thought of as a multi-layered medium that is embedded in a parent medium and contains grains different from its parent medium. From ultrasonic imaging of a EB weld, e.g., B-scans and local C-scans, we can get transverse and longitudinal view of the weld structure that is basically in accordance with that reported by Sanderson *et al* [1]. The boundaries between the parent material and the HAZ and between the HAZ and the fusion zone can be seen although they do not look continuously- and well-defined in the ultrasonic images. Refraction at the boundaries and weld anisotropy may have significant effect on ultrasound at the weld tip, and thus may cause imaging distortion, e.g., the weld bending at the weld tip and the others.

Some features on grain noise and backscattering from a EB weld have been analyzed. From the analysis of histograms of the weld ultrasonic image, the phenomenon has also been shown that the porosity tended to be concentrated towards the upper side of a HV weld, and a guideline on how to select the gates for creating C-scans has been proposed.

Due to the randomness of grain noise, the SDM has shown its ability to suppress grain noise both in the parent material of an EB weld and in the weld so that the weld ultrasonic image can be significantly improved. The suppression is achieved at the price of reduced spatial resolution.

To enhance flaw detection, wavelet filters have been studied. An FIR filter, called Sombrero filter, has been found to yield encouraging results of clutter suppression. However, the physical explanation for the results is still missing and needs exploring.

On the whole, these researches are still at the early stage. In future, we will exploit other means to extract more features on EB welds, deal with the filter design and parameter tuning, and inspect the copper canisters using a focused transducer with a lower center frequency that is similar to the wavelet filter.

1.7 References

[1] A. Sanderson, TF Szluha, C N Ribton, B G Dance and A B Day, *The Application of High Power Non-Vacuum EB Welding for Encapsulation of Nuclear Waste at Reduced Pressure*, SKB Inkapsling, Projektrapport 94-01, January 1994.

[2] T. Stepinski, and P. Wu, *Ultrasonic Inspection of Nuclear Fuel Copper Canisters*, SKB Projektrapport 97-01, December 1996.

[3] T. Stepinski, and P. Wu, *Inspection of Copper Canisters for Spent Nuclear Fuel by Means of Ultrasonic Array System*, SKB Projektrapport 97-06, Augusti 1997.

[4] P. Wu, and T. Stepinski, *Inspection of Copper Canisters for Spent Nuclear Fuel by Means of Ultrasonic Array System - Modelling, Defect Detection and Grain Noise Estimation*, SKB Projektrapport, Augusti 1998.

[5] H. Schultz, *Electron Beam Welding* (Abington Publishing, Cambridge, 1993).

[6] E.P. DeGarmo, J.T. Black, and R. A. Kohser, *Materials and Processes in Manufacturing* (Macmillan Publishing Company, New York, 1990), 7th Edition, Chap. 36, p. 911-928, and Chap. 39, p. 951-961.

[7] J.F. Lancaster, *Metallurgy of Welding* (Chapman & Hall, London, 1993), 5th ed.

[8] A.B. Day, *An Investigation into Optimisation of NDT of Spent Nuclear Canisters - Phase III*, TWI Report No. 220343/1/95, April 1995.

[9] L.J. Busse, and J.G. Miller, "A comparison of finite aperture phase sensitive and phase insensitive detection in the near field of inhomogeneous material," *IEEE 1981 Ultrason. Symp. Proc.*, pp. 617-626, 1981.

[10] M. O'Donnell, "Phase-insensitive pulse-echo imaging," *Ultrason. Imaging*, vol. 4, pp. 321-335, 1982.

[11] M.S. Patterson, and F.S. Foster, "The improvement and quantitative assessment of B-mode images produced by an annulararray/cone hybrid," *Ultrason. Imaging*, vol. 5, pp. 195-213, 1983.

[12] A.T. Kerr, M.S. Patterson, F.S. Foster, and J.W. Hunt, "Speckle reduction in pulse echo imaging using phase insensitive and phase sensitive signal processing techniques," *Ultrason. Imaging*, vol. 8, pp. 11-28, 1986.

[13] H. Song, P. Wu, R.M. Schmitt, and W. Thomas, "Correction of the artifact of the intensity distortion in the ultrasonic B-mode imaging with a phase insensitive method," *IEEE 1993 Ultrason. Symp. Proc.*, pp. 1195-1198, 1993.

[14] W. Thomas, R.M. Schmitt, and P. Wu, "Quantitative tissue characterization by means of phase insensitive signal processing," *IEEE 1994 Ultrason. Symp. Proc.*, pp. 1437-1440, 1994.

[15] M. Berson, A. Roncin, and L. Pourcelot, "Compounding scanning with an electronically steered beam," *Ultrason. Imaging*, vol. 3, pp. 303-308, 1981.

[16] D.P. Shattuck, and O.T. von Ramm, "Compounding scanning with a phased array," *Ultrason. Imaging*, vol. 4, pp. 97-107, 1982.

[17] P.M. Shankar, and V.L. Newhouse, "Speckle reduction with improved resolution in ultrasound images," *IEEE Trans. Ultrason. Ferroelec. Freq. Contr.*, vol. UFFC-32, pp. 537-543, 1985.

[18] P.M. Shankar, "Speckle reduction in ultrasound B-scans using weighted averaging in spatial compounding," *IEEE Trans. Ultrason. Ferroelec. Freq. Contr.*, vol. UFFC-33, pp. 754-758, 1986.

[19] G.E. Trahey, S.W. Smith, and O.T. von Ramm, "Speckle pattern correlation with lateral aperture translation: experimental results and implications for spatial compounding," *IEEE Trans. Ultrason. Ferroelec. Freq. Contr.*, vol. UFFC-33, pp. 257-264, 1986.

[20] S.W. Smith, and O.T. von Ramm, "The maltese cross processor: speckle reduction for circular transducers," *Ultrason. Imaging*, vol. 10, pp. 153-170, 1988.

[21] J.J. Giesey, P.L. Carson, D.W. Fitting, and C.R. Meyer, "Speckle reduction in pulse-echo ultrasonic imaging using a two-dimensional receiving array," *IEEE Trans. Ultrason. Ferroelec. Freq. Contr.*, vol. 39, pp. 167-173, 1992.

[22] S.K. Jespersen, J.E. Wilhjelm, and H. Sillesen, "Multi-angle compounding," *Ultrason. Imaging*, vol. 20, pp. 81-102, 1998.

[23] G. Strang, and T. Nguyen, *Wavelets and Filter Banks* (Wellesley-Cambridge Press, Wellesley MA, USA, 1996).

2 Modeling of ultrasonic fields from the ALLIN linear array with cylindrically curved surface

2.1 Introduction

During the past five years, we have been developing and upgrading the modeling tool that is mainly oriented to linear arrays. Up to now, the modeling tool can simulate acoustic and elastic fields from planar linear arrays [1-5], planar phased arrays [6,7], and concave arrays [6], and acoustic fields from the ALLIN array, a linear arrays with a cylindrically curved surface [8,9]. The theory used in the modeling tool, basically, is the angular spectrum approach (ASA), although some other methods have been used in combination [6,8,9]. To further upgrade the modeling tool, we have done the work this year in the following aspects:

(i) developing a novel, and efficient method of calculating the spatial impulse response (SIR) of the ALLIN array to determine the pulse excitation of the array;

(ii) calculating elastic fields radiated by the ALLIN array into immersed solids.

To quantitatively calculate ultrasonic fields from the array or to quantitatively estimate ultrasonic attenuation in copper canisters, it is necessary to have a precise pulse excitation of the ALLIN array. Last year the ASA had been extended to arbitrarily curved transducers and arrays, and thus the modeling of pulse-echo fields radiated by the ALLIN array into a fluid was able to be implemented and the modeled results were compared with the measurements [8,9]. To calculate the pulse-echo fields, the pulse excitation on the array surface was needed and usually obtained using deconvolution technique, specifically, deconvolving a measured echo with the spatial impulse response (SIR) of the array at the measurement point. Therefore, we started developing a method for computing the SIR, and had created a very preliminary form of the method that was a single integral for the on-axis case and not efficient. Also for the convenience of computer simulation, we formulated an analytical function that approximately modeled measured pulse-echoes, and further obtained the pulse excitation based on the deconvolution of the analytical function [8]. However, this analytical measurement model did not yield the accurate prediction of pulse-echo fields in comparison with the measured ones. In the present work, we have developed a novel, and efficient method of calculating the SIR of the ALLIN array to determine its pulse excitation, then applied the pulse excitation to the calculation of acoustic pulse-echo fields in water, and finally compared the calculations with measurements. This work is presented in Sect. 2.2. Using the pulse excitation, we have further calculated elastic fields radiated by the ALLIN array into a copper canister in immersion inspection. The results are presented in Sect. 2.3. The pulse excitation has also been used in the next chapter in calculating the pulse echoes

from attenuating copper plates for the log-spectral difference method to quantitatively estimate attenuation with diffraction correction.

2.2 Acoustic fields

2.2.1 Review of the spatial impulse response method (SIRM)

A number of different methods for computing ultrasonic transient fields have been developed up to now. An excellent review of transient field theory for baffled planar pistons was given by Harris [11]. The spatial impulse response method (SIRM) seems to have become a most powerful tool to calculate transient radiation since it was proposed by Tupholme [12] and Stepanishen [13,14]. The method has been applied extensively to the case of planar transducers with both uniform [11-24] and nonuniform [16,25-27] excitations and also to the case of curved transducers [16, 25, 27-33]. In the case of uniform planar transducers, the spatial impulse response (SIR) can be obtained for a few different shaped apertures, such as circular pistons [11-18], rectangular transducers [18-21], and triangular apertures [22], segmented annular apertures [23], and arbitrarily shaped transducers [24]. In the case of curved transducers, the SIRM has been applied to the cases of focusing transducers with spherically curved surfaces [16,28-30], conical surface [41], spherically curved strip [32], axisymmetric nonuniform surface velocity distribution [33], concave cylindrical transducers [34], and rectangular strip-like focusing transducers [35], and arbitrarily shaped transducers [25]. The analytic forms of spatial impulse responses are available only for circular pistons [11-18], rectangular transducers [20,21], triangular apertures [23], spherical radiators [28,29], and conical radiators [31]. The SIRM has also been applied to predicting pulse-echo fields from planar transducers [41-44].

Some relevant works, e.g., presented by Theumann *et al* [34] and by Reibold and Kazys [35], need special mentioning here. Using the SIRM, Theumann *et al* [34] dealt with a transducer that had the geometry of a concave cylinder and radiated an acoustic field inside the cylinder. They reduced the surface integral of the impulse response into a single integral (an elliptic integral) and obtained the impulse response by means of numerical integration. On the cylinder axis, the impulse response was given in analytic form. Reibold and Kazys [35] applied the SIRM to the calculation of the radiation by a rectangular strip-like focusing transducer with a cylindrically concave surface, the same geometry as the transducer that we deal with in the present work. However, they essentially treated the concave, rectangular transducer as a plane transducer that was subdivided into a set of elementary strips on which the appropriate phase shifts were imposed. The concave, rectangular transducer treated in such a way is equivalent to a planar "linear array" that consists of the same set of such elementary strips and has the imposed time delays corresponding the same phase shifts. Therefore, the impulse response

obtained in such a way was not the one of the cylindrically concave, rectangular transducer, but the one of the "linear array". Another possible solution to the rectangular transducer with a cylindrically curved surface is the method proposed by Jensen and Svendsen [35], who used the idea similar to Ocheltree and Frizzell's [45], cutting an aperture into a large number of small rectangular elements so that the farfield approximation holds for each rectangular element at one certain frequency, and then using the farfield SIR of a rectangular aperture given by Stepanishen [13,14]. They applied the method to a spherically concave transducer. However, this method can be inefficient, especially for the field points close to a transducer surface and in the focal zone. For field points close to the transducer surface the transducer must be cut into a large number of small rectangles so that the farfield approximation holds for the highest frequency component of an impulse response, and in the focal zone the SIR becomes very narrow so that the highest frequency can be very high, e.g., the SIR is a δ impulse at the focal point of a spherical cap transducer. Also, the farfield-approximation-based rule for choosing the sizes of the small rectangular elements is ambiguous and uncertain because the widths of the SIRs at different field points vary over very large range, and the criterion for choosing the highest frequency can be difficult to determine.

A thorough literature review (partly presented above) reveals that the SIRM has, so far, not been used for simulating acoustic fields radiated by cylindrically curved, rectangular transducers and linear arrays consisting of cylindrically curved, rectangular elements. Determining the SIR of linear arrays that have cylindrically curved surfaces is of particular interest in the present work because it is the key to the SIRM for the evaluation of transient fields. In this section we present a novel approach to calculating the SIR of rectangular transducers and linear arrays with curved surfaces, which makes it possible to predict the pulse-echo fields from the array. The pulse-echo fields mean the fields radiated by the array, diffracted by a point-like scatterer, and received by the same array. The general theory underlying the approach is given in Sect. 2.2.2 and applied to the above-mentioned linear arrays. An example of a calculated impulse response of such an array is presented in Sect. 2.2.3. The simulated and measured results are compared in Sect. 2.2.4. The analytic form of the SIR of such a curved, rectangular transducer is available in some special case and its derivation is given in Appendix 3-B.

2.2.2 Theory

A. General description of the spatial impulse response method

It is well known that a sound field from a baffled planar piston source in a fluid can be rigorously depicted by the Rayleigh integral. For a curved source the Rayleigh integral can approximately represent the radiation of the curved source under certain conditions, where the diameter of the source is large compared to the wavelength, and the source is only slightly curved. The secondary diffraction under these conditions can, thus, be neglected. This was shown by O'Neil [36] early in 1947, and later

pointed out by Penttinen and Luukkala [28] and Arditi, *et al* [29]. Several experimental studies [37-39] and numerical investigations [40] have shown that the O'Neil theory agrees very well with experiments and a more exact model for focused transducers. Thus, the O'Neil theory does seem to be a good basis for evaluating focused transducers.

For a source with a radiating surface *S* and a transient normal particle velocity, $v_n(t)$, on surface *S*, the Rayleigh integral for time dependent velocity potential $\phi(\mathbf{r},t)$ is given by [11,29]

$$\phi(\mathbf{r},t) = \int_S \frac{v_n\left(t - |\mathbf{r}-\mathbf{r}_s|/c\right)}{2\pi|\mathbf{r}-\mathbf{r}_s|} dS \,, \tag{2.1}$$

where $\mathbf{r}_s$ and $\mathbf{r}$ are the source and field points, respectively, and *c* is the sound speed in the medium.

If all the points on the source vibrate with equal amplitude and in phase, i.e., the source is a uniformly vibrating piston, Eq. (2.1) can be written (see e.g., [11-14]),

$$\phi(\mathbf{r},t) = v_n(t) * h(\mathbf{r},t) \,, \tag{2.2}$$

where * stands for the convolution in time and $h(\mathbf{r},t)$ is called its impulse response [13,14] or, alternatively, spatial impulse response (SIR) [11], which is defined as

$$h(\mathbf{r},t) = \int_S \frac{\delta\left(t - |\mathbf{r}-\mathbf{r}_s|/c\right)}{2\pi|\mathbf{r}-\mathbf{r}_s|} dS = \int_S \frac{\delta\left(t - r'/c\right)}{2\pi r'} dS \,, \tag{2.3}$$

where $r' = |\mathbf{r}-\mathbf{r}_s|$. The pressure field at point $\mathbf{r}$ can be obtained from the relation,

$$p(\mathbf{r},t) = \rho \frac{\partial \phi(\mathbf{r},t)}{\partial t} = \rho \frac{\partial \left[v_n(t) * h(\mathbf{r},t)\right]}{\partial t} \,, \tag{2.4a}$$

or

$$p(\mathbf{r},t) = \rho v_n(t) * \frac{\partial h(\mathbf{r},t)}{\partial t} = v_n(t) * h_p(\mathbf{r},t) \,, \tag{2.4b}$$

where ρ is the density of the medium, and

$$h_p(\mathbf{r},t) = \rho \frac{\partial h(\mathbf{r},t)}{\partial t} \,, \tag{2.4c}$$

which is usually referred to as the pressure spatial impulse response [16,20,41-44]. This is the so-called SIRM.

The SIRM has also been applied to predicting pulse-echo fields from planar transducers, that is, the fields radiated by a transducer, diffracted by a rigid point-like scatterer, and received by the same transducer (see [41,43]). It is also employed here to predict the pulse-echo fields from a linear array with a cylindrically concave surface. Assuming that a transducer works as a receiver that is uniformly pressure sensitive in the effective frequency range of a signal, its voltage output when used in pulse-echo mode to receive the echo from a rigid point-like scatterer is given by [41,42,46]

$$e(t) = e_0 v_n(t) * h_p(\mathbf{r},t) * h_p(\mathbf{r},t) \tag{2.5}$$

where e_0 is a proportional constant.

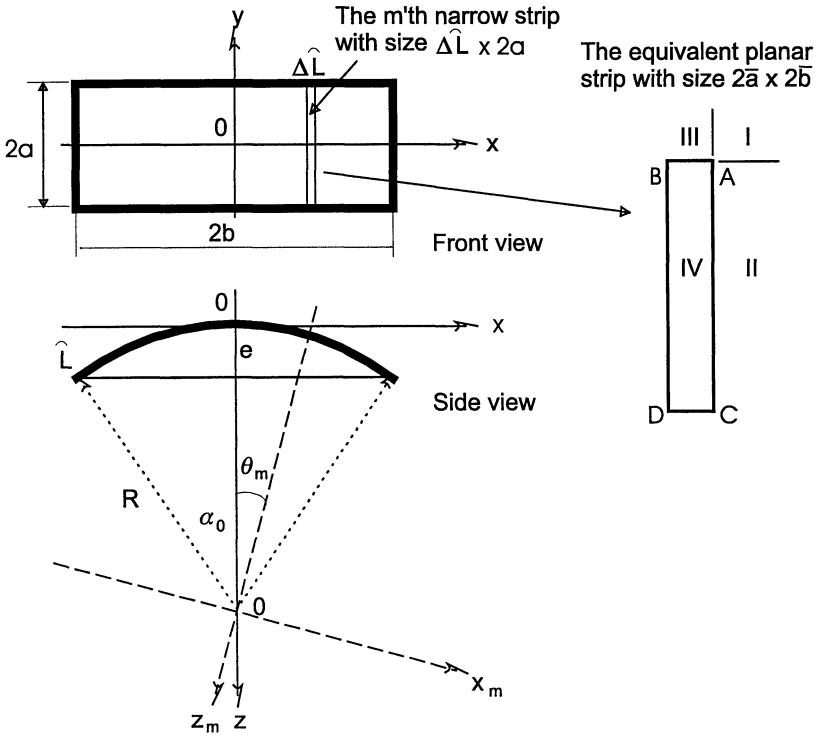

Fig. 2.1. Geometry of the rectangular aperture with cylindrically curved surface, and the four regions I, II, III, and IV in which the SIR of the (planar) sub-aperture is defined and listed in Table A2.1 in Appendix 3-A.

From the above formulation, it can be seen that, to predict a field radiated by a source, the normal velocity on the source surface and the SIR of the source need to be known. The normal velocity can be determined experimentally (see e.g., [42,44]); this will be discussed in the next section.

Determination of the SIR of velocity potential in Eq. (2.3), therefore, is the key to the SIRM. As mentioned in the Introduction, the spatial impulse responses are available in analytic form for some special cases only. However, the SIRs of a rectangular aperture and a linear array with cylindrically curved surface, which are among the most commonly-used transducers and arrays in NDT and medical imaging, are not available yet. Here an approach to determining the SIRs of a rectangular aperture and a linear array, both with a cylindrically curved surface, is proposed.

B. Spatial impulse response of a cylindrically curved, rectangular aperture

The geometry of a cylindrically curved, rectangular aperture is shown in Fig. 2.1. The idea of finding the SIR of the aperture is as follows: first subdivide the aperture in the *x*-direction into a set of such narrow strip sub-apertures that each sub-aperture can be approximated by a planar rectangle (see Fig. 2.1), and then sum up the SIRs of all these sub-apertures. Obviously, the narrower the strips the more exact the SIR of the aperture obtained. Since the SIR of a planar rectangular aperture is available in an analytic form [20], the SIR of the cylindrically curved, rectangular aperture is easily found by the summation of these analytic SIRs of narrow strips. For a planar rectangular aperture with size $2\bar{a}\times 2\bar{b}$, its SIR, denoted by $h_{\text{rect}}(\mathbf{r},t)$, is listed in Table A2.1 in Appendix 3-A.

Assuming that the cylindrically curved, rectangular aperture has dimension $2a\times 2b$ and radius of curvature *R*, the half angle, α_0, subtended by chord *2b* (see Fig. 2.1) can easily be found to be

$$\alpha_0 = \arcsin(b/R)\,, \tag{2.6}$$

and the arc length spanning over chord *2b* is

$$\hat{\mathrm{L}} = 2\alpha_0 R\,. \tag{2.7}$$

Supposing that the cylindrically curved, rectangular aperture is subdivided into *M* sub-apertures of narrow strips with length 2*a* (see Fig. 2.1), the arc width of each sub-aperture is

$$\Delta\hat{L} = \hat{L}/M\,, \tag{2.8}$$

and the angle subtended by $\Delta\hat{L}$ is

$$\Delta\alpha = 2\alpha_0/M\,. \tag{2.9}$$

For a large *M*, $\Delta\hat{L}$ can be approximated by its chord ΔL which expressed as

$$\Delta L = R\sin(\Delta\alpha/2). \tag{2.10}$$

Each sub-aperture is, therefore, approximately planar with dimension of $2\bar{a}\times 2\bar{b} = \Delta L \times 2a$. The angle subtended by the arc from the center of the m'th sub-aperture to the z-axis is

$$\theta_m = -\alpha_0 + \Delta\alpha(m-1/2),\ (m=1,\ \ldots,\ M). \tag{2.11}$$

To facilitate the calculation of SIR, the coordinate transform is applied to each sub-aperture. For the m'th sub-aperture, the coordinates (x_m, y_m, z_m) are transformed into the coordinates (x, y, z) through the following transformation,

$$\begin{bmatrix} x_m \\ y_m \\ z_m \end{bmatrix} = \begin{bmatrix} \cos\theta_m & 0 & \sin\theta_m \\ 0 & 1 & 0 \\ -\sin\theta_m & 0 & \cos\theta_m \end{bmatrix} \begin{bmatrix} x \\ y \\ z-R \end{bmatrix}, \tag{2.12}$$

which means that the $x_m - y_m - z_m$ coordinate system is obtained in such a way that the x-y-z coordinates are first translated by R in the z-direction, and then rotated clockwisely by θ_m in the x-z plane. Obviously, all the sub-apertures in the $x_m - y_m - z_m$ coordinates are located at point $(0,0,-R)$. Therefore, the SIR of the cylindrically curved, rectangular aperture can be obtained from the superposition of the SIRs of all M sub-apertures in the following manner,

$$h(\mathbf{r},t) = \sum_{m=1}^{M} h_{rect}(\mathbf{r}_m, t), \tag{2.13}$$

where $\mathbf{r}_m = (x_m, y_m, z_m)$, and $h_{rect}(\mathbf{r}_m, t)$ is the SIR of the m'th planar, rectangular aperture with dimension of $2\bar{a}\times 2\bar{b} = \Delta L \times 2a$, and is available in analytic form (refer to Table A2.1 in Appendix 3-A).

C. Spatial impulse response of a linear array with cylindrically concave surface

The linear array considered here is schematically shown in Fig. 2.2. It consists of N elements which are all $2a\times 2b$ rectangles with cylindrically concave surface having radius of curvature, R. The center of the i'th element is located at $y_i = (i - N/2 - 1/2)d$ where i = 1, 2, …, N, and d is the spacing of the adjacent elements. Assuming that the element centered at the origin has the SIR

$h_0(\mathbf{r},t)$, which can be obtained from Eq. (2.13), the SIR of the i'th element, $h_i(\mathbf{r},t)$, can be easily found by shifting $h_0(\mathbf{r},t)$ along the y axis according to the relation $y_i = (i - N/2 - 1/2)d$, i.e., $h_i(x,y,z,t) = h_0(x,y-y_i,z,t)$. When all the elements are excited simultaneously with the same electronic pulse, that is, without electronic focusing, the SIR of the linear array can be written as

$$h(\mathbf{r},t) = \sum_{i=1}^{N} h_i(\mathbf{r},t) = \sum_{i=1}^{N} h_0(x,y-y_i,z,t)\,. \tag{2.14}$$

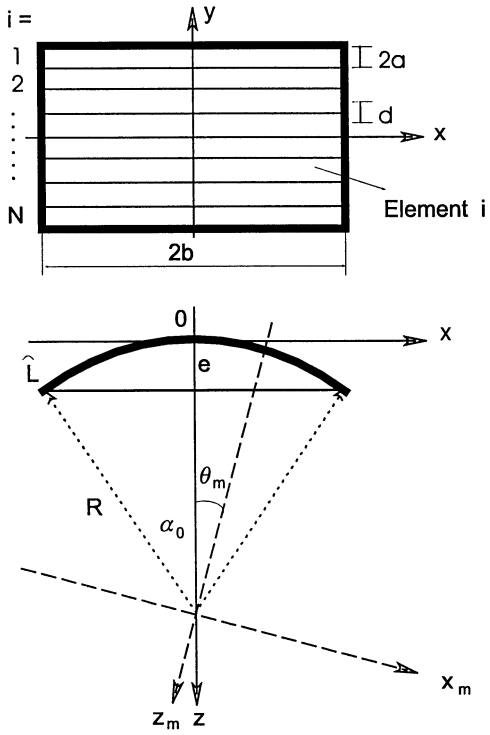

Fig. 2.2. Geometry of the linear array with cylindrically concave surface.

2.2.3 Examples and discussions

To apply the theory proposed in the preceding section, the SIRs of two specific sources in water are considered in this section. The sound velocity of water used in all the calculations is c=1485 m/s. One is the concave, rectangular transducer with 2a=16 mm, 2b=33.5 mm, and R=190 mm. The other is the linear array consisting of 16 elements with 2a=0.9 mm, 2b=33.5 mm, and R=190 mm. The arc length of the cylindrical curve is 33.543 mm. These parameters, actually, define the linear array that is used in our laboratory. In calculating their SIRs, both the aperture and the array are divided into 670 narrow strips (i.e., M = 670) so that each strip is a 16 mmx0.05 mm rectangle. The SIRs of the aperture and the array are calculated using Eqs. (2.13) and (2.14), respectively. Note that in this

section all the following figures relevant to the SIRs show $h(\mathbf{r}, t)/c$ instead of $h(\mathbf{r}, t)$, and the time axes are in different scales for best illustrating the SIRs at different positions.

A. The SIRs of the concave, rectangular aperture with 2a = 16 mm, 2b = 33.5 mm, and R =190 mm.

The SIRs of the concave, rectangular aperture are calculated in four cases, that is, on the z-axis (z= 170 - 240 mm), and across the z-axis at three depths, z = 130, 190 (focal position), and 240 mm. The respective results are shown in Figs. 2.3-2.6. It should be pointed out that the peak at the focal point in Figs 3 and 5 is infinitely high so that it can not be displayed completely. Here the main features of the SIRs of the aperture are examined and analyzed without going into much detail.

(i) In a special case where the field points are on the center axis of the cylindrical curve, i.e., the y-line at $x = 0$ and $z = R$ (refer to Fig. B2.1), the analytic form of $h(\mathbf{r}, t)$ is available and its derivation is given in Appendix 3-B. The analytic form is evaluated in two regions. In the region of $|y| \le a$,

$$h(\mathbf{r},t)=\begin{cases}\dfrac{2cR}{\pi\sqrt{(ct)^2-R^2}}\arcsin\left(\dfrac{b}{R}\right), & R<ct\le R',\\ \dfrac{cR}{\pi\sqrt{(ct)^2-R^2}}\arcsin\left(\dfrac{b}{R}\right), & R'<ct<R'',\\ 0, & \text{otherwise,}\end{cases} \tag{2.15a}$$

and in the region of $|y| > a$,

$$h(\mathbf{r},t)=\begin{cases}\dfrac{cR}{\pi\sqrt{(ct)^2-R^2}}\arcsin\left(\dfrac{b}{R}\right), & R'<ct<R'',\\ 0, & \text{otherwise,}\end{cases} \tag{2.15b}$$

where $R'=\sqrt{R^2+(|y|-a)^2}$ and $R''=\sqrt{R^2+(|y|+a)^2}$.

(ii) For the field points on the z-axis (see Fig. 2.3), $h(\mathbf{r}, t)$ has the non-zero portion starting just from time instant $t = z/c$ before the focal point, but starting earlier than time instant $t = z/c$ after the focal point. The maximum amplitude of $h(\mathbf{r}, t)$ increases with z until the focal point ($z = R$), and decreases with z beyond the focal point. The width of $h(\mathbf{r}, t)$ decreases with z until the focal point ($z = R$). At the focal point, it follows from Eq. (2.15a) that $h(\mathbf{r}, t)$ approaches to infinity for $t \to R / c$ and has a width of (R''-R)/c. This is different from the case of the spherically focusing transducer where $h(\mathbf{r}, t)$ is an impulse response $\delta(t - R / c)$ at the focus [28,29].

(iii) In the case of off-z-axis, the variations of $h(\mathbf{r}, t)$ in the x-and y-direction are quite different. This is best described in Figs. 2.4-2.6 that show the SIRs vary in the x- and y-direction before the focus (z = 130 mm), at the focus (z = 190 mm), and beyond the focus (z = 240 mm). In the x-direction, the non-zero portion of $h(\mathbf{r}, t)$ shifts toward an earlier time instant (toward left in the figures) as $|x|$ is getting bigger from x = 0 till $|x| = b$, and then toward a later time instant (toward right in the figures) for further increasing $|x|$. In the y-direction, the non-zero portion of $h(\mathbf{r}, t)$ always starts at the same time instant from y = 0 till $|y| = a$, and then moves toward a later time instant as $|y|$ further increases. This behavior of $h(\mathbf{r}, t)$ neither resembles the case of the corresponding planar, rectangular transducer [20], nor the case of the spherical transducer [28,29].

(iv) Some features of $h(\mathbf{r}, t)$ in the present case that are similar to those in the case of the corresponding planar, rectangular transducer can be seen from Figs 2.4-2.6. For example, $h(\mathbf{r}, t)$ becomes wider and gets smaller in amplitude as the distance off the axis increases.

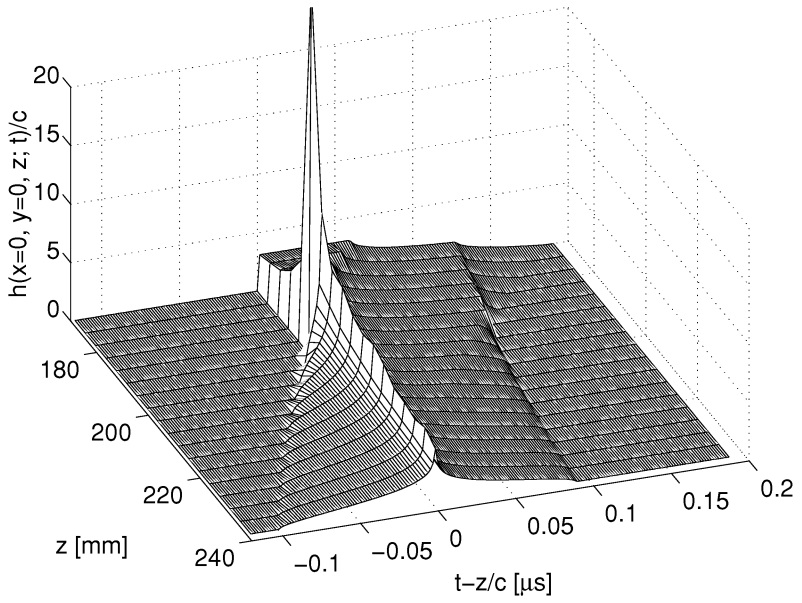

Fig. 2.3. The spatial impulse responses of the concave, rectangular aperture along the z-axis in the range of z=170-240 mm.

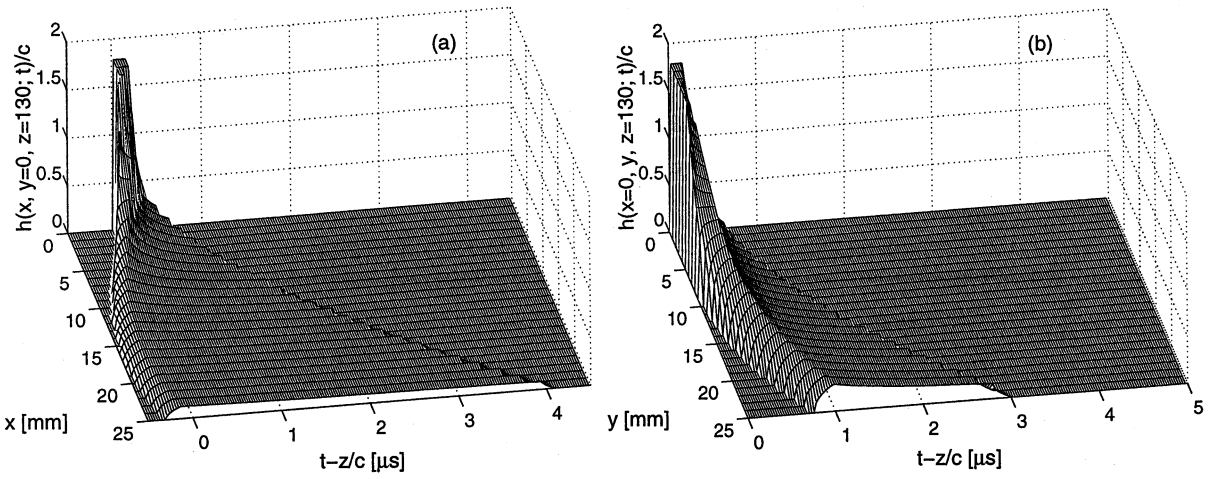

Fig. 2.4. The spatial impulse responses of the concave, rectangular aperture along (a) the x-axis and (b) the y-axis at $z = 130$ mm.

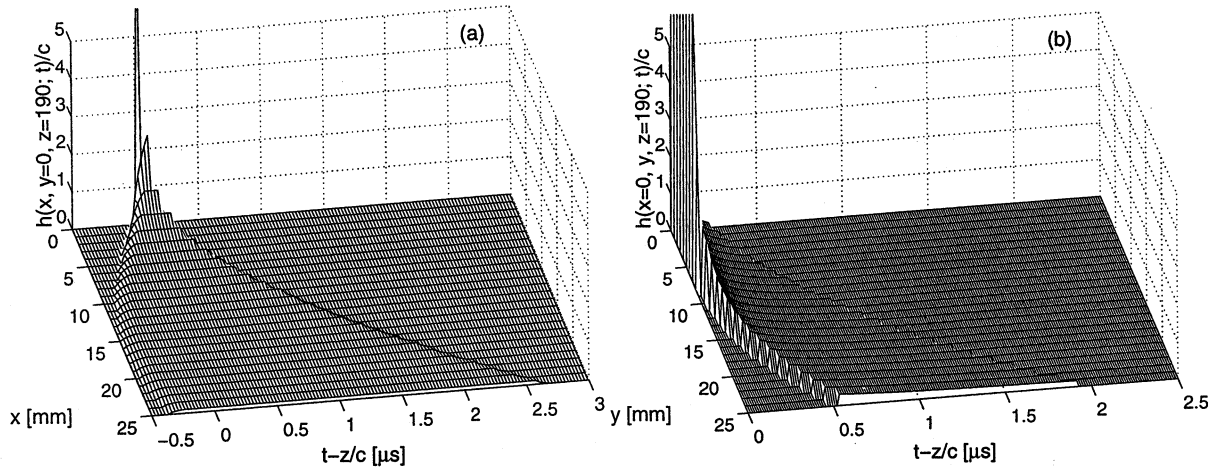

Fig. 2.5. The spatial impulse responses of the concave, rectangular aperture along (a) the x-axis and (b) the y-axis at the focal plane ($z = 190$ mm).

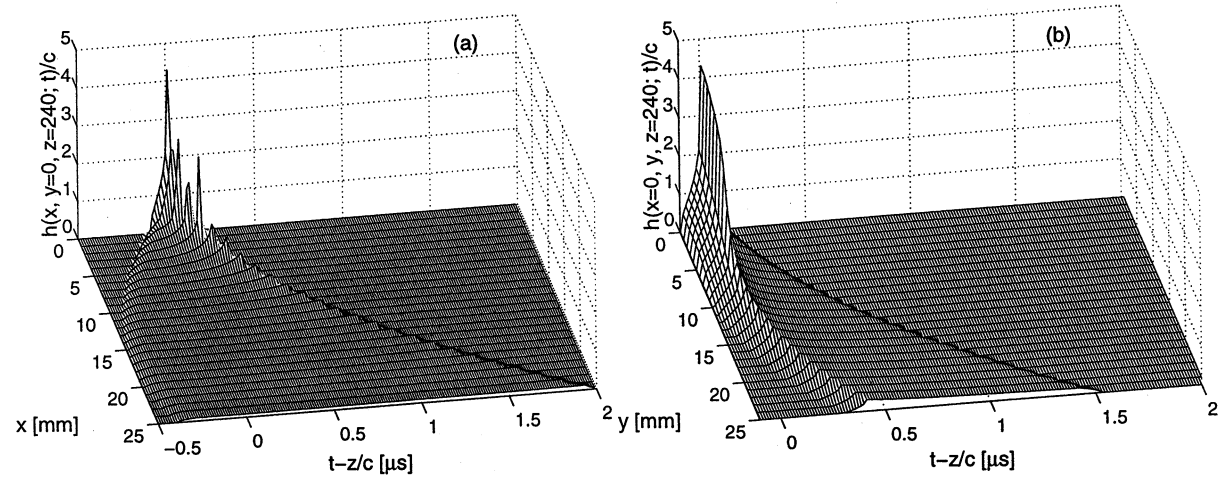

Fig. 2.6. The spatial impulse responses of the concave, rectangular aperture along (a) the x-axis and (b) the y-axis at $z = 240$ mm.

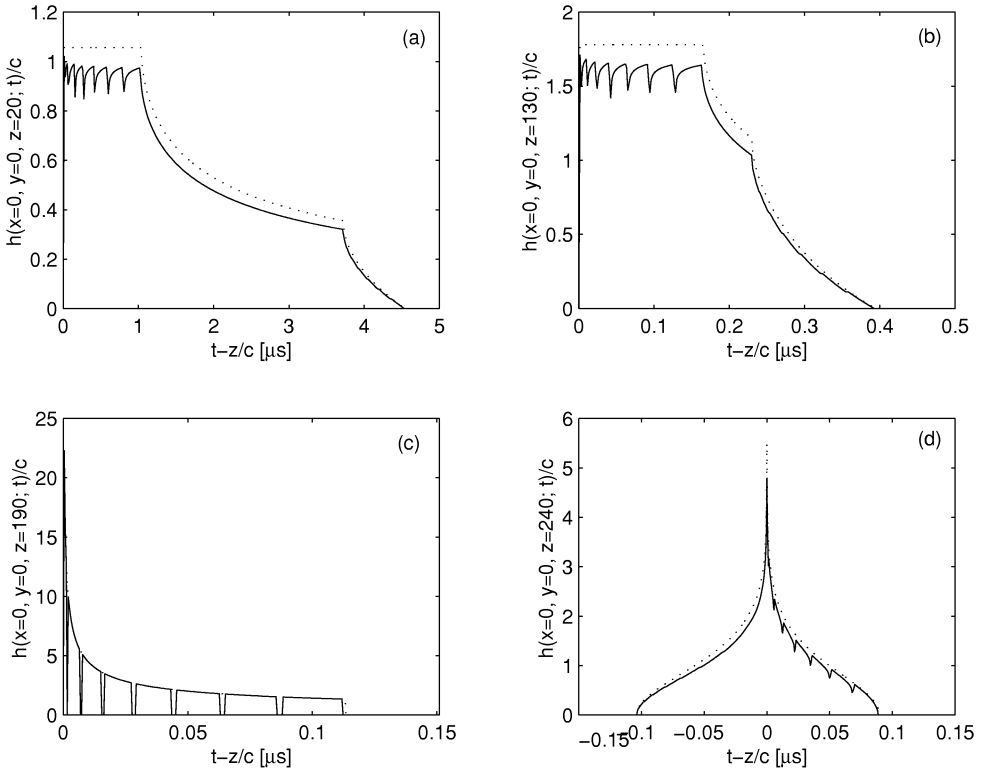

Fig. 2.7. The spatial impulse responses of the linear array (solid) in comparison with those of the corresponding concave, rectangular aperture (dotted) on the axis at (a) z = 20 mm, (b) z = 130 mm, (c) z = 190 mm, and (d) z = 240 mm.

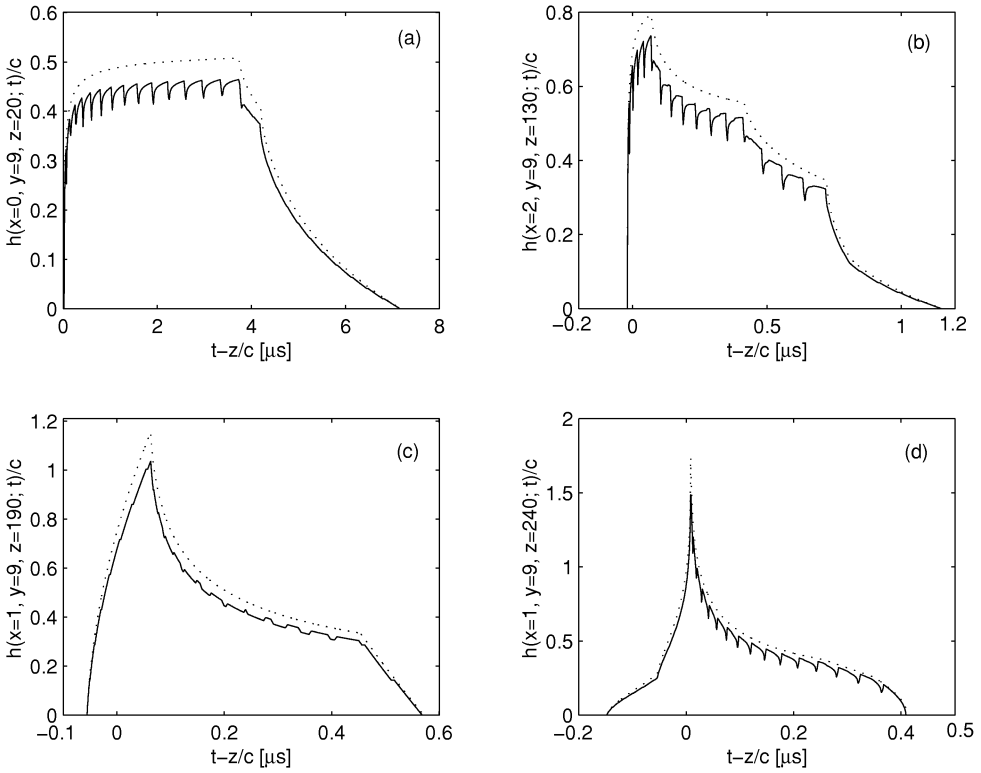

Fig. 2.8. The spatial impulse responses of the linear array (solid) in comparison with those of the corresponding concave, rectangular aperture (dotted) off the axis at (a) (x, y, z) = (0, 9, 20) mm, (b) (x, y, z) = (2, 9, 130) mm, (c) (x, y, z) = (1, 9, 190) mm, and (d) (x, y, z) = (1, 9, 240) mm.

B. The SIRs of the linear array of 16 elements with 2a = 0.9 mm, 2b = 33.5 mm, and R =190 mm.

The SIRs of the linear array without electronic focusing are computed in two cases of on-axis and off-axis. In each case, the SIRs at four different positions are presented in comparison with the corresponding SIRs of the rectangular aperture studied in Sect. III-A. The SIRs on the z-axis at z = 20, 130, 190, and 240 mm are illustrated in Fig. 2.7, and those off the z-axis at **r** = (0, 9, 20), (2, 9, 130), (1, 9, 190), and (1, 9, 240) mm are displayed in Fig. 2.8. From the two figures, it can be seen that the SIRs of the array and the rectangular aperture look similar in general, but differ quite much in details. All the differences result from the existence of the 0.1-mm gaps between adjacent elements. The main features of the SIRs of the array observed are the following:

(i) on the axis, all the SIRs have eight discontinuous parts that come from the superposition of the SIRs of eight pairs of array elements symmetrical to the axis (Fig. 2.7);

(ii) off the axis, all the SIRs are out of the geometrical region (i.e. $|y|>a$) and have 16 discontinuous parts that come from the superposition of the SIRs of 16 elements (Fig. 2.8);

(iii) the SIRs of the array have smaller amplitude than those of the rectangular aperture (Figs. 2.7 and 2.8), except the one at the focus (Fig. 2.7(c)), because the 0.1-mm gaps lessen the radiating surface;

Now let us compare our method presented above with other methods that are the possible solution of our problem. Comparing with the method proposed by Reibold and Kazys [35], our method is both more efficient and more accurate for the same M. For example, for the SIR of each strip, our method only needs to make one straight calculation of the SIR but the Reibold and Kazys's method needs to make four calculations and then sum the four calculated results (see Eq. (10) in [35]). Since in [35] the concave, rectangular transducer was treated as a plane transducer that was subdivided into a set of elementary strips on which the appropriate phase shifts were imposed, it was equivalent to a planar "linear array" that consisted of the same set of such elementary strips and had the imposed time delays corresponding the same phase shifts. Therefore, the impulse response obtained in such a way was not the one of the cylindrically concave, rectangular transducer, but the one of the "linear array", and thus the short spikes appearing in their results were not due to insufficient spatial sampling but had to be like that for the "linear array". This surely results in some significant errors. For example, the radiating surface area of the "linear array" is planar and thus smaller than the actual radiating surface area of the concave transducer, and the orientations of the elementary strips are different and not always parallel to the transducer axis. Because of this treatment, the SIR obtained at the focal point was not infinite in amplitude (see Fig. 7 in [35]) although in fact it has to be. The method developed by Theumann *et al* [24] for a cylindrical transducer possibly can be applied to treating the rectangle transducer with a cylindrical surface. But it requires solving elliptic integrals, and thus it can be less efficient than our method. In comparison with the method suggested by Jensen and Svendsen [25], our method is more accurate and much more efficient, especially for the field points in the near-field

region and in the focal zone under the same condition of dividing the aperture in the x-direction. The reason is the following: the method suggested by Jensen and Svendsen [25] carries out the division of an aperture in two directions, e.g., into MxN small rectangles in the x- and y-directions as defined in Fig. 2.1, so that all sides of each small rectangle divided from the aperture must be small enough to satisfy the far-field approximation; whereas our method makes the division only in one direction, i.e., into M narrow rectangles in the x-direction in Fig. 2.1, so that each strip (a narrow rectangle) divided from the aperture only needs to be narrow enough in the x-direction (see Fig. 2.1). Also the far-field approximation is not needed because each strip's exact SIR is available in analytic form.

2.2.4 Simulations of ultrasonic fields, and comparisons with experiments

In this section, the ultrasonic fields from the ALLIN ultrasonic array system in our laboratory working in the pulse-echo mode have been measured and compared with the simulated results.

The array used in the experiments consists of 64 strip-like elements that are linearly-aligned in the y-direction and cylindrically curved in x-direction with the radius of curvature of 190 mm (refer to Fig. 2.2). In the present case, 16 elements are used to form an aperture. The spacing between the centers of the adjacent elements is 1 mm, and the gap between the adjacent elements is 0.1 mm. This means that the width of each element is $2a$=0.9 mm. The length of each element is $2b$ = 33.5 mm. The nominal center frequency is 3 MHz, and the band width 58%. All the simulated results are based on this geometry.

To simulate an ultrasonic field from a transducer, as mentioned in Sect. II-A, one needs to know the SIR of the transducer and the pulse excitation of normal velocity on the transducer surface. The SIR can be determined using the approach developed in Sect. II. The SIR of the linear array has been obtained and presented in Sect. III-C. The pulse excitation can be determined by experiment in combination with a deconvolution technique, presented below in Sect. IV-A. Based on the SIR and the pulse excitation, and using Eqs. (2.4c) and (2.5), the pulse-echo fields are simulated.

Measurements of the pulse-echo fields from the ALLIN array system were performed by using a small scatterer, a carbide drill that was a flat-end cylinder with a 0.3-mm diameter and a 20-mm length. The drill was fixed to a hard rubber plate with a 17-mm length outside the plate. Both the array and the scatterer were put in a water tank. The array was scanned mechanically in the x- and z-directions and electronically in the y-direction while the scatterer was placed at a fixed position. The sound velocity of water measured and used in all the calculations was 1485 m/s, and the density was 1000 $\mathrm{kg/m^3}$. The sampling frequency used in the measurements was 66.7 MHz, and the amplitude resolution was 8 bits.

In theory a rigid point-like scatterer is needed so that Eq. (2.5) holds. Using the above-mentioned small scatterer will result in some small deviation from the prediction by Eq. (2.5), but not a significant deviation so that the predicted results are in good agreement with the measured ones. This will be shown in the following subsections discussing comparison of the simulations and measurements. To reduce the electronic noise, all the measured results were post-processed by an ideal low pass filter with 6.45-MHz cutoff frequency. But it should be noted that the noise in the effective frequency range (0-6.45 MHz) could not be eliminated and thus still has some small effect on the measured echoes. All the simulated and measured results shown in the following figures are normalized.

A. Determination of the pulse excitation of normal velocity on the linear array from experiments

The pulse excitation of normal velocity, $v_n(t)$, is obtained by performing a deconvolution of Eq. (2.5) using the simplified Wiener filter,

$$v_n(t) = \text{IFFT}\left[V_n(\omega)\right] = \frac{1}{e_0}\,\text{IFFT}\left[\frac{H_{fb}^*(\mathbf{r},\omega)}{\left|H_{fb}(\mathbf{r},\omega)\right|^2 + q}E(\omega)\right], \tag{2.16}$$

where IFFT[.] means the inverse fast Fourier transform, $E(\omega)$ is the Fourier transform of the measured pulse-echo $e(t)$, and $H_{fb}(\mathbf{r},\omega)$ is the Fourier transform of the transmission/reception pressure spatial impulse response of the array, i.e., $H_{fb}(\mathbf{r},\omega) = \text{FFT}\left[h_p(\mathbf{r},t) * h_p(\mathbf{r},t)\right]$, and $H_{fb}^*(\mathbf{r},\omega)$ is the conjugate of $H_{fb}(\mathbf{r},\omega)$. q in the equation is a constant defining the inverse of the signal-to-noise ratio (SNR), and it was chosen to be $q = 0.0001\max\left[\left|H_{fb}(\mathbf{r},\omega)\right|^2\right]$ based on the echo from the field point on the axis at z = 180 mm, which is close to the focal point and has large SNR (see Fig. 2.9(c), and SNR in Table 2.1). Using the echo from this on-axis field point and the SIR of the 16-elemenet array at the field point (Fig. 2.9(a)) in Eq. (2.16), the pulse excitation was obtained (Fig. 2.9(d)).

B. Simulation of pulse-echo fields and comparison with the experiments

From Eq. (2.5) and using the pulse excitation shown in Fig. 2.9(d), the pulse-echo fields from the 16-element linear array are simulated on the axis (Fig. 2.10) and off the axis (Fig. 2.11), and compared with the measurements. In Figs. 2.10 and 2.11, the simulated results are plotted in solid curves, and the measured in dotted curves. Fig. 2.10 shows the echoes from on-axis points at z = 20, 130, 180, 240 mm, and Fig. 2.11 illustrates those from off-axis points at (x, y, z) = (0, 9, 20), (2, 9,

130), (1, 9, 180), and (1, 9, 240) mm. The signal-to-noise ratios (SNR), the ratio of signal power to noise power, of the measured signals and the normalized root-mean-square (rms) differences between the simulated and the measured results are given in Table 2.1. The rms difference is here defined as $\Delta_{\text{rms}} = \left\{ \sum_{m=1}^{M} \left[V_{\text{simu}}(m) - V_{\text{meas}}(m) \right]^2 \Big/ \sum_{m=1}^{M} \left[V_{\text{meas}}(m) \right]^2 \right\}^{1/2}$ where $V_{\text{simu}}(m)$ and $V_{\text{meas}}(m)$ are the simulated and measured results after normalization. Note that the SNRs for Figs. 2.10(a) and 2.11(a) were estimated with the resolvable edge waves excluded, and Δ_{rms}'s were evaluated in the effective ranges of the main echoes to minimize the noise effect. The noise included electronic noise from the ALLIN system and quantization error noise of the A/D since the amplitude resolution used was 8 bits. The effect of the quantization error noise was very significant when the signal level was low. Although the noise was largely reduced by using the above mentioned post-processing, the noise in the frequency range (i.e., 0-6.45 MHz) of effective signals could not be filtered out and still had significant effects on the measured data with low SNRs, e.g., in the case of Fig. 2.11.

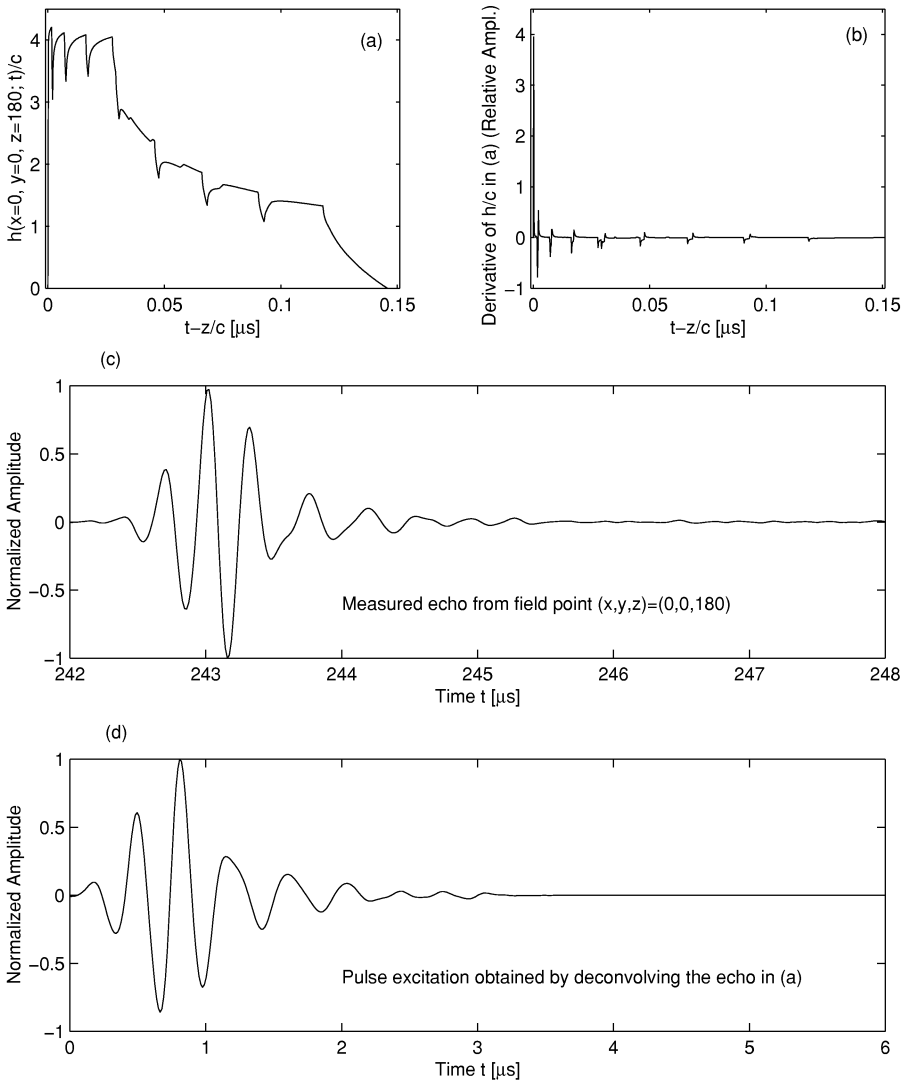

Fig. 2.9. (a) The SIR, $h(\mathbf{r}, t)$, of the array, and (b) the derivative of $h(\mathbf{r}, t)$ at field point $\mathbf{r}$ = (0, 0, 180). (c) The measured echo from field point $\mathbf{r}$ = (0, 0, 180). (d) The pulse excitation of normal velocity on the array surface obtained by deconvolving the echo in (c) with the SIR at the field point using Eq. (2-16).

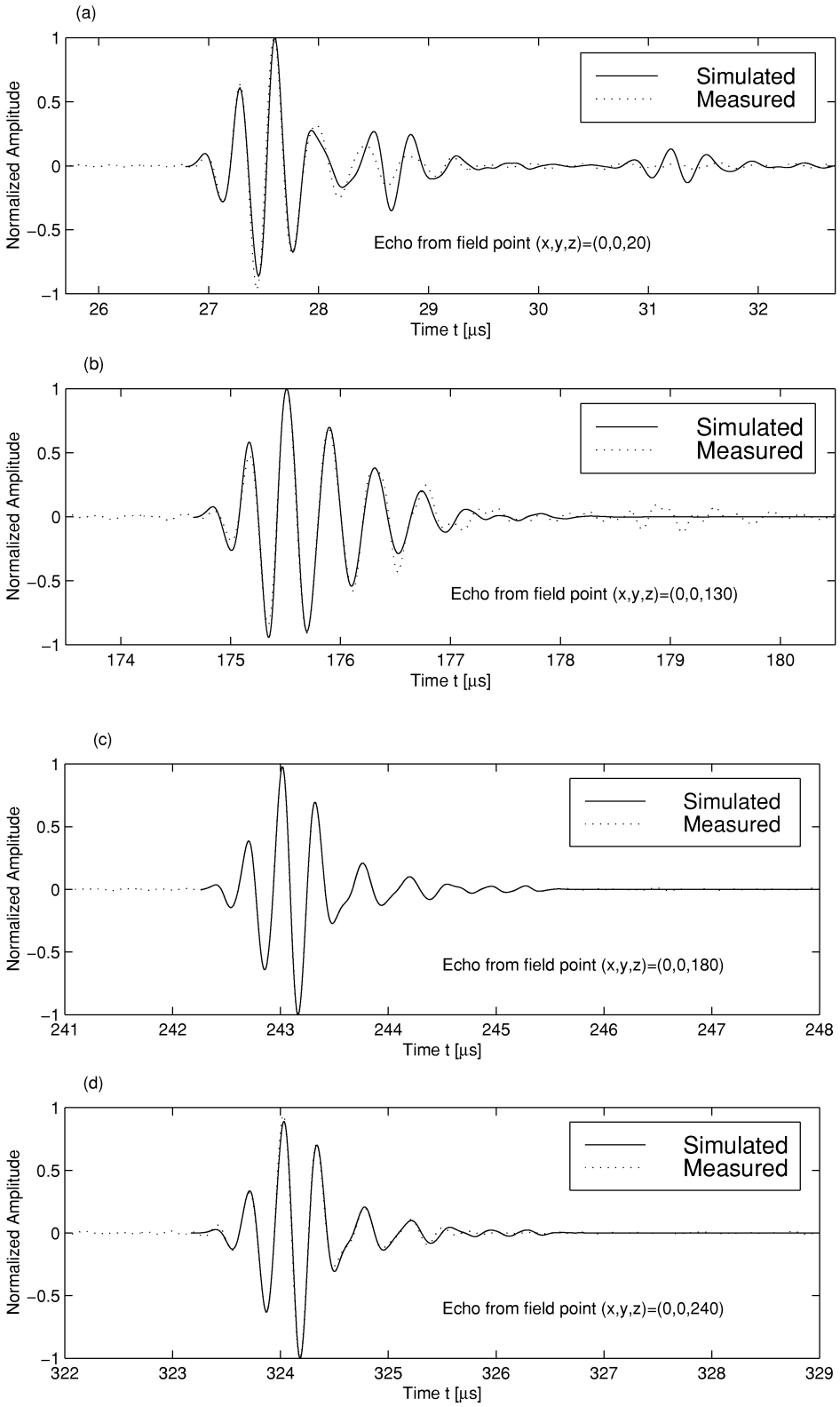

Fig. 2.10. The measured (dashed) and simulated (solid) pulse-echoes from the linear array on the axis at (a) z = 20 mm, (b) z = 130 mm, (c) z = 180 mm, and (d) z = 240 mm.

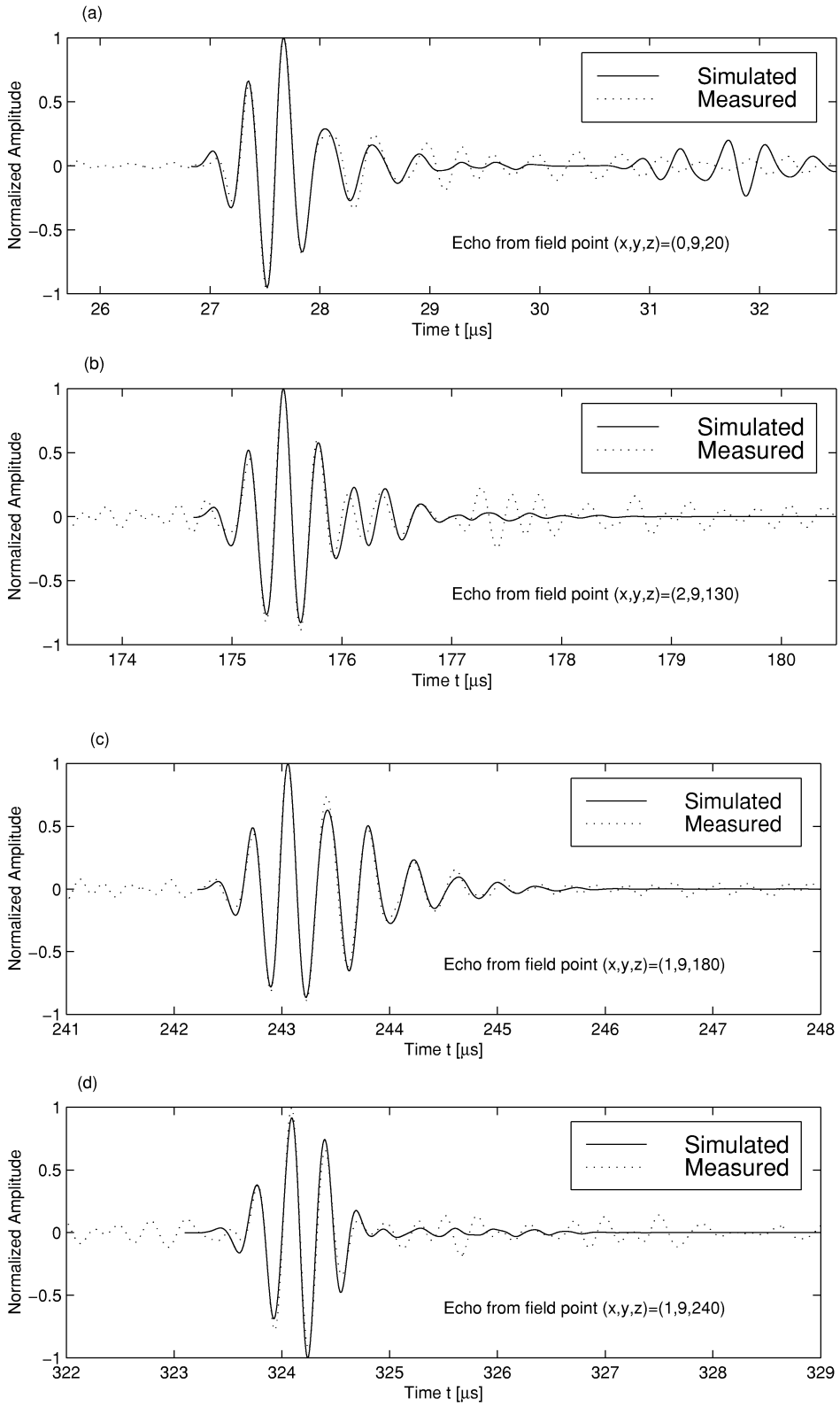

Fig. 2.11. The measured (dashed) and simulated (solid) pulse-echoes of the linear array off the axis at (a) (*x, y, z*) = (0, 9, 20) mm, (b) (*x, y, z*) = (2, 9, 130) mm, (c) (*x, y, z*) = (1, 9, 180) mm, and (d) (*x, y, z*) = (1, 9, 240) mm.

TABLE 2.1. The signal-to-noise ratio (SNR) of the measured echoes and the normalized rms difference (Δ_{rms}) of the simulated and measured results in Figs. 2.10 and 2.11. Note that the SNRs in Figs. 2.10(a) and 2.11(a) were estimated with the resolvable edge waves excluded, and Δ_{rms}'s were evaluated in the effective ranges of the main echo waves.

	Fig. 2.10				Fig. 2.11			
	(a)	(b)	(c)	(d)	(a)	(b)	(c)	(d)
SNR	14.68	87.98	647.16	246.00	2.21	6.10	19.38	5.77
Δ_{rms}	0.260	0.168	0.005	0.094	0.249	0.234	0.181	0.255

From Table 2.1 and the comparisons shown in Figs. 2.10 and 2.11, it is seen that the simulated results are, on the whole, in a very good agreement with the measured ones. Looking into some detail, we can find that for the high SNR (Figs. 2.10(c)-(d)) the agreement becomes excellent, and for the lower SNR (Figs. 2.10(a)-(b) and 2.11(a)-(d)), the agreement is still good. This also indicates that the agreement between the simulated and measured results can be better if the SNR can be improved. The resolvable edge waves in the measured results in Figs. 2.10(a) and 2.11(a) can not be seen. This is because the edge waves are small in the case of a rectangular aperture and thus difficult to detect. A similar case was also reported in the paper by Hayman and Weight [42]. In addition to the noise effect, use of a finite-sized small scatterer of 0.3 mm diameter may result in some small deviation of the predicted results from the measured ones. Evaluation of such deviation is not of our present interest. The discrepancies may also be attributed to the using of the nominal, instead of effective, geometrical parameters of the array like in the case of spherically focused transducers [47]. This is another topic that will be further investigated in our future work. Basically, the above comparison and analysis have demonstrated that the approach developed in the present work for computing the SIR of the linear array with a cylindrically curved surface can provide a very good prediction of the pulse-echo fields from the array.

2.3 Elastic fields radiated by the ALLIN array into immersed copper canisters

Ultrasonic elastic fields radiated by the ALLIN array in an immersed copper canister have been calculated based on the angular spectrum approach (ASA). The ASA applied to the calculation of elastic fields in immersed solids has been presented in our previous reports and papers [1-7]. Although the ASA was only used to the case of planar arrays and transducers, it can also apply to curved arrays provided that the angular spectra of the curved arrays are used. Recently, we have developed a method to calculate the angular spectrum of the ALLIN array with a cylindrically curved surface and presented in Refs. [8,9]. Based on the above mentioned theory and the method and using

the pulse excitation of the array obtained in the preceding section (Fig. 2.9(d)), the elastic fields radiated by the ALLIN array in a copper canister submerged in water have been computed in terms of particle velocity. The immersing fluid is water whose sound velocity is 1485 m/s and density is 1000 kg/m^3. The copper canister is assumed to be an isotropic and non-attenuating medium that has LW and SW velocities of 4596 m/s and 2260 m/s, respectively, and density of 8960 kg/m^3. The path length of the water layer was 28 mm. Two different apertures have been used that consist of 16- and 32-elements, respectively. To each of the apertures four different focusing laws are applied that focus the normally incident beams in the immersed canister at distances of 20, 40, 60, and 80 mm beneath the front surface of the copper, respectively. All these focusing laws are those that in our last report [8] we applied to the ALLIN array to generate the focused pulse-echo fields. All these focused fields were measured on a copper block with a set of side-drilled holes located at different depths and presented in our last report [8] in order to test and confirm the focusing laws and finally to find out a one that was most suited for the inspection of EB welds in copper canisters.

The calculated elastic fields from the 16- and 32-element apertures are shown in Figs. 2.12 and 2.13, respectively. Each field is displayed both in color-scaled levels and contour. Comparing these transmit fields in Figs. 2.12 and 2.13 with the corresponding pulse-echo fields that we measured in last year (see [8]), we can easily see the correlation between them. For example, their beam patterns or spatial resolutions look very similar.

Let us look at the field in Fig. 2.13(d) that is focused at z=80 mm by the 32-element aperture. This focused field is what we used for evaluation of EB welds. The reason for choosing this focused field was that it has a narrow beam width over the depth range from 50 to 70 mm, the range of EB welds.

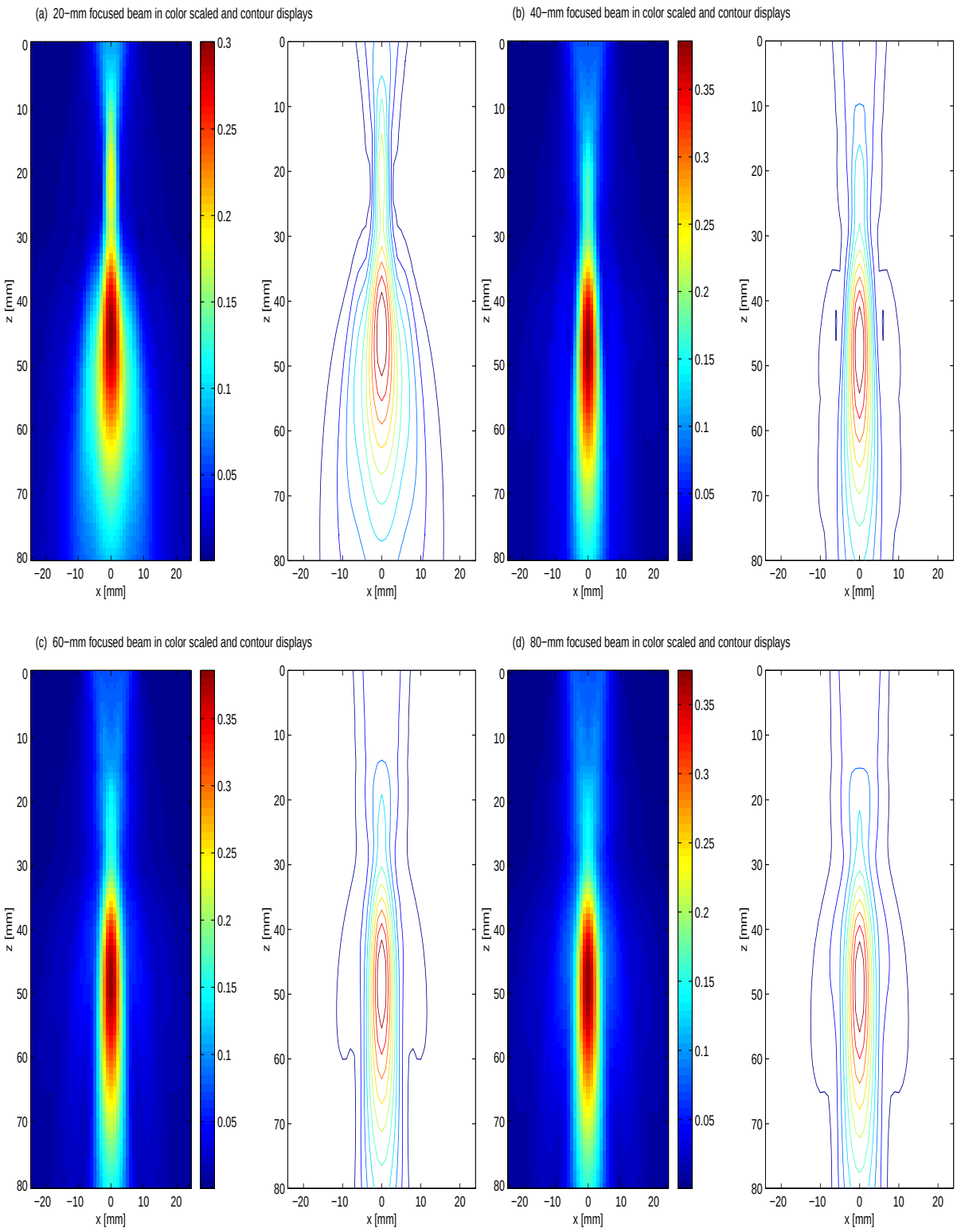

Fig. 2.12. Calculations of elastic fields radiated by the 16-element aperture into the immersed copper with four focusing laws that focus the normally incident beams at (a) 20, (b) 40, (c) 60 and (d) 80 mm, in the copper. The fields are shown in terms of particle velocity.

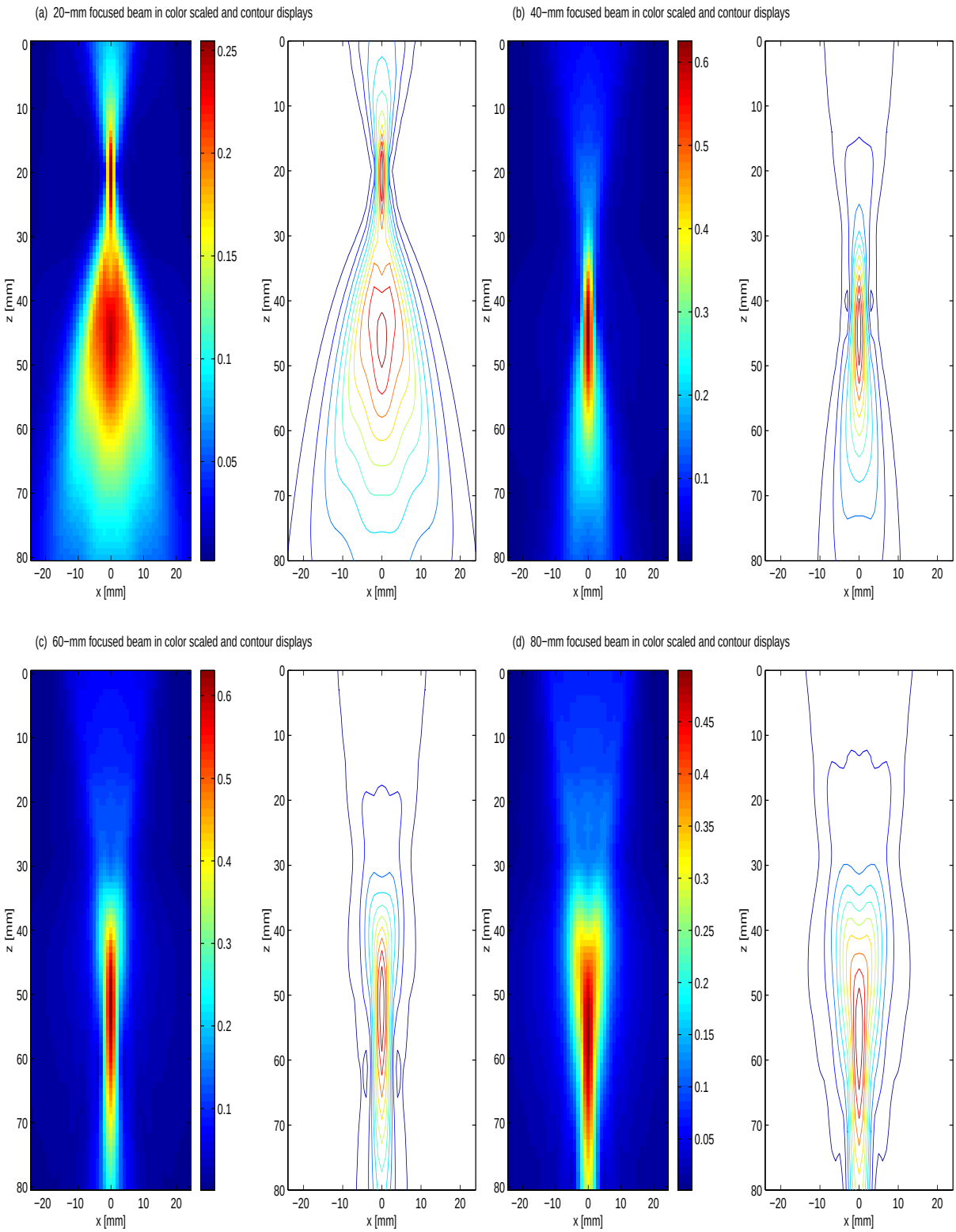

Fig. 2.13. Calculations of elastic fields radiated by the 32-element aperture into the immersed copper with four focusing laws that focus the normally incident beams at (a) 20, (b) 40, (c) 60 and (d) 80 mm, in the copper. The fields are in terms of particle velocity.

2.4 Conclusion

An approach to computing the SIR of a cylindrically curved, rectangular aperture has been developed. It calculates the SIR by superposing the SIRs of a row of very narrow strips into which the aperture is divided in the cylindrically curved direction. The strips are so narrow that they can be considered to be planar, rectangular apertures whose exact SIRs are available in analytic form. For the field points on the center axis of the cylindrical curve, the analytic form of the SIR of such a cylindrically curved, rectangular aperture has been found. Using this approach, the SIR of a linear array used in our laboratory which consists of rectangular elements with such cylindrically curved surfaces has been obtained. Analysis and comparison of the SIRs of both the curved, rectangular aperture and the array have been made in some detail. The pulse excitation of normal velocity on the surface of the array, another condition required for simulating actual ultrasonic fields, has been determined by measurement in combination with a deconvolution technique. Using the SIR and the pulse excitation obtained, the pulsed-echo fields from the array have been simulated. Measurements of the pulse-echo fields were performed using a small scatterer (a 0.3-mm-diameter flat-ended carbide drill). The simulated results have been compared with the measured ones, and the comparison has shown that the simulated and the measured results are very similar. This has basically validated the developed approach.

There were some small discrepancies between the simulated and the measured results, especially when the measured results had low signal-to-noise ratios. These discrepancies were caused mostly by the electronic noise and the quantization error of A/D converters, and slightly by using a finite-sized, small scatterer. Use of the nominal geometrical parameters of the array also contributed to the discrepancies. The effect of the nominal geometrical parameters on the theoretical prediction, and the effective geometrical parameters of the transducers and arrays need further investigating.

For calculating the SIR of a rectangular transducer or a linear array with a cylindrically curved surface, the approach proposed in this report is more efficient than the method in [34], and both more accurate and more efficient than the methods presented in [25] and [35].

Having used the pulse excitation of the ALLIN array obtained in Sect. 2.3, elastic fields in an immersed copper canister radiated by two apertures consisting of 16- and 32-elements have been calculated in eight cases. To each of the apertures four focusing laws have been applied that focus the normally incident beams in the immersed canister at distances of 20, 40, 60, and 80 mm beneath the front surface of the copper, respectively. These fields have shown to have good correlation (e.g., the variations of beam widths or lateral resolutions with depth) with the measured pulse-echo fields from a side-drilled-holes copper block that were presented in our last report [8].

APPENDIX 3-A: SPATIAL IMPULSE RESPONSE OF A PLANAR, RECTANGULAR APERUTRE WITH SIZE $2\bar{a}\times 2\bar{b}$ *[20]*

TABLE A-I. $(2\pi/c)h_{\text{rect}}(\mathbf{r},t)$ - the spatial impulse response (SIR) of a planar, rectangular aperture with size $2\bar{a}\times 2\bar{b}$ ($\bar{a}\le\bar{b}$) [20].

Time interval	Region I	Region II	Region III	Region IV
$\tau_{\min} < t < \tau_A$	. . .	$\pi - 2\alpha_2$	$2\bar{\alpha}_3 - 2\alpha_1$	$-2\pi - 2\bar{\alpha}_1 - 2\bar{\alpha}_2 + 2\bar{\alpha}_3 + 2\bar{\alpha}_4$
$\tau_A < t < \tau_m$	$\pi/2 - \alpha_1 - \alpha_2$	$\pi/2 - \alpha_1 - \alpha_2$	$-\pi/2 - \alpha_1 - \alpha_2 + 2\bar{\alpha}_3$	$-3\pi/2 - \alpha_1 - \alpha_2 + 2\bar{\alpha}_3 + 2\bar{\alpha}_4$
$\tau_m < t < \tau_M$ *	$-\alpha_1 + \alpha_3$	$-\pi - \alpha_1 + \alpha_3 + 2\bar{\alpha}_4$	$-\alpha_1 + \alpha_3$	$-\pi - \alpha_1 + \alpha_3 + 2\bar{\alpha}_4$
$\tau_m < t < \tau_M$ **	$-\alpha_2 + \alpha_4$	. . .	$-\pi - \alpha_2 + 2\bar{\alpha}_3 + \alpha_4$	$-\pi - \alpha_2 + 2\bar{\alpha}_3 + \alpha_4$
$\tau_M < t < \tau_D$	$-\pi/2 + \alpha_3 + \alpha_4$	$-\pi/2 + \alpha_3 + \alpha_4$	$-\pi/2 + \alpha_3 + \alpha_4$	$-\pi/2 + \alpha_3 + \alpha_4$

* for $\tau_B \le \tau_C$, and ** for $\tau_C \le \tau_B$.

$\tau_m = \min(\tau_B, \tau_C)$, $\tau_M = \max(\tau_B, \tau_C)$, $\tau_{\min} = \tau_A$, τ_{S2}, τ_{S1}, or τ_0 for regions I, II, III, and IV (refer to Fig. 2.1), respectively, where $\tau_0 = z/c$, $\tau_{Si} = \left[d_i^2 + z^2\right]^{1/2}/c$, $d_1 = x - \bar{a}$, $d_2 = y - \bar{b}$, $d_3 = x + \bar{a}$, and $d_4 = y + \bar{b}$. $\alpha_i(\mathbf{r},t) = \arcsin\left[d_i/\sigma(\mathbf{r},t)\right]$, and $\bar{\alpha}_i(\mathbf{r},t) = \text{sgn}(d_i)\arcsin\left\{\left[|d_i|/\sigma(\mathbf{r},t)\right], 1\right\}$, where $\sigma(\mathbf{r},t) = (c^2t^2 - z^2)$, and $\text{sgn}(d_i)$ stands for the sign of d_i.

APPENDIX 3-B: THE ANALYTIC FORM OF THE SIR OF A CONCAVE, RECTANGULAR APERTURE FOR THE FIELD POINTS ON THE y-LINE AT x = 0 AND z = R

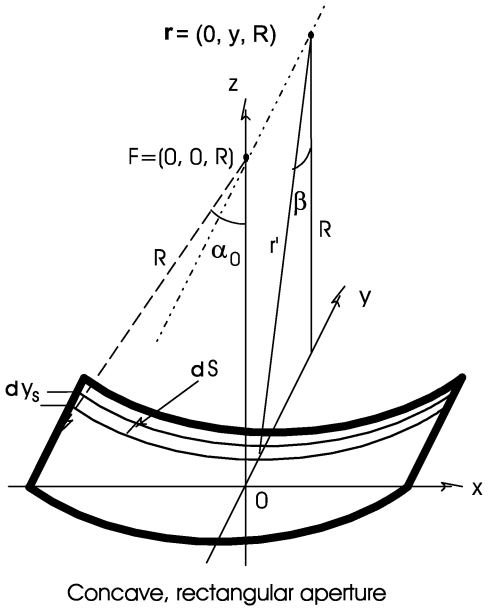

Fig. B2.1. Schematic for derivation of the analytic SIR of the concave, rectangular aperture on field points **r** = (0, *y*, *R*).

For a concave, rectangular aperture with a $2a \times 2b$ dimension and radius of curvature, R, (as shown in Fig. 2.1), its SIR is available in analytic form in the case where the field points are on the center axis of the cylindrical curve, i.e., on the y-line at $x = 0$ and $z = R$ that is expressed by $\mathbf{r} = (0, y, R)$.

From the geometry for this special case shown in Fig. B2.1, one has

$$dS = 2\alpha_0 R dy_s = 2\alpha_0 R\, dr' / \sin\beta = 2\alpha_0 R\, r'\, dr' \Big/ \sqrt{r'^2 - R^2}\ , \tag{B2.1}$$

where α_0 is determined by Eq. (2.6). The SIR $h(\mathbf{r}, t)$ is evaluated in two regions. In the region of $|y| \le a$, one has from Eq. (2.3) and Eq. (B2.1),

$$\begin{aligned} h(\mathbf{r},t) &= \int_{-a}^{a} \frac{\delta(t - r'/c)}{2\pi r'} 2\alpha_0 R dy_s \\ &= \frac{\alpha_0 R}{\pi} \int_{R}^{\sqrt{R^2+(y+a)^2}} \frac{\delta(t - r'/c) dr'}{\sqrt{r'^2 - R^2}} + \frac{\alpha_0 R}{\pi} \int_{R}^{\sqrt{R^2+(y-a)^2}} \frac{\delta(t - r'/c) dr'}{\sqrt{r'^2 - R^2}}\ . \end{aligned} \tag{B2.2a}$$

Letting $R' = \sqrt{R^2 + (|y| - a)^2}$, $R'' = \sqrt{R^2 + (|y| + a)^2}$ and $r' = c\tau$, Eq. (B-2a) reduces to

$$\begin{aligned} h(\mathbf{r},t) &= \frac{2c\alpha_0 R}{\pi} \int_{R/c}^{R'/c} \frac{\delta(t-\tau) d\tau'}{\sqrt{(c\tau)^2 - R^2}} + \frac{c\alpha_0 R}{\pi} \int_{R'/c}^{R''/c} \frac{\delta(t-\tau) d\tau'}{\sqrt{(c\tau)^2 - R^2}}\ , \\ &= \begin{cases} \dfrac{2cR}{\pi\sqrt{(ct)^2 - R^2}} \arcsin\left(\dfrac{b}{R}\right), & R < ct \le R', \\ \dfrac{cR}{\pi\sqrt{(ct)^2 - R^2}} \arcsin\left(\dfrac{b}{R}\right), & R' < ct < R'', \\ 0, & \text{otherwise.} \end{cases} \end{aligned} \tag{B2.2b}$$

Similarly, in the region of $|y| > a$, one has

$$\begin{aligned} h(\mathbf{r},t) &= \int_{-a}^{a} \frac{\delta(t - r'/c)}{2\pi r'} 2\alpha_0 R dy \\ &= \int_{R'}^{R''} \frac{\delta(t - r'/c)}{2\pi r'} \frac{2\alpha_0 R dr'}{\sin\beta} \\ &= \frac{c\alpha_0 R}{\pi} \int_{R'/c}^{R''/c} \frac{\delta(t-\tau) d\tau'}{\sqrt{(c\tau)^2 - R^2}} \end{aligned}$$

$$= \begin{cases} \dfrac{cR}{\pi\sqrt{(ct)^2 - R^2}} \arcsin\left(\dfrac{b}{R}\right), & R' < ct < R'', \\ 0, & \text{otherwise.} \end{cases} \tag{B2.3}$$

The same results are also possible to obtain using a different formulation made by Theumann *et al* (Eq. (12) in [34]) for a concave cylindrical transducer. Since a concave cylindrical transducer can be seen as the sum of two semi-cylindrical transducers that have $b = R$, its SIR can be easily obtained from Eqs. (B2.2b) and (B2.3) as follows,

$$h(\mathbf{r}, t) = \begin{cases} \dfrac{2cR}{\sqrt{(ct)^2 - R^2}}, & R < ct \le R', \\ \dfrac{cR}{\sqrt{(ct)^2 - R^2}}, & R' < ct < R'', \\ 0, & \text{otherwise.} \end{cases} \tag{B2.4}$$

for $|y| \le a$, and

$$h(\mathbf{r}, t) = \begin{cases} \dfrac{cR}{\pi\sqrt{(ct)^2 - R^2}} \arcsin\left(\dfrac{b}{R}\right), & R' < ct < R'', \\ 0, & \text{otherwise.} \end{cases} \tag{B2.5}$$

for $|y| > a$. The result in Eq. (B2.4) is different from the corresponding one in [34], i.e., Eq. (14) in [34]. It seemed that there were some mistakes made in Eq. (14) in [34], that is, only one of the two parts of the SIR (the part in the h^- space, so defined in [34]) was considered.

2.5 References

[1] P. Wu, R. Kazys and T. Stepinski, "Calculation of transient fields in immersed solids radiated by linear focusing arrays," in 1995 *IEEE Ultrason. Symp. Proc.*, pp. 993-997, 1995.

[2] T. Stepinski, and P. Wu, *Ultrasonic Inspection of Nuclear Copper Canisters*, SKB Projektrapport 97-01, December 1996.

[3] P. Wu, R. Kazys and T. Stepinski, "Analysis of the numerically implemented angular spectrum approach based on the evaluation of two-dimensional acoustic fields--Part I: Errors due to the discrete Fourier transform and discretization," *J. Acoust. Soc. Am.* **99:** 1339-1348 (1996).

[4] P. Wu, R. Kazys and T. Stepinski, "Analysis of the numerically implemented angular spectrum approach based on the evaluation of two-dimensional acoustic fields--Part II: Characteristics as a function of angular range," *J. Acoust. Soc. Am.* **99:** 1349-1359 (1996).

[5] P. Wu, R. Kazys and T. Stepinski, "Optimal selection of parameters for the angular pectrum approach to numerically evaluate acoustic fields," *J. Acoust. Soc. Am.* **101**: 125-134, (1997).

[6] T. Stepinski, and P. Wu, *Ultrasonic Inspection of Nuclear Copper Canisters*, SKB Projektrapport 97-08, August 1997.

[7] P. Wu, and T. Stepinski, "Elastic fields in immersed isotropic solids from phased array: the time harmonic case," *Res. Nondestr. Evla.* **10**: 185-204, (1998).

[8] P. Wu, and T. Stepinski, *Inspection of Copper Canisters for Spent Nuclear Fuel by Means of Ultrasonic Array System - Modelling, Defect Detection and Grain Noise Estimation*, SKB Projektrapport, Augusti 1998.

[9] P. Wu, and T. Stepinski, "Extension of the angular spectrum approach to curved radiators," *J. Acoust. Soc. Am.* **105**: 2618-2627, (1999).

[10] P. Wu, and T. Stepinski, " Spatial impulse response method for predicting pulse-echo fields from a linear array with cylindrically concave surface," *IEEE Ultrason. Ferroelec. Freq. Contr.*, accepted for publication in May 1999.

[11] G.R. Harris, "Review of transient field theory for a baffled planar piston," *J. Acoust. Soc. Am.*, vol. 70, pp. 10-20, 1981.

[12] G.E. Tupholme, "Generation of acoustic pulses by baffled plane pistons," *Mathematika,* vol. 16, pp. 209-224, 1969.

[13] P.R. Stepanishen, "The time-dependent force and radiation impedance on a piston in a rigid infinite planar baffle," *J Acoust. Soc. Am.,* vol. 49, pp. 841-849, 1971.

[14] P.R. Stepanishen, "Transient radiation from pistons in an infinite planar baffle," *J Acoust. Soc. Am.,* vol. 49, pp. 1629-1638, 1971.

[15] P.R. Stepanishen, "Acoustic transients from planar axisymmetric vibrators using the impulse-response approach," *J. Acoust. Soc. Am.*, vol. 70, pp. 1176-1181, 1981.

[16] M.A. Fink, and J.-F. Cardoso, "Diffraction effects in pulse-echo measurement," *IEEE Trans. Sonics &Ultrason.*, vol. SU-31, pp. 313-329, 1984.

[17] M.E. Banna, and M.E. Nokali, "On the transient response of a circular transducer," *Wave Motion*, vol. 8, pp. 235-241, 1986.

[18] J.C. Lockwood, and J.G. Willette, "High speed method for computing the exact solution for the pressure variations in the nearfield of a baffled piston," *J Acoust. Soc. Am.,* vol. 53, pp. 735-741, 1973.

[19] J.G. Scarano, N. Denisenko, M. Matteucci, and M. Pappalardo, "A new approach to the derivation of the impulse response of a rectangular piston," *J. Acoust. Soc. Am.*, vol. 78, pp. 1109-113, 1985.

[20] J.L. San Emeterio, and L.G. Ullate, "Diffraction impulse response of rectangular transducers," *J. Acoust. Soc. Am.*, vol. 92, pp.651-662, 1992.

[21] T-J. Teo, "An improved approximation for the spatial impulse response of a rectangular transducer," *IEEE Trans. Ultrason. Ferroelect. Freq. Contr.*, vol. 45, pp. 76-83, 1998.

[22] J.A. Jensen, "Ultrasound field from triangular apertures," *J. Acoust. Soc. Am.*, vol. 100, pp. 2049-2056, 1996.

[23] D. Reilly, and G. Hayward, "A model to predict the transient radiation from segmented annular apertures radiating into solid media," *IEEE Trans. Ultrason. Ferroelect. Freq. Contr.*, vol. 43, pp. 263-269, 1996.

[24] B. Piwakowski, and B. Delannoy, "Method for computing spatial pulse response: Time-domain approach," *J. Acoust. Soc. Am.*, vol. 86, pp. 2422-2432, 1989.

[25] J.A. Jensen, and N.B. Svendsen, "Calculation of pressure fields from arbitraily shaped, apodized, and excited ultrasound transducers," *IEEE Trans. Ultrason. Ferroelect. Freq. Contr.*, vol. 39, pp. 262-267, 1992.

[26] G.R. Harris, "Transient field of a baffled planar piston having an arbitrary vibration amplitude distribution," *J. Acoust. Soc. Am.*, vol. 70, pp. 186-204, 1981.

[27] J. Naze Tjotta and S. Tjotta, "Nearfield and farfield of pulsed acoustic radiators," *J. Acoust. Soc. Am.*, vol. 71, pp.824-834, 1982.

[28] A. Penttinen and M. Luukkala, "The impulse response and pressure nearfield of a curved radiator," *J. Phys D, Appl. Phys.* vol. 9, pp. 1547-1557, 1976.

[29] M. Arditi, F.S. Foster, and J.M. Hunt, "Transient fields of concave annular arrays," *Ultrason. Imag.,* vol. 3, pp. 37-61, 1981.

[30] H. Djelouah, J.C. Baboux and M. Perdix, " Theoretical and experimental study of the field radiated by ultrasonic focused transducer," Ultrasonics vol. 29, pp. 188-200, (1991).

[31] M.S. Patterson, and F.S. Foster "Acoustic fields of conical radiators," *IEEE Trans. Sonics Ultrason.*, vol.SU-29, pp. 83-92, 1982.

[32] P. Faure, D. Cathignol, and J.Y. Chapelon, "On the pressure field of a transducer in the form of a curved strip," J. Acoust. Soc. Am., Vol. 95, pp. 628-637, (1994).

[33] W.A. Verhoef, M.J.T.M. Cloostermans, and J.M. Thijsssen, "The impulse-response of a focused source with an arbitrary axisymmetric surface velocity distribution," *J. Acoust. Soc. Am.*, vol. 75, pp. 1716-1720, 1984.

[34] J.F. Theumann, M. Arditi, J.J. Meister, and E. Jaques, "Acoustic fields of concave cylindrical transducers", *J. Acoust. Soc. Am.*, Vol. 88, pp. 1160-1169, (1990).

[35] R. Reibold, and R. Kazys, "Radiation of a rectangular strip-like focussing transducers, Part 1: harmonic excitation, Part 2: transient excitation," *Ultrasonics*, Vol. 30, pp. 49-59, (1992).

[36] H.T. O'Neil, "Theory of focusing radiators," *J Acoust. Soc. Am.,* vol. 21, pp. 516-526, 1949.

[37] E.L. Madsen, M.M. Goodsitt, and J.A. Zagzebski, "Continuous waves generated by focused radiators," *J. Acoust. Soc. Am.*, Vol. 70, pp. 1508-1517, 1981.

[38] M.M. Goodsitt, E.L. Madsen, and J.A. Zagzebski, "Field patterns of pulsed, focused, ultrasonic radiators in attenuating and nonattenuating media," *J. Acoust. Soc. Am.*, Vol. 71, pp. 318-329, 1982.

[39] W.N. Cobb, "Frequency domain method for the prediction of the ultrasonic field patterns of pulsed, focused radiators," *J. Acoust. Soc. Am.*, vol. 75, pp.72-79, 1984.

[40] F. Coulouvrat, "Continuous field radiated by a geometrically focused transducer: Numerical investigation and comparison with an approximate model," J. Acoust. Soc. Am., vol. 94, pp. 1663-1675, 1993.

[41] J.P. Weight and A.J. Hayman, "Observations of the propagation of very short ultrasonic pulses and their reflection by small targets," *J. Acoust. Soc. Am.* **63:** 396-404 (1978).

[42] A.J. Hayman and J.P. Weight, "Transmission and reception of short ultrasonic pulses by circular and square transducers," *J. Acoust. Soc. Am.* **66:** 945-951 (1979).

[43] A. Lhemery, "Impulse-response method to predict echo-responses from targets of complex geometry. Part I: Theory," *J. Acoust. Soc. Am.* **90:** 2799-2807, (1991).

[44] A. Lhemery, "Impulse-response method to predict echo-responses from targets of complex geometry. Part II: Computer implementation and experimental validation," *J. Acoust. Soc. Am.* **95:** 1790-1800 (1994).

[45] K. B. Ocheltree and L. A. Frizzell, "Sound field calculation for rectangular sources," IEEE Trans. Ultrason. Ferroelec. Freq. Contr. **36**, 242-248 (1989).

[46] S. McLaren and J.P. Weight, "Transmit-receive mode responses from finite-sized targets in fluid media," *J. Acoust. Soc. Am.* **82:** 2102-2112 (1987).

[47] J. Adach, and R.C. Chivers, "Effective geometrical parameters for a spherical cap transducer," Acustica **62**, 66-74 (1986).

3 Material Characterization -

Quantitative Evaluation of Ultrasonic Attenuation and Statistic Analysis of Microstructure in Polycrystalline metals

3.1 Introduction

In our recent report [1] some results on the evaluation of attenuation and the estimation of grain noise in copper specimens with various grades were presented. The attenuation evaluation had been conducted by means of the spectral shift method (SSM) and attempt to use the log-spectral difference method (LSDM) was made. The estimation of grain noise was carried out using the independent scattering model (ISM). The SSM and the LSDM were applied to the attenuation estimation based on the echoes from front and back surfaces of copper specimens. The results in the report had shown that the SSM gave a stable estimation of attenuation. However, it does not mean that the SSM can provide accurate estimates. We could not apply the LSDM for the estimation because at that time we had not solved the diffraction effect problem that could cause large error in the estimation, or even yield unreasonable results. We have also found that, in the practical situation when an inspected material has low attenuation, the SSM can not give proper estimation since the frequency shift is small.

The LSDM is one of the most commonly used methods for evaluating the attenuation of a material in nondestructive testing and evaluation (NDT&E) [1-5] and the attenuation of tissues in medical ultrasound diagnosis [6,6']. It can be applied to different measurement configurations. Because of the finite size of a transducer, the ultrasonic beam radiated by the transducer spreads out into a diffracted field, which can introduces errors in attenuation evaluation [2,10]. This is so called diffraction effect. Up to now the diffraction effect and its correction have been studied extensively for a long time [7,9]. Early in the forties, Huntington *et al* [7] calculated diffraction using numerical integration of an approximate expression for the piston field attributable to Lommel [8], who had obtained the expressions (valid for large *ka*) by applying the Kirchhoff approximation to the Fresnel diffraction of light by a circular hole n an opaque screen. In a different approach to the problem, Williams [9] used an expression by King [10] to obtain an exact integral for the acoustic diffraction correction. He also further derived an approximate expression that is valid for large *ka* and *z/a*, and numerically evaluated the expression. A better approximation to Williams's exact expression was found by Bass [11]. Later, Bass's method for computing the integrated signal at a circular receiver, equal in size to the source, parallel to it, and centered on the same axis, was generalized by Williams, Jr. [12] to the case where the receiver might have a different radius from the source. Noting the inconsistency of the predictions by Huntington [7] and Williams [9], Seki *et al* [13] recalculated the diffraction correction based on

the approximation formulas of Lommel [8] and Williams [9] but using smaller calculation intervals so that the predictions were in an agreement with the measurements. In late sixties, Gitis and Khimunin [14] gave a review of diffraction effects in ultrasonic measurements. After that, Khimunin [15] published extensive tables of the magnitude of the diffraction correction obtained by numerical integration of Williams's exact expression. Later, Benson and Kiyohara [16] used a high-speed computer to evaluate Lommel's integral and published tables for both the magnitude and the phase of the diffraction correction to great precision.

Van Buren and Rogers [17] showed that the region where z/a is greater than unity, the correct expression for Bass' second approximation gave excellent values for the diffraction correction. Rogers and Van Buren [18] revealed that Lommel integral was able to be evaluated analytically to obtain a simple closed-form expression for the diffraction correction and the simple expression was shown to be a good approximation at all distances from the source, provided that $\sqrt{ka} >> 1$. The Bass's results were also extended to include the effects of no-zero absorption [19]. For pulse-echo attenuation measurements, Papadakis [20] derived an expression for the diffraction correction that takes into account which echoes are used in the measurements, and pointed out the way of accurately applying Seki *et al*'s results. Papadakis also dealt with the diffraction effects in anisotropic media [22-25]. The essence of the theory was adopted from Seki *et al* [13]. For broadband pulse-echo measurements, Papadakis made a special study [26]. He also published a comprehensive paper presenting the diffraction correction [27]. Rhyne [28] studied the diffraction correction based on spatial impulse response method. The effective area of a transducer has also been taken into account in the measurements of ultrasonic attenuation and velocity [29,30]. It should be noted that all the above-mentioned solutions were obtained based on fluid model, and thus the problem has been solved only for longitudinal waves, and it has been confirmed that they work well for isotropic solids [21,22,25].

In later eighties, a more complete elastic model for both longitudinal and shear waves was developed by Schmerr and Sedov [31], and was applied to diffraction correction by Sedov and Schmerr [32]. Later Tang *et al* [33] used the Green's function method to derive another elastic model for longitudinal and shear waves, and also applied it to diffraction correction. However, in all these cases, the correction of diffraction effects has been made in the cases of contact measurements with circular piston transducers.

In the case of immersion and pulse-echo test, only a little work has been done dealing with this diffraction correction. For immersion measurements of ultrasonic scattering, Thompson and Gray [34] developed an analytical, approximate expression for the corrections of diffraction effects of circular flat piston transducers. In the immersion measurements, the frequency and angular dependencies of the scattering amplitude are convolved with those of the transmitting and receiving transducers and the propagation through the liquid-solid and solid-liquid interfaces. The approximate corrections were

presented for these effects for the cases of angle beam inspection through planar, spherically curved or cylindrically curved surfaces. This analytical expression was originally derived by Rogers and Van Buren [17], and it is equivalent to an expansion in Lommel functions derived by Seki *et al* [13]. Conceptually, it is equivalent to using the effective thickness of the immersed specimen, which is the product of the specimen's thickness and the refraction index (the radio of the specimen and fluid velocities). The effective thickness concept was also used by Simpson and McClung [35] to treat the immersion measurements. This analytical model has become widely used, e.g., in scattering measurements [36,37] and reflection and transmission measurements on viscoelastic plates [38,39].

For spherically focused transducers, several researchers also made the diffraction corrections [40-42].

In medical ultrasonics, extensive researches on the diffraction effects and their corrections have been made [43-61].

Besides in the attenuation and scattering measurements, the diffraction effects also need correcting in the measurements of velocity [2-5,14,14',62-64] and radiation force [65,66], and in ultrasonic interferometers [67,68].

From the above review of literature in a wide scope, we have not found that the diffraction corrections have been done for the linear arrays used in the immersion measurements. In the present work, we have developed an exact method for correcting the diffraction effects for the linear array with a cylindrically curved surface used in immersion measurements of attenuation so that the LSDM can be applied to quantitative attenuation estimation.

As for estimation of grain noise, quite a lot of work was done last year and presented in our recent report [1]. Presently, the independent scattering model (ISM) is still used to estimate the grain noise, and the K-distribution model (KDM) is also applied. Some newly coming copper specimens with different grades have been inspected. The estimated results from two methods are compared.

3.2 Quantitative evaluation of ultrasonic attenuation in polycrystalline metals

For the mechanism of attenuation in a polycrystalline metal and the methods (the SSM and the LSDM), the reader is referred to our recent report [1]. It should be pointed out that the longitudinal wave (LW) case is of our present interest since the normally incident beam is used in the attenuation evaluation.

It is known that in general an attenuation coefficient α, used as a measure of the attenuation, consists of two types of attenuation, the scattering attenuation α_s and the absorption attenuation α_a, both dependent on frequency *f*, i.e., on the ratio of wavelength to grain size. In our application the wavelength is in the same range as grain size and the scattering dominates the attenuation. In this

case, the attenuation of a polycrystalline material is determined almost entirely by scattering from grains, that is $\alpha(f) \approx \alpha_s(f)$. The log-spectral difference method (LSDM) is one of the most commonly-used methods for attenuation evaluating. For example, in the case of a plane wave used in an immersion test of an attenuating solid plate (see Fig. 3.1), the LSDM evaluates the attenuation coefficient based on the following relation taking into account reflection and transmission coefficients at front and back interfaces [1],

$$\alpha_L(\omega) = \frac{1}{2D} \ln \frac{4\rho c \rho_s c_L}{(\rho c + \rho_s c_L)^2} \frac{|P_{rF}(\omega)|}{|P_{rB}(\omega)|}, \tag{3.1}$$

where $P_{rF}(\omega)$, and $P_{rB}(\omega)$ are the Fourier transform of the transient plane waves reflected from the front and the back surfaces. They originate from the incident plane wave $P(\omega)$, denoting the Fourier transform of the incident transient plane wave $p(t)$. For a finite-size transducer, however, the diffraction has severe effect on evaluation of attenuation, and may cause completely wrong results. Such an effect is encountered both for transmitters and receivers. Therefore, it must be corrected to achieve an accurate evaluation.

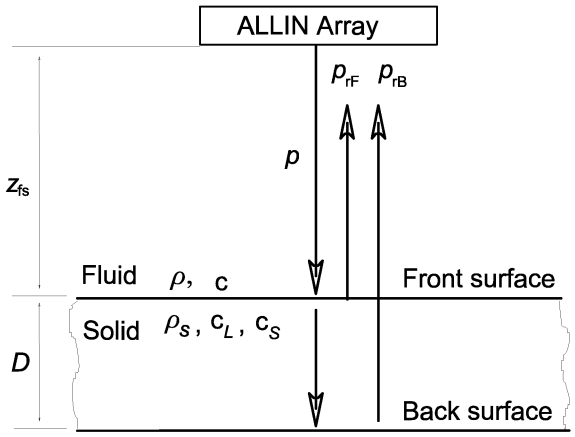

Fig. 3.1. Measurement set-up for the estimation of attenuation coefficient from reflected ultrasound.

3.2.1 Effects of diffraction on attenuation evaluation

First let us look at some measurements to see how the diffraction affects the attenuation evaluation. The measurements were made on a 19.3-mm thick copper plate using a normally incident beam radiated by the ALLIN array that was positioned at distances of 131 and 161 mm to the copper plate, which means that the water path length is 131 and 161 mm, respectively. The ALLIN array has a cylindrically concave surface with a 190-mm radius of curvature. The measurement set-up used is shown in Fig. 3.1, and the measurements were made under the same conditions except at different

distances. The array was electronically unfocused. The measured results are shown in Fig. 3.2, and to facilitate the comparison they were normalized by their front echoes' peak amplitudes of 82 and 97, respectively.

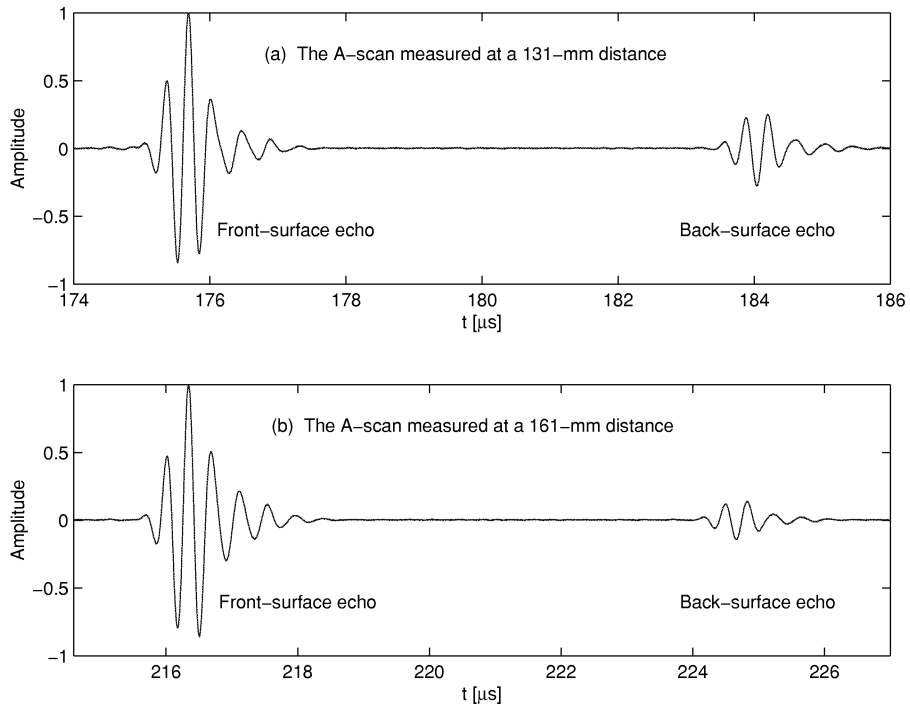

Fig. 3.2. The A-scans measured on the 19.3-mm-thick copper plate at distances of (a) z_{fs} =131 and (b) z_{fs} =161 mm to the array. The A-scans are normalized by their front echoes' peak amplitudes, 82 and 97, respectively.

From Fig. 3.2, it can be seen that in these two measurements, although made on the same specimen, the peak amplitude ratios of back-surface echo to front-surface echo are different, specifically, the first one (0.28 in Fig. 3.2(a)) is two times larger than the second (0.14 in Fig. 3.2(b)). Apparently, we will obtain different results if we use the two measurements to evaluate the attenuation coefficient, which is different from the plane wave case in Eq. (3.1). Also, given the sound velocity in water that is 1494 m/s, the LW and SW velocities in the copper plate that are 4643 m/s and 2260 m/s, and their densities of 1000 $\mathrm{kg/m^3}$ and 8960 $\mathrm{kg/m^3}$, respectively, we have $4\rho c\rho_s c_L/(\rho c+\rho_s c_L)^2$ =0.1339 and the attenuation coefficient evaluated by Eq. (3.1) can become negative valued, which is obviously not true.

The above analysis has demonstrated the effect of diffraction on the attenuation evaluation, and, thus, to make use of the LSDM for correct evaluation with good accuracy, the diffraction effect on the attenuation evaluation must be corrected. It is worth noting that for the electronically focused array the respective results would be more realistic.

3.2.2 Fundamentals of attenuation evaluation with diffraction correction

To introduce the method for correcting the diffraction effect on attenuation evaluation, we start with two simple examples. The first one is the case of the spherical waves propagating in an attenuating medium and measured by a point-like receiver, the second is the case of an ultrasonic beam radiated by a finite-size transmitter and measured by a point-like receiver. Then we consider the case of spherical waves propagating in an attenuating medium and measured by a finite-size (circular) receiver. The examples help to understand the fundamentals of diffraction effect and the idea behind the diffraction correction in a simple and intuitive way without getting into any profound theory in physical acoustics.

3.2.2.1 Evaluation of attenuation using a point receiver

A. The case of a spherical wave

A spherical pressure wave with frequency ω traveling through an unbounded medium with attenuation coefficient, α, is written as

$$p(r) = \frac{A}{r}\exp(-\alpha r)\exp(jk_0 r) = p_0(r)\exp(-\alpha r) \tag{3.2}$$

where A is an initial amplitude at $r = a$ (a is the radius of the spherical source), $r = \sqrt{x^2 + y^2 + z^2}$, $k_0 = 2\pi/\lambda = \omega/c$ is the propagation constant (the wave number when the attenuation is assumed to be zero), c is the sound velocity, and $p_0(r) = A\exp(jk_0 r)/r$ is the spherical wave propagating in this unbounded medium when its attenuation is assumed to be zero. Obviously, in this non-attenuating medium, the amplitude of the spherical wave is distance dependent, i.e., it decreases with increasing r due to beam-spreading. Assuming that the wave propagates from r_1 to $r_2 = r_1 + d$ and their pressures $p(r_1)$ and $p(r_2)$ at r_1 and r_2 are measured by a point-like receiver, we have

$$p(r_1) = \frac{A}{r_1}\exp(-\alpha r_1)\exp(jk_0 r_1) = p_0(r_1)\exp(-\alpha r_1), \tag{3.3a}$$

$$p(r_2) = \frac{A}{r_2}\exp(-\alpha r_2)\exp(jk_0 r_2) = p(r_1)\frac{p_0(r_2)}{p_0(r_1)}\exp(-\alpha d). \tag{3.3b}$$

From Eq. (3.3b), the exact attenuation coefficient can be found to be

$$\alpha = \frac{1}{d}\ln\left(\frac{|p(r_1)/p_0(r_1)|}{|p(r_2)/p_0(r_2)|}\right) = \frac{1}{d}\left(\ln\frac{|p(r_1)|}{|p(r_2)|} - \ln\frac{|p_0(r_1)|}{|p_0(r_2)|}\right). \tag{3.4}$$

This equation basically shows the way of how to correct the diffraction effect to achieve an accurate evaluation. From this equation, it can be seen that $\left(\ln|p(r_1)/p(r_2)|\right)/d > \alpha$, which means that the attenuation is overestimated if $p_0(r_1)/p_0(r_2)$ is not taken into account. Since the point-like receiver is used to measure the pressure, the diffraction effect can be completely eliminated using Eq. (3.4).

B. The case of an ultrasound field radiated by a finite-size piston source

An ultrasound field radiated by an infinite-baffled, finite-size piston source into an attenuating medium can be obtained by superimposing point sources into which the finite piston source is divided, and it is, therefore, written in the Rayleigh integral with wave number of $k = k_0 + j\alpha$ [69],

$$p(x,y,z) = -\frac{jk\rho c}{2\pi}\iint_S v(x',y',z')\frac{\exp\left[(-\alpha + jk_0)r'\right]}{r'}dx'dy' \qquad \text{for } z \geq z', \tag{3.5}$$

where $r' = \sqrt{(x-x')^2 + (y-y')^2 + (z-z')^2}$, $v(x,y,z)$ is the normal velocity distribution in the source surface S, $k_0 = 2\pi/\lambda = \omega/c$, and α is the attenuation coefficient which is frequency-dependent. The integration is conducted over the source surface S. For a planar piston source, the pressure in Eq. (3.5) can be evaluated by the method proposed by Ocheltree and Frizzell [69],

$$p(x,y,z) = \frac{jk_0\rho c}{2\pi}\sum\frac{v(x',y',z')}{R}\exp\left[(-\alpha + jk_0)R\right]\operatorname{sinc}\frac{k_0 x'_n\,\Delta h}{R}\operatorname{sinc}\frac{k_0 y'_n\,\Delta h}{R} \tag{3.6}$$

where ρ is the density of the medium, $R = \sqrt{(x-x'_n)^2 + (y-y'_n)^2 + (z-z')^2}$, Δw and Δh are the sides of N small rectangular subelements divided from the source, $x'_n = x' - x_n$ and $y'_n = y' - y_n$, and (x_n, y_n) is the position of the nth subelement center. In the nearfield region, the attenuated field $p(x, y, z)$ does not look obvious. In the farfield, we have the approximation of $R \approx \sqrt{x^2 + y^2 + z^2} = r$, and Eqs. (3.5) and (3.6) can be approximated into the following form [70,71]

$$p(x,y,z) = \frac{jk\rho c}{2\pi r}V(k_x,k_y)\exp(jkr) \tag{3.7a}$$

where $V(k_x, k_y)$ is the farfield beam pattern (or the angular spectrum) of the source, and $(k_x, k_y) = k(\cos\varphi \sin\theta, \sin\varphi \sin\theta)$. Replacing k with $k = k_0 + j\alpha$ and considering $k_0 >> \alpha$ in the amplitude factor $jk\rho cV(k_x, k_y)/2\pi r$ ($k_0 >> \alpha$ is quite common in polycrystalline metals, e.g., for a highly attenuating metal with α=1000 dB/m $\approx$ 115 Np/m at 3 MHz and with a longitudinal wave velocity of 4660 m/s, k=4045+j115), Eq. (3.5a) can further be simplified to

$$p(x, y, z) = \frac{jk_0\rho c}{2\pi r} V(k_{0x}, k_{0y}) \exp(-\alpha r) \exp(jk_0 r) = p_0(r; k_{0x}, k_{0y}) \exp(-\alpha r), \qquad (3.7b)$$

where $p_0(r; k_{0x}, k_{0y}) = jk_0\rho cV(k_{0x}, k_{0y}) \exp(jk_0 r)/(2\pi r)$, $(k_{0x}, k_{0y}) = k_0(\cos\varphi \sin\theta, \sin\varphi \sin\theta)$, and φ and θ are the azimuth angle and the polar angle, respectively. Eq. (3.7b) shows that in the far-field region the ultrasound field from a finite source in an attenuating medium is similar to the spherical wave field except that the amplitude p_0 is direction dependent. Due to the similarity in form, the attenuation coefficient in the present case can be evaluated in a same way (using Eq. (3.4)) as in the case of spherical wave for the point-like receiver. For a rectangular piston source with a 2ax2b dimension, $V(k_x, k_y) = 4ab \sin(k_x a) \sin(k_y b) / (k_x a k_y b)$. On the axis, θ=0, and p_0 has the same form as the spherical wave, namely, $p_0(r; k_{0x}, k_{0y}) = A \exp(jk_0 r)/r$, where A is constant.

The above analysis has revealed that like a spherical wave an ultrasonic beam from a finite-size transducer can be also used to quantitatively estimate the attenuation of a medium because the diffraction effect can be eliminated (at least in the far field region). But it should be pointed out that the receiver used for measuring fields is point-like. In reality, finite-size receivers are most often used.

3.2.2.2 Evaluation of attenuation using a finite-size receiver

In practice, to evaluate the attenuation in a medium, a transmitter and a receiver are needed to generate and detect a field, respectively. When a point-like receiver was used to measure a field in a medium, the field $p(r)$ at point **r** was measured. In a real case of measuring an ultrasonic field, a finite-size transducer is usually used as receiver which is phase sensitive and yields phase cancellation effect, that is, the diffraction effect of the receiver. In this case, the pressure field measured by the receiver is not $p(\mathbf{r})$ at point **r**=(x, y, z), but the average field over the receiver surface. Now we shall study such a measured field.

Suppose that a receiver used for the measurement has an area of S and is placed at r with its axis being in coincidence with the wave propagation, the pressure detected by the receiver is the average value of $p(r)$ over the receiver area S, and from [13] it can be written as

$$\langle p(r)\rangle = \frac{1}{S}\int\int_S p(r')ds. \tag{3.8}$$

Now let us consider the example where the attenuation coefficient is evaluated using a finite size transducer to measure a spherical wave field. Suppose the receiver is circular, piston-like with radius a, and the axis of the receiver is in the direction of wave propagation. According to the reciprocity of transmitting and receiving of the same transducer, the spherical wave pressure received by this circular transducer at position **r** is equal to the on-axis field radiated by the transducer, which can be expressed in analytical from as follows [72],

$$\langle p(r)\rangle = \frac{Q}{\pi a^2}\left[\exp\left(jk\sqrt{r^2+a^2}\right) - \exp(jkr)\right], \tag{3.9}$$

where $Q = \rho c v_0$ is constant for a planar piston receiver. In an attenuating medium, we substitute $k = k_0 + j\alpha$ into the above equation and consider the case where the point source radiating the spherical wave is located in the transducer farfield region so that $\exp\left[-\alpha\left(\sqrt{r^2+a^2}-r\right)\right] \approx 1$ is satisfied. In this way, the above equation may reduce to

$$\langle p(r)\rangle = \langle p_0(r)\rangle \exp(-\alpha r), \tag{3.10}$$

where

$$\langle p_0(r)\rangle = \frac{Q}{\pi a^2}\left[\exp\left(jk_0\sqrt{r^2+a^2}\right) - \exp(jk_0 r)\right]. \tag{3.11}$$

Obviously, $\langle p_0(r)\rangle$ is just the on-axis field in the lossless medium from the corresponding transmitter. The attenuation coefficient can, therefore, be exactly evaluated in this manner,

$$\alpha = \frac{1}{d}\ln\frac{|\langle p(r_1)\rangle / \langle p_0(r_1)\rangle|}{|\langle p(r_2)\rangle / \langle p_0(r_2)\rangle|} = \frac{1}{d}\left(\ln\frac{|\langle p(r_1)\rangle|}{|\langle p(r_2)\rangle|} - \ln\frac{|\langle p_0(r_1)\rangle|}{|\langle p_0(r_2)\rangle|}\right). \tag{3.12}$$

The above analysis demonstrates that, when the measurement is made in the farfield region of the receiver, diffraction effect can be almost completely corrected so that Eq. (3.12) can give an accurate estimation of attenuation in a medium. Eq. (3.12) is exactly the same in form as Eq. (3.4).

3.2.3 Quantitative evaluation of attenuation using the ALLIN array with diffraction correction

In Sec. 3.2.2, we have discussed the evaluation of attenuation with diffraction correction for three simple cases. In these cases, the measurements of attenuated fields were conducted in homogeneous media using transmission mode, and the correction of diffraction could be made analytically. In reality, finite-size transmitters and receivers are usually used to generate and detect ultrasonic fields, and in this real case, the correction of diffraction is not so easy and the analytical formulas for the correction are not available at all. In general, the correction of diffraction is numerically implemented in the case where finite-size transmitters and receivers are used for evaluation.

In this section, we will deal with the evaluation of attenuation in immersion test, based on the ALLIN ultrasonic array system, and develop a method to correct the diffraction effect. The method is based on the extended angular spectrum approach (ASA) that was developed by us to calculate the angular spectrum of the ALLIN array with a cylindrically concave surface [1,73]. In the immersion test, the reflected fields from the front and back surfaces of an attenuating solid plate are used to make attenuation evaluation (see Fig. 3.1). The front surface is a fluid/solid interface and the back is a solid/fluid interface. The situation to be considered here is such that the ultrasonic beam generated by the ALLIN array is normally incident on a copper plate immersed in water, and the front and back surfaces are parallel. First we make a theoretical modeling of diffraction correction for quantitative evaluation of attenuation, and then we put the model into practical use through comparing the measured results with their corresponding calculated results.

3.2.3.1 Theory for quantitative evaluation of attenuation with diffraction correction

It is well known that waves propagate in a solid in different wave modes, mainly longitudinal wave (LW) and transverse wave (SW). In the normal incidence on a solid, the SW field is very small compared to the LW field. Therefore, only the attenuation coefficient of LW fields in the attenuating solid will be investigated. In the immersion measurement, the attenuation in a fluid (usually water) is very small, and thus will be neglected in the following study, i.e., $k = k_0 = \omega / c$ from the convention of notation used in Sect. 3.2.2. In an attenuating solid, the LW wave vector is denoted by $\mathbf{k}_L = k_L \hat{\mathbf{k}}_L$

where $k_L = k_{0L} + j\alpha_L$ with $k_{0L} = \omega / c_L$ and $\hat{\mathbf{k}}_L$ is a unit vector. Under these assumptions, we apply the ASA to calculate the pulse-echoes from the front and back surfaces of the attenuating immersed plate. The calculation procedure is schematically shown in Fig. 3.3.

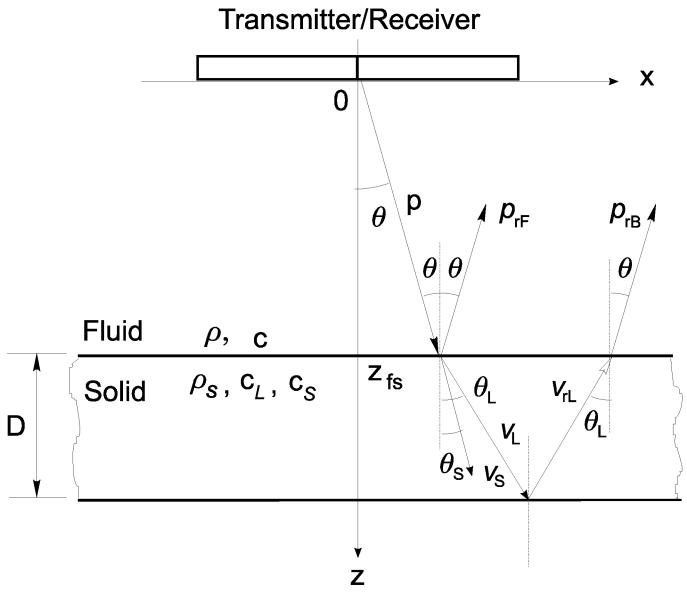

Fig. 3.3. Geometry and notation for the ASA to calculate the reflections from a copper plate.

Considering a curved transducer with normal velocity pulse excitation $v_n(x, y, z; t)$ on its surface area S, the time-harmonic component of the normal velocity at frequency ω, denoted by $\tilde{v}_n(x, y, z; \omega)$, can be obtained using Fourier transform. From [73], it follows that a time-harmonic field of the curved transducer with $\tilde{v}_n(x, y, z; \omega)$ can be represented by an angular spectrum of plane waves, $V(k_x, k_y; z_1)$, in a plane at $z = z_1$. A pressure plane wave in the fluid at point (x, y, z) resulting from the plane wave $V(k_x, k_y; z_1)\ \exp\left[j\left(xk_x + yk_y + (z - z_1)k_z\right)\right]$ can be expressed as,

$$P(k_x, k_y; x, y, z) = k\rho c V(k_x, k_y; z_1) \frac{\exp\left[j\left(xk_x + yk_y + (z - z_1)k_z\right)\right]}{k_z}, \quad (z \geq z_1), \tag{3.13}$$

where $k_x = kn_x$, $k_y = kn_y$, $k_z = \sqrt{k^2 - k_x^2 - k_y^2} = k\sqrt{1 - n_x^2 - n_y^2}$ are the spatial frequencies in the x-, y- and z-directions in the fluid. The propagation direction of the plane wave can be expressed by wave vector $\mathbf{k} = (k_x, k_y, k_z)$ or the direction cosines $\mathbf{n} = (n_x, n_y, n_z) = (\sin\theta\cos\phi, \sin\theta\sin\phi, \cos\theta)$. At the front (fluid/solid) interface at $z = z_{fs}$ the plane wave expressed in Eq. (3.13) is incident on the interface and reflected. The reflected wave can be written, in terms of pressure, as

$$P_{rF}(k_x,k_y;x,y,z) = R_{fs}(k_x,k_y)P(k_x,k_y;x,y,z_{fs})\exp\left[-j(z-z_{fs})k_z\right]$$

$$= \frac{k\rho cV(k_x,k_y;z_1)R_{fs}(k_x,k_y)\exp\left[j(xk_x+yk_y-(z+z_1-2z_{fs})k_z)\right]}{k_z},\ (z \le z_{fs}) \qquad (3.14)$$

where $R_{fs}(k_x,k_y)$ is the reflection coefficient at the fluid/solid interface. The transmitted longitudinal wave (LW) in terms of particle velocity can be found to be [73]

$$\mathbf{V}_L(k_x,k_y;x,y,z) = \frac{\hat{\mathbf{L}}k_L T_{fs}(k_x,k_y)P(k_x,k_y;x,y,z_{fs})\exp\left[j(z-z_{fs})k_{zL}\right]}{k\rho c}$$

$$= \frac{\hat{\mathbf{L}}k_L V(k_x,k_y;z_1)T_{fs}(k_x,k_y)\exp\left[j\left(xk_x+yk_y+(z-z_{fs})k_{zL}+(z_{fs}-z_1)k_z\right)\right]}{k_z},$$

$$(z_{fs} \le z \le z_{fs}+D), \qquad (3.15)$$

where $T_{fs}(k_x,k_y)$ is the transmission coefficient at the fluid/solid interface, and the relations $k_{xL}=k_x$ and $k_{yL}=k_y$ is used in the LW vector, namely $\mathbf{k}_L=(k_{xL},k_{yL},k_{zL})=(k_x,k_y,k_{zL})$. The relations come from Snell's law stating $k\sin\theta = k_L\sin\theta_L$ in which θ_L is the LW refraction angle determined from the incident angle θ. Thus, the LW vector can alternatively be written as $\mathbf{k}_L = k_L(n_{xL},n_{yL},n_{zL}) = (k\sin\theta\cos\phi, k\sin\theta\sin\phi, k_L\cos\theta_L)$ which is associated with the incident wave vector $\mathbf{k}$. At the back (solid/fluid) interface, the transmitted LW is reflected and the reflected LW can be written as

$$\mathbf{V}_{rL}(k_x,k_y;x,y,z) = \hat{\mathbf{L}}_r R_{sf}(k_x,k_y)V_L(k_x,k_y;x,y,z_{fs}+D)\exp\left[-j(z-z_{fs}-D)k_{zL}\right]$$

$$= \frac{\hat{\mathbf{L}}_r k_L V(k_x,k_y;z_1)R_{sf}(k_x,k_y)T_{fs}(k_x,k_y)\exp\left[j\left(xk_x+yk_y-(z-z_{fs}-2D)k_{zL}+(z_{fs}-z_1)k_z\right)\right]}{k_z}$$

$$(z_{fs} \le z \le z_{fs}+D), \qquad (3.16)$$

where $R_{sf}(k_x,k_y)$ is the reflection coefficient at the solid/fluid interface. At the front (solid/fluid) interface, the transmitted LW is reflected and the reflected LW can be written as

$$P_{rB}(k_x,k_y;x,y,z) = \frac{k\rho cT_{sf}(k_x,k_y)V_{rL}(k_x,k_y;x,y,z_{fs})\exp\left[-j(z-z_{fs})k_z\right]}{k_L}$$

$$= \frac{k\rho cV(k_x,k_y;z_1)T_{sf}(k_x,k_y)R_{sf}(k_x,k_y)T_{fs}(k_x,k_y)\exp\left[j\left(xk_x+yk_y-(z-2z_{fs}+z_1)k_z+2Dk_{zL}\right)\right]}{k_z}$$

$$= \frac{T_{sf}(k_x,k_y)R_{sf}(k_x,k_y)T_{fs}(k_x,k_y)}{R_{fs}(k_x,k_y)}\exp\left[j2Dk_{zL}\right]P_{rF}(k_x,k_y;x,y,z). \qquad (z \le z_{fs}). \tag{3.17}$$

Inserting the relations $k_{zL} = k_L \cos\theta_L$ and $k_L = k_{0L} + j\alpha_L$ into the above equation, the LW attenuation of the solid plate can be explicitly expressed. The reflection and refraction coefficients at the fluid/solid interface, R_{fs} and T_{fs}, can be found in [75, 76], and those at the solid/fluid interface, R_{sf} and T_{sf}, are given in [76] and also in Appendix 3-A.

Superimposing all the plane waves in Eqs. (3.14) and (3.17), respectively, the reflected time-harmonic fields from the front and back surfaces can be obtained, as follows,

$$\tilde{p}_{rq}(x,y,z;\omega) = \frac{1}{(2\pi)^2}\int_{-\infty}^{\infty}\int_{-\infty}^{\infty} P_{rq}(k_x,k_y)dk_x dk_y\,, \tag{3.18}$$

where q = F, or B. When the reflected fields are measured by the same transducer, the measured pressures can be expressed as (see Eq. (3.8)),

$$\left\langle \tilde{p}_{rq}(\omega)\right\rangle = \frac{1}{S}\int\int_S \tilde{p}_{rq}(x',y',z';\omega)dx'dy'\,, \tag{3.19}$$

where $z'=f(x', y')$ defines the surface of the curved transducer. Eq. (3.19) indicates that the fields $\tilde{p}_{rq}(x,y,z;\omega)$ on the transducer surface S are summed up coherently and thus phase cancellation occurs. The phase cancellation results in the diffraction of the receiver. To obtain the pulse-echoes from the front and back surfaces, namely, the pressures measured by the receiver, we can perform Fourier transform to Eq. (3.19), and thus we have,

$$\left\langle p_{rq}(t)\right\rangle = \int_{-\infty}^{\infty}\left\langle \tilde{p}_{rq}(\omega)\right\rangle e^{-j\omega t}d\omega\,. \tag{3.20}$$

To evaluate attenuation, we actually need Eq. (3.19) to calculate the time-harmonic components, $\left\langle \tilde{p}_{rq}(\omega)\right\rangle$, which is dependent on frequency ω, and correct the diffraction effect for each of the components using the similar way in Eq. (3.12). Because the pulse-echoes are used, their propagating path length is $2D$, and the LW attenuation coefficient is evaluated with diffraction correction in the manner,

$$\alpha_L(\omega)=\frac{1}{2D}\ln\frac{\left|\left\langle\tilde{p}_{rF}(\omega)\right\rangle/\left\langle\tilde{p}_{0rF}(\omega)\right\rangle\right|}{\left\langle\tilde{p}_{rB}(\omega)\right\rangle/\left\langle\tilde{p}_{0rB}(\omega)\right\rangle}, \tag{3.21}$$

where $\left\langle\tilde{p}_{0rq}(\omega)\right\rangle$ are the fields (usually calculated) with $\alpha_L=0$. As the attenuation in a fluid (usually water) is very small and neglected, the echoes from the front surface are the same, i.e., $\left\langle\tilde{p}_{rF}(\omega)\right\rangle=\left\langle\tilde{p}_{0rF}(\omega)\right\rangle$. Therefore, Eq. (3.21) becomes,

$$\alpha_L(\omega)=\frac{1}{2D}\ln\frac{\left|\left\langle\tilde{p}_{0rB}(\omega)\right\rangle\right|}{\left|\left\langle\tilde{p}_{rB}(\omega)\right\rangle\right|}. \tag{3.22}$$

α_L in Eqs. (3.21) or (3.22) is in NP/m, and for dB/m, use the conversion, 1 NP = 8.686 dB. In a real situation, $\left\langle\tilde{p}_{rq}(\omega)\right\rangle$ come from measurements, and $\left\langle\tilde{p}_{0rq}(\omega)\right\rangle$ from calculations.

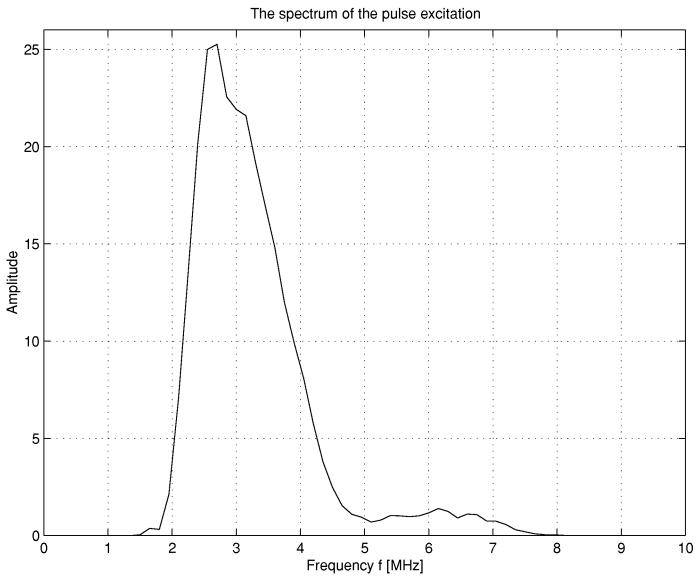

Fig. 3.4. The spectrum of the pulse excitation $v_n(x,y,z;t)$ in terms of amplitude.

3.2.3.2 Theoretical and experimental evaluation of attenuation with diffraction correction

Now we apply the above-developed theory to a specific case given in Sect. 3.2.1. Using the normal velocity pulse excitation $v_n(x,y,z;t)$ of the ALLIN array that has been determined and given in Fig. 2.9(d) in Chap. 2, and employing Eqs. (3.13)-(3.20), we calculate the pulse-echoes from the front and back surfaces with geometry and physical parameters given in Sect. 3.2.1. The amplitude spectrum of the pulse excitation is shown in Fig. 3.4. From the spectrum, we can see that the majority of the pulse

excitation energy is concentrated in the frequency range from 1.5-8 MHz. Therefore, the time-harmonic components, $\langle \tilde{p}_{rq}(\omega) \rangle$, are calculated only in this frequency range. Based on the calculated pulse-echoes from the immersed copper plate in the attenuating and non-attenuating cases, we first make a theoretical test of the method for diffraction correction in order to show the correctness of the theory, and then apply it to a real situation of attenuation evaluation.

A. Theoretical test of the correcting method

Assuming that the attenuation coefficient is linear frequency dependent, we $\alpha_L(f) = \beta f$, where β is constant. Although this assumption does not apply to our case, here we use it to test whether we can still obtain such a linear-frequency-dependent attenuation coefficient using Eq. (3.22) with the calculated, back-surface echoes (in the transform domain), $\langle \tilde{p}_{0rB}(\omega) \rangle$ and $\langle \tilde{p}_{rB}(\omega) \rangle$, which are non-attenuated and attenuated, respectively. Therefore, the correctness of the theory is verified.

Given α_L=0.15 dB/mm at a 3 MHz frequency, i.e., β = 0.03 dB/mm/MHz, the pulse-echoes from the attenuating copper plate, $\langle p_{rF}(t) \rangle$ and $\langle p_{rB}(t) \rangle$, were calculated, first using Eqs. (3.14) and (3.17), respectively, and then using Eqs. (3.18)-(3.20). Letting α_L=0, the pulse-echoes from the copper plate in the non-attenuation case, $\langle p_{0rF}(t) \rangle$ and $\langle p_{0rB}(t) \rangle$, were calculated. In Fig. 3.5 are shown the results that are calculated in the cases of attenuation (dotted) and non-attenuation (solid) at (a) z_{fs}=131 and (b) z_{fs}=161 mm. Since the attenuation in water is neglected, the front-surface echoes $\langle p_{rF}(t) \rangle$ and $\langle p_{0rF}(t) \rangle$ are the same for the two cases. Whereas, the back-surface echoes $\langle p_{rB}(t) \rangle$ and $\langle p_{0rB}(t) \rangle$ are different, specifically speaking, $\langle p_{rB}(t) \rangle$ is smaller than $\langle p_{0rB}(t) \rangle$ because of the attenuation in the plate. For both cases, we apply Eq. (3.22) to evaluate the attenuation coefficients of the copper plate for z_{fs}=131 and z_{fs}=161 mm, respectively, which are almost exactly the same. The evaluated result (dotted) for z_{fs}=131 together with the exact result ($\alpha_L = \beta f$ in which β = 0.03 dB/mm/MHz and *f* is in MHz) are illustrated in Fig. 3.6. If we magnify the figure, we can find that the evaluated result is always slightly smaller than the exact result, and the error is less than two percent. From this, we can conclude that the diffraction effect of the ALLIN array can, in principle, be corrected up to a very high precision using the method developed above. In reality, we may not obtain such a good agreement because of practical reasons.

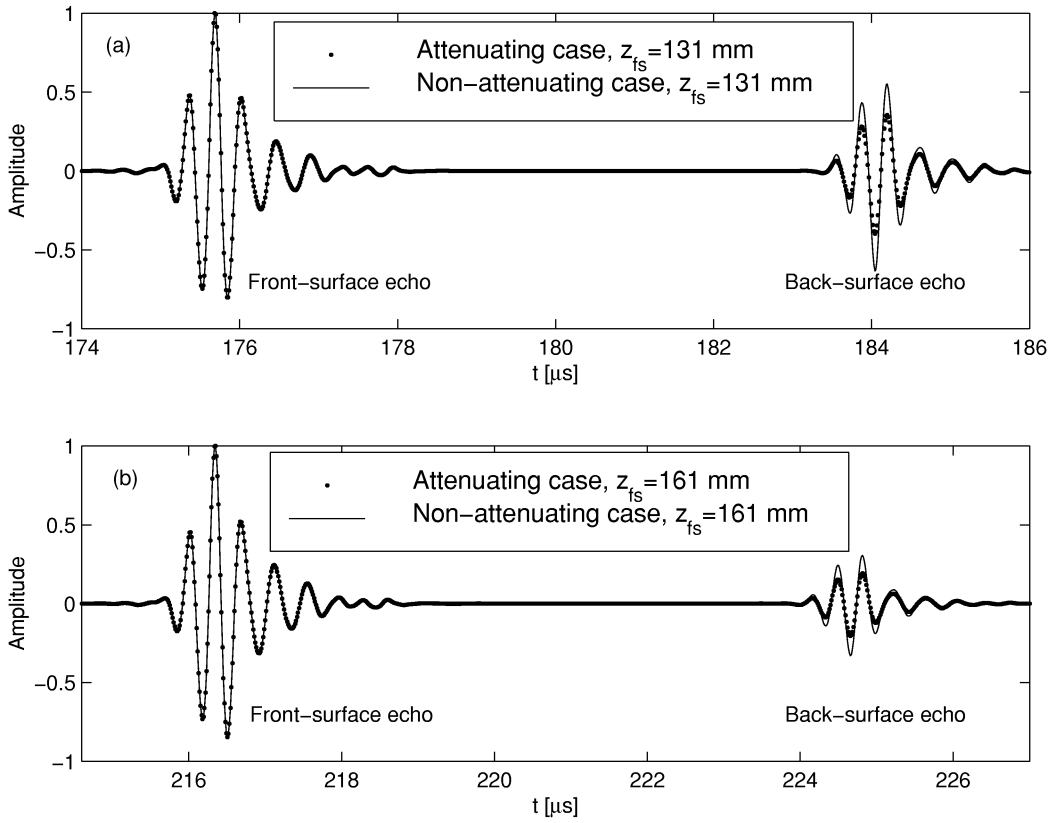

Fig. 3.5. The calculations of the attenuated echoes (dotted) and the non-attenuated (solid) echoes from the 19.3-mm-thick copper plate at distances of (a) z_{fs} =131 and (b) z_{fs} =161 mm to the array. They are normalized by their front echoes' peak amplitudes, respectively.

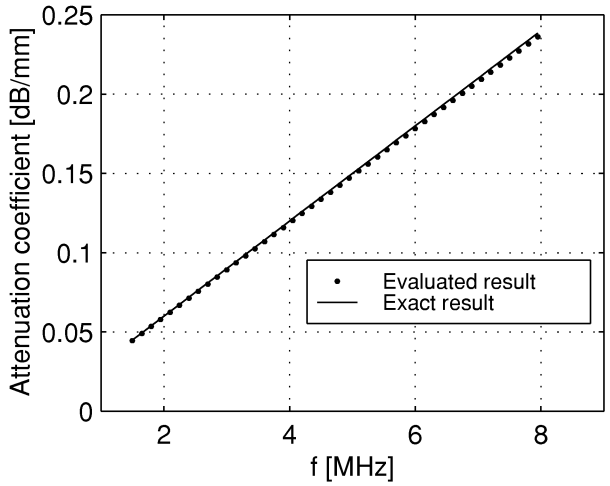

Fig. 3.6. The evaluated attenuation (dotted) of the copper plate when z_{fs} =131 mm, and the exact attenuation (solid).

B. Quantitative evaluation of attenuation for a real situation

Applying Eq. (3.21) or (3.22) to a real situation of attenuation evaluation, the pulse-echoes from the copper plate in the non-attenuation case need calculating, in addition to measuring the echoes from the attenuating plate. The calculated (solid) and the measured (dotted) echoes are

comparatively shown in Fig. 3.7. Note that the calculated results in Figs. 3.5 and 3.7 are exactly the same. From Fig. 3.7, we can see that on the whole the calculated and the measured front-surface echoes, but a small difference still exists, especially for the measurement at z_{fs}=131 mm. Using the calculated back-surface echoes and the measured ones in Eq. (3.22), the attenuation coefficients have been evaluated for the two measurements, and are shown in Fig. 3.8 as a function of frequency.

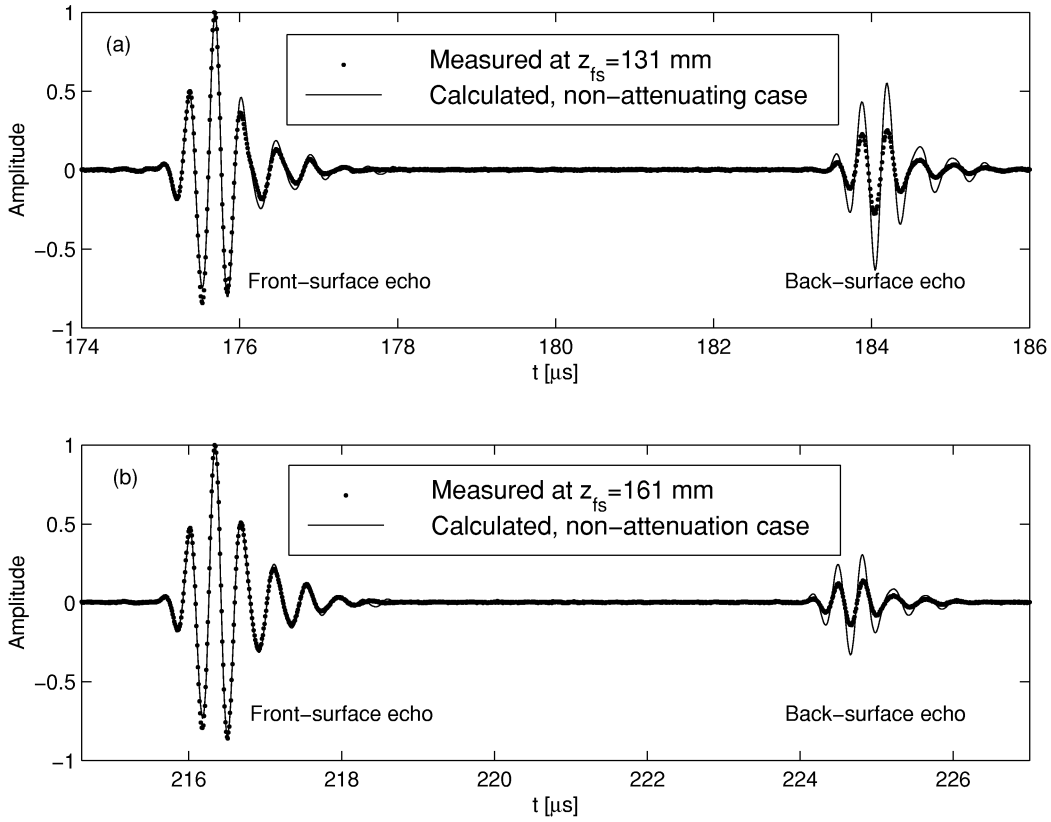

Fig. 3.7. The measured echoes (dotted) and the calculated, non-attenuated echoes (solid) from the 19.3-mm-thick copper plate at distances of (a) z_{fs}=131 and (b) z_{fs}=161 mm to the array. The signals are normalized by their front echoes' peak amplitudes, respectively.

In Fig. 3.8, it can be seen that the evaluated attenuation coefficients for z_{fs}=131 mm and z_{fs}=161 mm are close only in the frequency range of 2-4.5 MHz, unlike the theoretical case presented in Sect. 3.2.3.2A. A reason for this is that the energy of the pulse excitation is concentrated in this frequency range (refer to Fig. 3.4) so that the estimations outside this range are unreliable because noise energy can be larger and quantization error can have significant influence. In the frequency range of 2–4.5 MHz, the evaluations give quite reasonable attenuation values that increase with frequency in non-linearity.

In principle, the coefficients evaluated from the two measurements should not be different. In practice, there are quite a few factors, both experimentally and theoretically, that may cause the difference of the evaluations. Experimentally, the sound velocities could be measured inaccurately, or the surfaces of the transducer and the copper plate could not be placed exactly in parallel. In the theoretical aspect, the piston-like vibration on the transducer surface used in the ultrasonic field model was not precise, and thus the effective geometrical parameters of the transducer needed determining precisely. The use of inaccurate parameters will cause the inaccuracy in calculating the pulse excited normal velocity and the echoes, e.g., in Fig. 3.7 where we can see some differences between the calculated and measured front-surface echoes. Another possible error source is the neglecting of nonlinear propagation effects [77,78]. The numerical implementation of the ASA and the FFT may be a small error source. These above-mentioned factors, meanwhile, indicate some aspects in which we need to do more work for more accurate estimation. When these factors are improved, the correcting method can give better estimations.

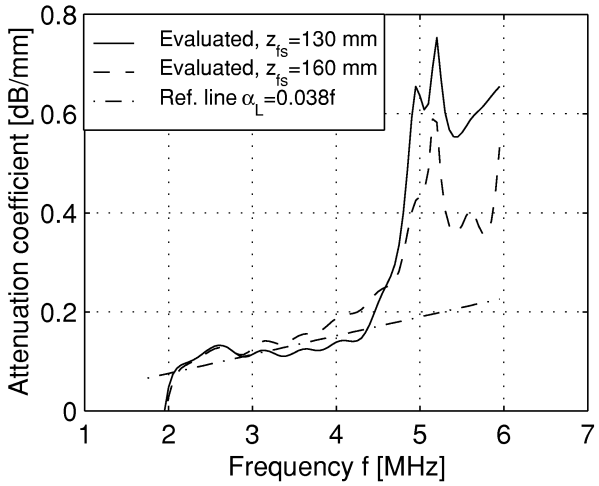

Fig. 3.8. The evaluated attenuations of the copper plate for z_{fs} =131 mm (solid) and 161 mm (dash), together with the reference line $\alpha_L = 0.038f$ (dotted), where α_L is in dB/mm and f is in MHz.

3.3 Evaluation of ultrasonic grain noise in polycrystalline metals

3.3.1 Evaluation using the independent scattering model

The independent scattering model (ISM) is used to estimate the grain noise. The theory and the experimental method have been presented in detail in our last report [1].

Using the same procedure as in [1], two copper specimens, T19A and T19B, were inspected. The specifications of the specimens are given in Table 3.1. The transducer use was PANAMETRICS V307, 25-mm diameter, 191.1-mm focal length (measured), and 5.35-MHz central frequency (measured). The sound velocities of water and the copper specimens measured were 1490 m/s, and

4770 m/s, respectively, which were a little different from those presented in [1]. The water paths for measuring the attenuation coefficients in specimens, T19A and T19B, were set 97 and 108 mm, respectively, and the water paths for measuring the grain noise in T19A and T19B both were set 97 mm.

Table 3.1 Specifications, experimental setup, and measured attenuation coefficients and figure of merit (FOM) for Specimens T19A and T19B.

Specimen	Condition	Length (mm)	Width (mm)	Thickness (mm)	Scanning position	Attenuation (dB/mm)	FOM (1/mm)
T19A	Extruded	80.0	65.0	54.9	67x52	$0.1174^{+0.0265}_{-0.0062}$	0.134
T19B	Extruded	94.0	66.4	52.3	80x52	$0.1181^{+0.0279}_{-0.0116}$	0.140

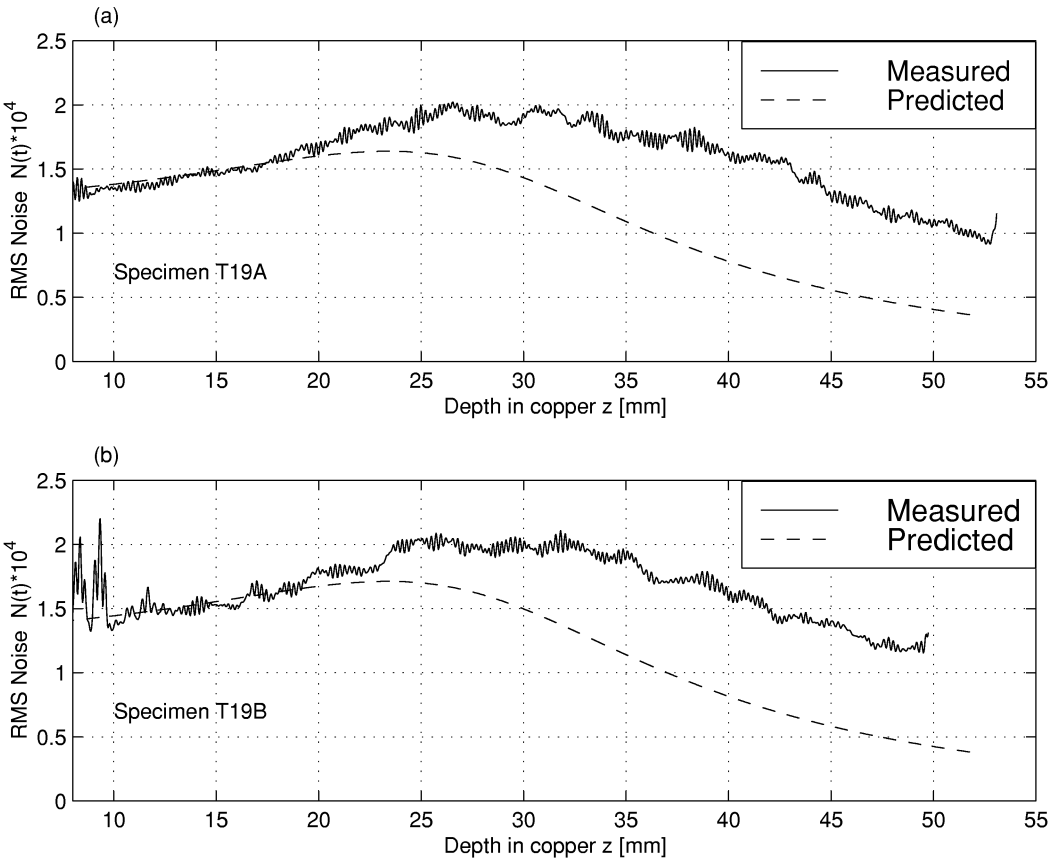

Fig. 3.9. Measured (solid) and predicted (dash) RMS grain noise, $N(t)$, in copper specimens (a) T19A, and (b) T19B.

The attenuation coefficients of the two specimens were measured using the spectral shift method (see Table 3.1), and they are quite close. The root-mean-square values of grain noise were measured and

predicted with the ISM (see Fig. 3.9). From Fig. 3.9, a broad maximum of the RMS noise can be seen in each case due to focusing of the ultrasonic beam within the copper specimen. The calculated figure-of-merits for the two specimens are given in Table 3.1. It is interesting to compare the present results with those reported in [1]. The attenuation coefficients of T19A and T19B both are smaller, and their RMS noise curves show the maximums. Whereas the RMS noise curves of the three specimens (Specimens #1, #2 and #4) in [1] did not show the maximums because of the larger attentions. The FOMs of T19A and T19B both are also quite close and smaller than those of Specimens #1, #2 and #4 in [1]. From the results in Table 3.1, we can deduce that the grain sizes in T19A and T19B are much smaller than those of Specimens #1, #2 and #4.

3.3.2 Evaluation using the K-distribution model

The theory of the K-distribution has been studied in detail in our previous report [1]. Here, we apply it to the estimation of grain noise in Specimens #4, #1, #2 and T19A (T19B is not considered here because it is close to T19A) that have grain sizes from large to small, respectively, and we also compare the estimated results from the K-distribution with those from the ISM. The measurements of the grain noise for Specimens #4, #1, and #2 that have been presented in our recent report [1] are re-used.

In order to make comparable the results estimated on the different specimens using the two methods, the regions of interest were chosen in such a way that the insonified volumes of the chosen regions should be as identical as possible. In the measurements made on Specimens #4, #1, and #2, the water path lengths used were all 130 mm. Thus, the focus position in each specimen was around 20 mm. For Specimen T19A, the water path length was set 97 mm so that the focus position was about 30 mm in T19A. The regions of interest chosen for Specimens #4, #1, and #2 were all from 8 to 34 mm in the specimens, and that for Specimen T19A was from 18 to 44 mm. Obviously, all the regions of interest cover the focal zones.

A K-parameter is the parameter related with the number density of scatterers, and can be calculated using the central moments of different orders [70]. Therefore, there can be more than one K-parameter available (e.g., α_1, α_4 and α_6 calculated from the 1st, 4th and 6th central moments) for use. It has been shown in [70] that the K-parameter calculated from the 1st order moment usually gives best results, and is denoted by α_1. Therefore, α_1 has been estimated for the four specimens using the above chosen regions of interest. The estimated α_1's are given in Table 3.2.

From the estimated α_1's, we can see that the smaller the grain size the larger the K-parameter. Physically, this means that the number of scatterers (grains) in an identical insonified volume is larger for the smaller scatterers (grains). This preliminary result demonstrates the possibility of using the K-

parameter as an estimator for grain noise. However, using the K-distribution model for quantitative estimation, it needs doing more research on it.

Table 3.2 The estimated K-parameter for Specimens #4, #1, #2, and T19A.

Specimen	#4	#1	#2	T19A
K parameter (α_1)	2.03	2.72	3.95	16.83

3.4 Conclusions

To quantitatively estimate attenuation of a solid in the immersion case, a method for correcting the diffraction effect has been developed for the log-spectral difference method (LSDM). The correcting method has been established based on the extended angular spectrum approach that is used to calculate the echoes from the front and back surfaces of the immersed solid. In the case of a copper plate submerged in water and inspected by a linear array with a cylindrically curved surface, the correcting method has been theoretically tested for attenuation estimation. The results have shown that the estimated attenuation coefficient is in an excellent agreement with the exact one. The method has also applied to a real situation, in which the results have shown that the method yields reasonable evaluated attenuation values. This work has demonstrated that the method is possible to effectively correct diffraction effect so as to achieve quantitative estimation of attenuation.

For the estimation of grain noise, the ISM and the K-distribution method have been used. The results estimated using two methods have been compared. Unlike Specimens #4, #1 and #2, Specimen T19A has small attenuation, and its RMS noise from Specimen T19A has shown a maximum that arises from the focusing of ultrasound beam. Consequently, the FOM estimated using the ISM is small compared to those for Specimens #4, #1 and #2. This has yielded the same conclusion as drawn in [1] that the higher attenuation and the larger FOM correspond to the larger grains.

The results from the K-distribution method have demonstrated the possibility of using the K-parameter as a parameter related to the grain size and the number density of grains. However, the quantitative relation of the K-parameter with the grain properties has not been determined, and it needs more research.

3.5 References

[1] P. Wu, and T. Stepinski, *Inspection of Copper Canisters for Spent Nuclear Fuel by Means of Ultrasonic Array System - Modelling, Defect Detection and Grain Noise Estimation*, SKB Projektrapport, Augusti 1998.

[2] J. Krautkrämer and H. Krautkrämer, *Ultrasonic Testing of Materials*. 4th Edition, Springer-Verlag, Berlin, pp. 539-548, (1990).

[2'] C. Graciet, and B. Hosten, "Simultaneous measurement of speed, attenuation, thickness and density with reflected ultrasonic waves in plates," *Proc. IEEE 1994 Ultrason. Symp.* pp. 1219-1222, 1994.

[3] E.P. Papadakis, "Ultrasonic velocity and attenuation: measurement methods with scientific and industrial applications," in *Physical Acoustics*, ed. W.P. Mason, Academic Press, New York. **12**: 277-374 (1976).

[4] M.A. Breaseale, J.H. Cantrel, Jr., and J.S. Heyman, "Ultrasonic wave velocity and attenuation measurements," in *Methods of experimental physics: -- Ultrasonics*, ed. P.E. Edmonds, Academic Press, New York. **19**: 67-135 (1981).

[5] E.P. Papadakis, "The measurement of ultrasonic attenuation," in *Physical Acoustics*, ed. R.N. Thurston, and A.D. Pierce, Academic Press, San Diego. **19**: 107-155 (1990).

[6] R. Kuc, "Estimation of acoustic attenuation from reflected ultrasound signals: Comparison of spectral-shift and spectral-difference approaches," *IEEE Trans. Acoust. Speech, Signals Process.* **ASSP-32:** 1-6 (1984).

[6'] R. Kuc, "Bounds on estimating the acoustic attenuation of small tissue regions from reflected ultrasound," *Proc. IEEE.* **73:** 1159-1168 (1985).

[7] H.B. Huntington, A.G. Emslie, and V.W. Hughes, *J. Franklin Inst.* **245:** 1-6 (1945).

[8] E. Lommel, *Abhandl. d. Bayer. Akad. Wiss. Math. Naturwiss. Kl.* **15:** 233 (1886).

[9] O.A. Williams, "The piston source at high frequencies," *J. Acoust. Soc. Am.* **23:** 1-6 (1951).

[10] L.V. King, "On the acoustic radiation of the piezo electric oscillator etc.," *Can. J. Res.* **11:** 135-146 (1934).

[11] R. Bass, "Diffraction effects in the ultrasonic field of a piston source," *J. Acoust. Soc. Am.* **30:** 602-605 (1958).

[12] O.A. Williams, Jr., "Integrated signal on circular piston receiver centered in a piston beam, " *J. Acoust. Soc. Am.* **48:** 285-289 (1970).

[13] H. Seki, A. Granato, and R. Truell, "Diffraction effects in the ultrasonic field of a piston source and their importance in the accurate measurement of attenuation," *J. Acoust. Soc. Am.* **28:** 230-239 (1956).

[14] M.B. Gitis, and A.S. Khimunin, "Diffraction effects in ultrasonic measurements (review)," *Soviet Phys. – Acoust.* **14:** 413-431 (1969), translated from: Akusticheskii-Zhurnal. **14:** 489-513 (1968).

[14'] M.B. Gitis, and A.S. Khimunin, "Diffraction corrections for measurements of the absorption coefficient and velocity of sound " *Soviet Phys. – Acoust.* **14:** 305-310 (1969), translated from: Akusticheskii-Zhurnal. **14:** 363-370 (1968).

[15] A.S. Khimunin, "Numerical calculation of the diffraction corrections for the precise measurement of ultrasound absorption," *Acustica* **27:** 173-81 (1972).

[15'] A.S. Khimunin, "On the ultrasound diffraction losses for circular transducers of different radii," *Acustica* **54:** 13-22 (1983).

[16] G.C. Benson, and O. Kiyohara, "Tabulation of some integral functions describing diffraction effects in the ultrasonic field of a circular piston source," *J. Acoust. Soc. Am.* **55:** 184-185 (1974).

[17] A.L. Van-Buren, and P.H. Rogers, "Diffraction correction for a circular piston source," *Acustica* **31:** 45-47 (1974).

[18] P.H. Rogers, and A.L. Van-Buren, "An exact expression for the Lommel diffraction correction integral," *J. Acoust. Soc. Am.* **55:** 724-728 (1974).

[19] H. Apostolopulos, and H. Davies, "Absorption related diffraction corrections in the near field of an ideal piston radiator," *Acustica* **65:** 35-38 (1987).

[20] E.P. Papadakis, *J. Acoust. Soc. Am.* **31:** 150-152 (1959).

[21] E.P. Papadakis, "Rayleigh and stochastic scattering of ultrasonic waves in steel," *J. Appl. Phys.* **34:** 265-269 (1963).

[22] E.P. Papadakis, *J. Acoust. Soc. Am.* **35:** 490-494 (1963).

[23] E.P. Papadakis, "Diffraction of ultrsound radiating into an elastically anisotropic medium,"*J. Acoust. Soc. Am.* **36:** 414-422 (1964).

[24] E.P. Papadakis, "Ultrasonic diffraction loss and phase change in anisotropic materials,"*J. Acoust. Soc. Am.* **40:** 863-876 (1966).

[25] E.P. Papadakis, "Ultrasonic attenuation caused by scattering in polycrystalline media," in *Physical Acoustics*, ed. W.P. Mason, Academic Press, New York. **4** Part B: 269-328 (1968).

[26] E.P. Papadakis, "Ultrasonic diffraction loss and phase change for broad-band pulses," *J. Acoust. Soc. Am.* **52:** 847-849 (1972).

[27] E.P. Papadakis, "Ultrasonic diffraction from single apppertures with application to pulse measurements and crystal physics," in *Physical Acoustics*, ed. W.P. Mason, Academic Press, New York. **11**, 151-211 (1975).

[28] T.L. Rhyne, "Radiation coupling of a disk to a plane and back or a disk to disk: An exact solution," *J. Acoust. Soc. Am.* **61:** 318-324 (1977).

[29] A.S. Khimunin, "Ultrasonic propagation parameter measurements incorporating exact diffraction corrections," *Acustica* **39:** 87-95 (1978).

[30] R.C. Chivers, L. Bosselaar, and P.R. Filmore, "Effective area to be used in diffraction corrections," *J. Acoust. Soc. Am.* **68:** 80-84 (1980).

[31] L.W. Schmerr, Jr., and A. Sedov, "An elastodynamic model for compressional and shear wave transducers," *J. Acoust. Soc. Am.* **86:** 1988-1999 (1989).

[32] A. Sedov, and L.W. Schmerr, Jr., "Elastodynamic diffraction correction integrals," *J. Acoust. Soc. Am.* **86:** 2000-2005 (1989).

[33] X.M. Tang, M.N. Toksöz, and C.H. Cheng, "Elastic wave radiation and diffraction of a piston source," *J. Acoust. Soc. Am.* **87:** 1894-1902 (1990).

[34] R.B. Thompson, and T.A. Gray, "Analytic diffraction corrections to ultrasonic scattering measurements," in *Rev. of Progr in Quantitative Nondestructive Evaluation*. Plenum, New York, NY, USA. **2A:** 567-586 (1983).

[35] W.A. Simpson, Jr., and R.W. McClung, "Quantitative attenuation technique for materials characterization," *Materials Eval.* **49:** 1409-1413 (1991).

[36] R.B. Thompson, and T.A. Gray, "A model relating ultrasonic scattering measurements through liquid-solid interfaces to unbounded medium scattering amplitudes," *J Acoust. Soc. Am.,* **74:** 1279-1290 (1983)

[37] R.B. Thompson, and T.A. Gray, "Application of diffraction corrections to the absolute measurement of scattering amplitudes," in *Rev. of Progr in Quantitative Nondestructive Evaluation*. Plenum, New York, NY, USA. 3**A:** 373-383 (1984).

[38] D. Zhou, L. Peirlinckx, and L. Van Biesen, "Identification of parametric models for ultrasonic double transmission experiments on viscoelastic plates," *J Acoust. Soc. Am.* **99:** 1446-1458 (1996).

[39] L. Peirlinckx, P. Guillaume, R. Pintelon, and L. Van Biesen, "A global system identification approach for the accurate parametric modeling of ultrasonic reflection and transmission experiments," *IEEE Trans. Ultrason. Ferroelec. Freq. Contr.* **36:** 628-639 (1996).

[40] A. Penttinen, and M. Luukkala, "Diffraction losses associated with curved ultrasonic transducers," *J. Phys. D: Appl. Phys.* **10:** 665-669 (1977).

[41] M.G. Manley, N.N. Hsu, "Response of a focused transducer facing a rigid reflector," in *Rev. of Progr in Quantitative Nondestructive Evaluation*. Plenum Press, New York, NY, USA. 869-875 (1997)

[42] X. Chen, K.Q. Schwarz, and K.J. Parker, "Acoustic coupling from a focused transducer to a flat plate and back to the transducer," *J. Acoust. Soc. Am.* **95:** 3049-3054 (1994).

[43] M. O'Donnell, "Effects of diffraction on measurements of the frequency-dependent ultrasonic attenuation," *IEEE Trans. Biomed. Eng.* **BME-30:** 320-326 (1983).

[44] M.J.T.M. Cloostermans, and J.M. Thijssen, "A beam corrected estimation of the frequency-dependent attenuation of biological tissues from backscattered ultrasound," *Ultrason. Imag.* **5:** 136-147 (1983).

[45] M. Insana, J. Zagzebski, and E. Madsen, "Improvements in the spectral difference method for measuring ultrasonic attenuation," *Ultrason. Imag.* **5:** 331-345 (1983).

[46] J.F. Cardoso, and M. Fink, "Diffraction effects in pulse-echo attenuation measurement," in *Proc. IEEE 1984 Ultrason. Symp.* (IEEE cat no. 83 CH). 841-846 (1983).

[47] M. Fink and J.F. Cardoso, "Diffraction effects in pulse-echo measurement," *IEEE Trans. Sonics Ultrason.* **SU-31:** 313-329 (1984).

[48] R. Kuc, and D. Regula, "Diffraction effects in reflected ultrasound spectral estimates," *IEEE Trans. Biomed. Eng.* **BME-31:** 537-545 (1984).

[49] D.E. Robinson, L.S. Wilson, and T. Bianchi, "Beam pattern (diffraction) correction for ultrasonic attenuation," *Ultrason. Imag.* **6:** 293-303 (1984).

[50] F. Hottier, and J. Bernatets, "Estimation of ultrasonic attenuation in biological tissues," *Acta Electronica* **26:** 33-58 (1984).

[51] P. Laugier, G. Berger, M. Fink, and J. Perrin, "Diffraction correction for focused transducers in attenuation measurements *in vivo*," *Ultrason. Imag.* **9:** 248-259 (1987).

[52] J. Ophir, and D. Mehta, "Elimination of diffraction error in acoustic attenuation estimation via axial beam translation," *Ultrason. Imag.* **10:** 139-152 (1988).

[53] X.-L. Wang, and R. Feng, "Diffraction correction in backscattering measurement," Ultrasonics **27:** 239-244 (1989).

[54] I. Cespedes, and J. Ophir, "Diffraction correction methods for pulse-echo acoustic attenuation estimation (tissue characterisation)," *Ultrasound Med. Bio.* **16:** 707-717 (1990).

[55] J.F. Cardoso, M. Fink, "Echographic diffraction filters and the diffraction function for random media through an instantaneous time-frequency approach," *J. Acoust. Soc. Am.* **90:** 1074-1084 (1991).

[56] P. Jiang, R.E. Apfel, "Plane wave approximation in a pulse transmission system and its application to attenuation measurements (ultrasonics)," in *IEEE 1991 Ultrason. Symp. Proc.* (Cat. No.91CH3079-1). IEEE, New York, NY, USA. 671-674 (1991).

[57] I. Cespedes, J. Ophir, "Correction of diffraction errors in attenuation estimation with dynamic beam translation," *Ultrasound Med. Bio.* **18:** 213-218 (1992).

[58] W. Xu, and J.J. Kaufman, "Diffraction correction methods for insertion ultrasound attenuation estimation," *IEEE Trans. Biomed. Eng.* **40:** 563-570 (1993).

[59] J.J. Kaufman, W. Xu, A.E. Chiabrera, and R.S. Siffert, "Diffraction effects in insertion mode estimation of ultrasonic group velocity," *IEEE Trans. Ultrason. Ferroelec. Freq. Contr.* **42:** 232-242 (1995).

[60] B. Zeqiri, "Validation of a diffraction correction model for through-transmission substitution measurements of ultrasonic absorption and phase velocity," *J. Acoust. Soc. Am.* **99:** 996-1001 (1996).

[61] X. Chen, D. Philips, K.Q. Schwarz, J.G: Mottley, and K.J. Parker, "The measurement of backscatter coefficient from a broadband pulse-echo system: a new formulation," *IEEE Trans. Ultrason. Ferroelec. Freq. Contr.* **44:** 515-525 (1997).

[62] E.P. Papadakis, "The measurement of ultrasonic velocity," in *Physical Acoustics*, ed. R.N. Thurston, and A.D. Pierce, Academic Press, San Diego. **19**: 81-106 (1990).

[63] A.S. Khimunin, " Numerical calculation of the diffraction corrections for the precise measurement of ultrasound phase velocity," *Acustica* **32:** 192-200 (1975).

[64] A.S. Khimunin, and E.A. Lvova, "On diffraction corrections in ultrasound velocity measurements using the direct pulse method," *Acoustics Letters* **6:** 106-109 (1983).

[65] P.B. Nagy, "Diffraction correction for radiation force measurement on an ideal plane reflector," *Acustica* **61:**125-129 (1986).

[66] P.B. Nagy, "Diffraction correction for a radiation force measurement on an infinite plane target *J. Acoust. Soc. Am.* **79:** 1794-1797 (1986).

[67] A.S. Khimunin, and E.A. Lvova, "On the diffraction effects in an ultrasonic interferometer," *Acustica* **53:** 107-122 (1983).

[68] A.S. Khimunin, "Numerical modeling of the diffraction problem for an ultrasonic interferometer," *Soviet Phys. - Acoust.* **29:** 65-67 (1983).

[69] K.B. Ocheltree and L.A. Frizzell, "Sound field calculation for rectangular sources," *IEEE Trans. Ultrason. Ferroelec. Freq. Contr.* **36:** 242-248 (1989).

[70] T. Stepinski, and P. Wu, *Ultrasonic Inspection of Nuclear Copper Canisters*, SKB Projektrapport 97-08, August 1997.

[71] P. Wu, and T. Stepinski, "Elastic fields in immersed isotropic solids from phased array: the time harmonic case," *Res. Nondestr. Evla.* **10**: 185-204, (1998).

[72] L.E. Kinsler, A.R. Frey, A.B. Coppens, and J.V. Sanders, *Fundamentals of Acoustics*. Wiley, New York, Chap. 7, (1982).

[73] P. Wu, and T. Stepinski, "Extension of the angular spectrum approach to curved radiators," *J. Acoust. Soc. Am.* **105**: 2618-2627, (1999).

[74] P. Wu, and T. Stepinski, " Spatial impulse response method for predicting pulse-echo fields from a linear array with cylindrically concave surface," *IEEE Ultrason. Ferroelec. Freq. Contr.* **46:** 1283-1297, (1999).

[75] T. Stepinski, and P. Wu, *Ultrasonic Inspection of Nuclear Copper Canisters*, SKB Projektrapport 97-01, December 1996.

[76] L.M. Brekhovskikh, *Waves in Layered Media*. 2nd Edition, Academic, New York, Chap. I, (1980).

[77] B. Zeqiri, "Erroes in attenuation measurements due to nonlinear propagation effects," *J. Acoust. Soc. Am.* **91**: 2585-2593, (1992).

[78] J. Wu, "Effects of nonlinear interaction on meamsurements of frequency-dependent attenuation coefficients," *J. Acoust. Soc. Am.* **99**: 3380-3384, (1996).

ISSN 1404-0344
CM Gruppen AB, Bromma, 1999